

Electronic Supplementary Information

Structural and Dimensional Control of Porphyrin Capsules Using Group 15 Tris(3- pyridyl) Linkers

Álvaro García-Romero,^a Daniel Miguel,^a Dominic S. Wright,^b Celedonio M. Álvarez,^a and Raúl García-Rodríguez*^a

^a GIR MIOMeT-IU, Cinquima, Química Inorgánica, Facultad de Ciencias, Universidad de Valladolid, Campus Miguel Delibes, 47011, Valladolid, Spain. E-mail: raul.garcia.rodriguez@uva.es

^b Dominic S. Wright – Department of Chemistry, University of Cambridge, Cambridge CB2 1EW, U.K.

Contents

Experimental details	5
NMR studies and spectra	9
Figure S1. Compound 1 ·Zn, $\{[(\text{Sb}(\text{3-py})_3)]_2 \cdot (\text{ZnTPP})_3\}$	9
Figure S2. ^1H NMR spectrum of 1 ·Zn.....	9
Figure S3. $^{13}\text{C}\{^1\text{H}\}$ NMR spectrum of 1 ·Zn.	10
Figure S4. Selected region of the ^1H – ^1H NOESY spectrum of 1 ·Zn.	10
Figure S5. Compound 2 ·Zn, $\{[(\text{Bi}(\text{3-py})_3)]_2 \cdot (\text{ZnTPP})_3\}$	11
Figure S6. ^1H NMR spectrum of 2 ·Zn.....	11
Figure S7. $^{13}\text{C}\{^1\text{H}\}$ NMR spectrum of 2 ·Zn.	12
Figure S8. Selected region of the ^1H – ^1H NOESY spectrum of 2 ·Zn.....	12
Figure S9. ^1H NMR spectra of a sample of (a) 1 ·Zn and (b) 2 ·Zn in CDCl_3 at 298, 273, 233 and 213 K.....	13
Figure S10. Compound P ·Mg, $\{[(\text{P}(\text{3-py})_3)]_2 \cdot (\text{MgTPP})_3\}_n$	14
Figure S11. ^1H NMR spectrum of P ·Mg.	14
Figure S12. $^{13}\text{C}\{^1\text{H}\}$ NMR spectrum of P ·Mg.....	15
Figure S13. $^{31}\text{P}\{^1\text{H}\}$ NMR spectrum of P ·Mg.	15
Figure S14. Selected region of the ^1H – ^1H ROESY spectrum of P ·Mg	16
Figure S15. Compound 1 ·Mg, $\{[(\text{Sb}(\text{3-py})_3)]_2 \cdot (\text{MgTPP})_3\}_n$	16
Figure S16. ^1H NMR spectrum of 1 ·Mg.....	17
Figure S17. $^{13}\text{C}\{^1\text{H}\}$ NMR spectrum of 1 ·Mg.	17
Figure S18. Selected region of the ^1H – ^1H NOESY spectrum of 1 ·Mg.	18
Figure S19. Compound 2 ·Mg, $\{[(\text{Bi}(\text{3-py})_3)]_2 \cdot (\text{MgTPP})_3\}_n$	18
Figure S20. ^1H NMR spectrum of 2 ·Mg.	19
Figure S21. $^{13}\text{C}\{^1\text{H}\}$ NMR spectrum of 2 ·Mg.	19
Figure S22. Selected region of the ^1H – ^1H NOESY spectrum of 2 ·Mg.	20
Figure S23. Compound 3	20
Figure S24. ^1H NMR spectrum of 3	21
Figure S25. $^{13}\text{C}\{^1\text{H}\}$ NMR spectrum of 3	21
Figure S26. Selected region of the ^1H – ^{13}C HMBC spectrum of 3	22
Figure S27. Compound 3 ·py.....	22
Figure S28. ^1H NMR spectrum of 3 ·py.....	23
Figure S29. Compound 4	23
Figure S30. ^1H NMR spectrum of 4	24
Figure S31. $^{13}\text{C}\{^1\text{H}\}$ NMR spectrum of 4	24
Figure S32. Selected region of the ^1H – ^{13}C HMBC spectrum of 4	25
Figure S33. Compound 3 ·Zn, $\{[\text{Cl}_2\text{Sb}(\text{3-py})_3] \cdot (\text{ZnTPP})_3\}$	26
Figure S34. ^1H NMR spectrum of 3 ·Zn.	26
Figure S35. $^{13}\text{C}\{^1\text{H}\}$ NMR spectrum of 3 ·Zn.....	27
Figure S36. Selected region of the ^1H – ^1H NOESY spectrum of 3 ·Zn	27
Figure S37. Compound 3 ·Mg, $\{[(\text{Cl}_2\text{Sb}(\text{3-py})_3)] \cdot (\text{MgTPP})_3\}_n$	28
Figure S38. ^1H NMR spectrum of 3 ·Mg.	28
Figure S39. $^{13}\text{C}\{^1\text{H}\}$ NMR spectrum of 3 ·Mg.	29
DOSY experiments	30
Figure S40. ^1H DOSY NMR spectra of (a) 1 ·Zn and (b) 2 ·Zn at 298 K in CDCl_3	30
Figure S41. ^1H DOSY NMR spectrum of P ·Mg.....	31

Table S1. D-MW analysis using the ^1H DOSY NMR of $\text{P}\cdot\text{Mg}$	31
Figure S42. $ECC_{DSE}^{CDCl_3}$ was used to determine the MW_{det} of $\text{P}\cdot\text{Mg}$	32
Figure S43. ^1H DOSY NMR spectrum of $\mathbf{1}\cdot\text{Mg}$	32
Table S2. D-MW analysis using the ^1H DOSY NMR of $\mathbf{1}\cdot\text{Mg}$	32
Figure S44. $ECC_{DSE}^{CDCl_3}$ was used to determine the MW_{det} of $\mathbf{1}\cdot\text{Mg}$	33
Figure S45. ^1H DOSY NMR spectrum of $\mathbf{2}\cdot\text{Mg}$	34
Table S3. D-MW analysis using the ^1H DOSY NMR of $\mathbf{2}\cdot\text{Mg}$	34
Figure S46. $ECC_{DSE}^{CDCl_3}$ was used to determine the MW_{det} of $\mathbf{2}\cdot\text{Mg}$	35
Binding data analysis.....	36
Figure S47. Stacked ^1H -NMR spectra of the titration of ligand $\mathbf{1}$	37
Figure S48. Chemical shifts of the $\text{Sb}(\text{3-py})_3$ signals against $[\text{G}]/[\text{H}]$	37
Figure S49. Stacked ^1H -NMR spectra of the titration of ligand $\mathbf{2}$	38
Figure S50. Chemical shifts of the $\text{Bi}(\text{3-py})_3$ signals against $[\text{G}]/[\text{H}]$	38
High resolution mass data.....	39
Figure S51. HR-MS (ESI-TOF) of $\mathbf{1}\cdot\text{Zn}$	39
Figure S52. HR-MS (ESI-TOF) of $\mathbf{2}\cdot\text{Zn}$	39
Figure S53. HR-MS (ESI-TOF) of $\{[\text{P}(\text{3-py})_3]\cdot(\text{MgTPP})_3\}$	40
Figure S54. HR-MS (ESI-TOF) of $\{[\text{Sb}(\text{3-py})_3]\cdot(\text{MgTPP})_3\}$	40
Figure S55. HR-MS (ESI-TOF) of $\{[\text{Bi}(\text{3-py})_3]\cdot(\text{MgTPP})_3\}$	41
Figure S56. HR-MS (MALDI-TOF) of $\mathbf{3}$	41
Figure S57. HR-MS (ESI-TOF) of $\mathbf{4}$	42
X-ray crystallographic studies.....	43
Figure S58. Solid-state structures of closed-capsule conformers of $\mathbf{2}\cdot\text{Zn}$	46
Figure S59. X-ray structure of the 2D polymeric structure of $\text{P}\cdot\text{Mg}$	46
Figure S60. X-ray structure of the 2D polymeric structure of $\text{P}\cdot\text{Mg}$	47
Figure S61. X-ray structure of the 2D polymeric structure of $\mathbf{1}\cdot\text{Mg}$	47
Figure S62. X-ray structure of the 2D polymeric structure of $\mathbf{1}\cdot\text{Mg}$	48
Figure S63. X-ray structure of the 2D polymeric structure of $\mathbf{2}\cdot\text{Mg}$	48
Figure S64. X-ray structure of the 2D polymeric structure of $\mathbf{2}\cdot\text{Mg}$	49
Figure S65. Correlation between the covalent radii of the bridgehead atom and the effective size of the capsule.....	49
Figure S66. Molecular structure of $\text{Cl}_2\text{Sb}^\vee(\text{3N-py})_3\cdot\text{Py}$ ($\mathbf{3}\cdot\text{py}$).....	50
Figure S67. Molecular structure of the monomeric unit of $\text{Cl}_2\text{Bi}(\text{3N-py})_3$ ($\mathbf{4}$).....	50
Table S4. Crystallographic data.....	51
Table S5. Selected bond length and angles.....	55
Figure S68. Trends in the X-ray structures of the capsules.....	56
Figure S69. Linear correl of the bridgehead atom and the $\text{C}_6\text{--C}_6$ distances.....	56
Figure S70. Linear correlation between the covalent radii of the bridgehead atom and the volume of the capsule.....	57
Figure S71. Comparison of predicted and the experimental XRPD patterns.....	58
Figure S72. Comparison of predicted and the experimental XRPD patterns.....	59
Figure S73. Comparison of predicted and the experimental XRPD patterns.....	59
TGA and TGA-MS studies.....	60
Figure S74. TGA thermograms of $\text{P}\cdot\text{Mg}$, $\mathbf{1}\cdot\text{Mg}$ and $\mathbf{2}\cdot\text{Mg}$	61
Figure S75. TGA thermogram of $\text{P}\cdot\text{Mg}$	61

Figure S76. TGA thermogram of 1 ·Mg.....	61
Figure S77. TGA thermogram of 2 ·Mg.....	62
Figure S78. TGA-MS analysis of 2 ·Mg.....	62
N₂ and CO₂ Sorption experiments.....	63
Table S6. Porosity parameters from N ₂	63
Table S7. Porosity parameters from CO ₂	63
Figure S79. N ₂ adsorption-desorption isotherms for P ·Mg.....	63
Figure S80. N ₂ adsorption-desorption isotherms for 2 ·Mg.....	64
Figure S81. CO ₂ adsorption isotherm for P ·Mg.....	64
Figure S82. CO ₂ adsorption isotherm for 2 ·Mg.....	65
Computational details.....	66
Figure S83. Comparison of the X-ray and the DFT-calculated structure of P ·Zn.....	66
Figure S84. Comparison of the X-ray and the DFT-calculated of 1 ·Zn.....	67
Figure S85. Comparison of the X-ray and the DFT-calculated of 2 ·Zn.....	67
Preliminary catalytic studies.....	80
Scheme S1. Bi-catalyzed cleavage of 1,2 diols (R = Me or Ph).....	80
Figure S86. Kinetic experiment of Sb-catalyzed oxidation of α-hydroxyketones.....	81
Table S8. Sb-catalyzed oxidation of α-hydroxyketones.....	82
References.....	83

Experimental details

General Methods

All syntheses were carried out on a vacuum line under a N₂ atmosphere. Products were isolated and handled under a N₂ atmosphere. 3-Bromopyridine, NMR solvents, and reaction solvents were stored over molecular sieves and degassed using three freeze–pump–thaw cycles under N₂ prior to use. Compounds P(3-py)₃, Sb(3-py)₃ (**1**) and Bi(3-py)₃ (**2**) were synthesized as described previously.^[1,2]

NMR spectra were recorded using 500 MHz Agilent DD2 instruments equipped with a cold probe and a 400 MHz Agilent instrument equipped with a ONEPROBE in the Laboratory of Instrumental Techniques (LTI) Research Facilities, University of Valladolid. Chemical shifts (δ) are reported in parts per million (ppm). ¹H and ¹³C NMR spectra are referenced to TMS. ³¹P NMR is referenced to H₃PO₄. ¹H spectra were acquired on a 500 MHz Agilent spectrometer using the 2D DOSY gradient compensated stimulated echo with convection compensation (DgcsteSL-cc) pulse sequence. Sixteen gradient levels ranging from 7 to 53 G/cm (12% to 88% of the maximum gradient strength) were used. The diffusion delay (Δ) was 50 ms and the diffusion gradient length (δ) was 1.7 ms. For each DOSY NMR experiment, a series of 16 spectra was collected. Spectra were recorded in CDCl₃, and the temperature was set to and controlled at 298 K. Coupling constants (*J*) are reported in Hz. Standard abbreviations are used to indicate multiplicity: s = singlet, d = doublet, t = triplet, and m = multiplet. ¹H and ¹³C peak assignments were performed with the help of additional 2D NMR experiments (¹H–¹³C HSQC, ¹H–¹³C HMBC, ¹H–¹H NOESY, ¹H–¹H ROESY, and ¹H–¹H COSY). High-resolution mass spectra were recorded at the mass spectrometry service of the Laboratory of Instrumental Techniques (LTI) of the University of Valladolid. An Agilent TOF-LC/MS 6210 spectrometer (ESI-TOF, positive ion mode), a UPLC-MS system (UPLC: Waters ACQUITY H-class UPLC; MS: Bruker Maxis Impact) with electrospray ionization (ESI positive ion mode), a MALDI-TOF system (MALDI-TOF) and a Bruker autoflex speed (N₂ laser: 337 nm, pulse energy: 100 μ J, 1 ns; acceleration voltage: 19 kV, reflector positive mode) were used. *Trans*-2-[3-(4-*tert*-butylphenyl)-2-methyl-2-propenylidene]malonitrile (DCTB) was used as the matrix. Elemental analysis was obtained using a Thermo Scientific FLASH 2000 Elemental Analyzer at the Parque Científico Tecnológico (PTC) facilities of the University of Burgos.

Diffraction data were collected using an Oxford Diffraction Supernova diffractometer equipped with an Atlas CCD area detector and a four-circle kappa goniometer. For the data collection, a Mo micro-focused source with multilayer optics was used. When necessary, crystals were mounted directly from solution using perfluorohydrocarbon oil to prevent atmospheric oxidation, hydrolysis, and solvent loss. Data integration, scaling, and empirical absorption correction were performed using the CrysAlisPro software package.^[3] The structure was solved by direct methods and refined by full-matrix-least-squares against F² with SHELX^[4] in OLEX2.^[5] Non-hydrogen atoms were refined anisotropically, and hydrogen atoms were placed at idealized positions and refined using the riding model. Graphics were made with OLEX2^[5] and MERCURY.^[6] For measurement of the solvent-accessible voids in the Mg structures (**P**·Mg, **1**·Mg, **2**·Mg), first, the solvent molecules were removed from the X-ray structures. Once the solvent was removed, the solvent-accessible volume was calculated using the “Calculate Solvent Accessible Voids” tool in Olex2 with a probe radius of 1.2 Å and a grid spacing of 0.1 Å.^[5]

Synthetic procedures

Synthesis of 1·Zn: A Schlenk tube was charged with **1** (10.5 mg, 0.029 mmol) and ZnTPP (60 mg, 0.088 mmol), and 2 ml of CHCl₃ was then added. The resulting dark-purple solution was stirred for 1 hour at r.t. The solution was filtered with a syringe filter into a narrow Schlenk flask under a N₂ atmosphere, and slow diffusion of hexane (20 ml) at r.t. yielded **1**·Zn as purple blocks suitable for X-ray crystallography that were dried under vacuum. Yield (calculated as [Sb(3-py)₃·(ZnTPP)₃]·CHCl₃, based on elemental analysis that indicates solvent loss from the crystal): 45.2 mg (0.018 mmol, 62.1%). ¹H NMR (298 K, CDCl₃, 500 MHz): δ = 8.73 (s, 24H, H₁₃), 7.98 (d, J = 7.6 Hz, 24H, H₉ Ph), 7.69 (t, J = 7.6 Hz, 12H, H₇ Ph), 7.56 (t, J = 7.6 Hz, 24H, H₈ Ph), 5.73 (br, 3H, H₄ py), 5.16 (br, 3H, H₅ py), 4.37 (br, 3H, H₆ py), 3.80 (br, 3H, H₂ py). ¹³C{¹H} NMR (298 K, CDCl₃, 100.6 MHz): δ = 150.76 (C₂ py), 150.07 (C₁₂), 145.92 (C₆ py), 143.17 (C₁₀ py), 141.79 (C₄ py), 134.57 (C₉ Ph), 131.80 (C₁₃), 129.55 (C₃), 127.41 (C₇ Ph), 126.44 (C₈ Ph), 123.95 (C₅ py), 120.79 (C₁₁). Elemental analysis (%) calcd for **1**·Zn·CHCl₃ (C₁₄₈H₉₇Cl₃N₁₅SbZn₃): C 70.8, H 3.9, N 8.4. Found: C 70.7, H 3.9, N 8.4. HR-MS [ESI, positive ion mode ESI-TOF]: m/z for C₁₄₇H₉₇SbZn₃N₁₅ [**1**·Zn+H]⁺ calcd: 2390.4957. Found: 2390.4940 (-0.7 ppm error).

Synthesis of 2·Zn: A Schlenk tube was charged with **2** (13.07 mg, 0.029 mmol) and ZnTPP (60 mg, 0.088 mmol), and 2 ml of CHCl₃ was then added. The resulting dark-purple solution was stirred for 1 hour at r.t. The solution was filtered with a syringe filter into a narrow Schlenk flask under a N₂ atmosphere, and slow diffusion of hexane (20 ml) at r.t. yielded **2**·Zn as purple blocks suitable for X-ray crystallography that were dried under vacuum. Yield (calculated as [Bi(3-py)₃·(ZnTPP)₃]·CHCl₃ based on elemental analysis that indicates solvent loss from the crystal): 43.6 mg (0.017 mmol, 57.9%). ¹H NMR (298 K, CDCl₃, 500 MHz): δ = 8.71 (s, 24H, H₁₃), 7.94 (d, J = 7.7 Hz, 24H, H₉ Ph), 7.68 (t, J = 7.7 Hz, 12H, H₇ Ph), 7.53 (t, J = 7.7 Hz, 24H, H₈ Ph), 5.61 (br, 3H, H₅ py), 5.23 (br, 3H, H₄ py), 3.94 (br, 3H, H₆ py), 3.42 (br, 3H, H₂ py). ¹³C{¹H} NMR (298 K, CDCl₃, 100.6 MHz): δ = 150.91 (C₂ py), 150.03 (C₁₂), 145.74 (C₃ py), 144.67 (C₆ py), 143.51 (C₄ py), 143.18 (C₁₀ py), 134.55 (C₉ Ph), 131.75 (C₁₃), 127.37 (C₇ Ph), 126.39 (C₈ Ph), 125.76 (C₅ py), 120.72 (C₁₁). Elemental analysis (%) calcd for **2**·Zn·CHCl₃ (C₁₄₈H₉₇Cl₃N₁₅BiZn₃): C 68.5, H 3.8, N 8.1. Found: C 68.7, H 3.9, N 8.2. HR-MS [ESI, positive ion mode ESI-TOF]: m/z for C₁₄₇H₉₇BiN₁₅Zn₃ [**2**·Zn+H]⁺ calcd: 2478.5719. Found: 2478.5664 (-2.2 ppm error).

Synthesis of 1·Mg: A Schlenk tube was charged with **1** (14.5 mg, 0.040 mmol) and MgTPP (39 mg, 0.061 mmol), and 2 ml of CHCl₃ was then added. The resulting dark-purple solution was stirred for 1 hour at r.t. The solution was filtered with a syringe filter into a narrow Schlenk flask under a N₂ atmosphere, and slow diffusion of hexane (20 ml) at r.t. yielded **1**·Mg as purple blocks suitable for X-ray crystallography that were dried under vacuum. Yield (calculated as {[Sb(3-py)₃]₂·(MgTPP)₃·0.5CHCl₃]_n based on elemental analysis that indicates solvent loss from the crystal): 30.3 mg (0.011 mmol, 56.5%). ¹H NMR (298 K, CDCl₃, 500 MHz): δ = 8.73 (s, 24H, H₁₃), 8.01 (d, J = 7.7 Hz, 24H, H₉ Ph), 7.69 (t, J = 7.7 Hz, 12H, H₇ Ph), 7.59 (t, J = 7.6 Hz, 24H, H₈ Ph), 6.33 (t, br, 6H, H₅ py), 6.20 (br, 6H, H₄ py), 5.99 (br, 6H, H₆ py), 5.59 (br, 6H, H₂ py). ¹³C{¹H} NMR (298 K, CDCl₃, 100.6 MHz): δ = 152.81 (C₂ py), 149.97 (C₁₂), 147.80 (C₆ py), 143.69 (C₁₀ py), 142.63 (C₄ py), 134.75 (C₉ Ph), 131.92 (C₁₃), 130.52 (C₃), 127.21 (C₇ Ph), 126.33 (C₈ Ph), 124.33 (C₅ py), 121.68 (C₁₁). Elemental analysis (%) calcd for **1**·Mg·0.5CHCl₃ (C_{162.5}H_{108.5}Cl_{1.5}N₁₈Sb₂Mg₃): C 72.7, H 4.1, N 9.4. Found: C 72.6, H 4.4, N 8.7. HR-MS

[ESI, positive ion mode ESI-TOF]: m/z for $C_{147}H_{97}Mg_3N_{15}Sb \{[Sb(3-py)_3] \cdot (MgTPP)_3 + H\}^+$ calcd: 2267.6680. Found: 2267.6702 (1.0 ppm error).

Synthesis of 2·Mg: A Schlenk tube was charged with **2** (18.0 mg, 0.040 mmol) and MgTPP (39 mg, 0.061 mmol), and 2 ml of $CHCl_3$ was then added. The resulting dark-purple solution was stirred for 1 hour at r.t. The solution was filtered with a syringe filter into a narrow Schlenk flask under a N_2 atmosphere, and slow diffusion of hexane (20 ml) at r.t. yielded **2·Mg** as purple blocks suitable for X-ray crystallography that were dried under vacuum. Yield (calculated as $\{[Bi(3-py)_3]_2 \cdot (MgTPP)_3 \cdot 0.5CHCl_3\}_n$ based on elemental analysis that indicates solvent loss from the crystal): 41.4 mg (0.014 mmol, 72.4%). 1H NMR (298 K, $CDCl_3$, 500 MHz): δ = 8.71 (s, 24H, H_{13}), 7.98 (d, J = 7.7 Hz, 24H, H_9 Ph), 7.69 (t, J = 7.7 Hz, 12H, H_7 Ph), 7.56 (t, J = 7.7 Hz, 24H, H_8 Ph), 6.32 (br, 6H, H_4 py), 6.25 (br, 6H, H_5 py), 5.67 and 5.35 (br, 3H/3H, $H_{2,6}$ py). $^{13}C\{^1H\}$ NMR (298 K, $CDCl_3$, 100.6 MHz): δ = 153.42 (C_2 py), 149.97 (C_{13}), 146.72 (C_6 py), 146.59 (C_3 py), 144.18 (C_4 py), 143.68 (C_{10} Ph), 134.76 (C_9 Ph), 131.90 (C_{13}), 127.21 (C_7 Ph), 126.32 (C_8 Ph), 126.05 (C_5 py), 121.67 (C_{11}). Elemental analysis (%) calcd for **2·Mg·0.5CHCl₃** ($C_{162.5}H_{108.5}Cl_{1.5}N_{18}Bi_2Mg_3$): C 68.3, H 3.8, N 8.8. Found: C 68.2, H 4.1, N 8.2. HR-MS [ESI, positive ion mode ESI-TOF]: m/z for $C_{147}H_{97}BiMg_3N_{15} \{[Bi(3-py)_3] \cdot (MgTPP)_3 + H\}^+$ calcd: 2354.7442. Found: 2354.7420 (-0.9 ppm error).

Synthesis of P·Mg: A Schlenk tube was charged with $P(3-py)_3$ (10.80 mg, 0.040 mmol) and MgTPP (39 mg, 0.061 mmol), and 2 ml of $CHCl_3$ was then added. The resulting dark-purple solution was stirred for 1 hour at r.t. The solution was filtered with a syringe filter into a narrow Schlenk flask under a N_2 atmosphere, and slow diffusion of hexane (20 ml) at r.t. yielded **P·Mg** as purple blocks suitable for X-ray crystallography that were dried under vacuum. Yield: 28.3 mg (0.011 mmol, 57.9%). 1H NMR (298 K, $CDCl_3$, 500 MHz): δ = 8.69 (s, 24H, H_{13}), 7.92 (d, J = 7.7 Hz, 24H, H_9 Ph), 7.68 (t, J = 7.7 Hz, 12H, H_7 Ph), 7.52 (t, J = 7.7 Hz, 24H, H_8 Ph), 6.19 (br, 6H, H_5 py), 5.71 (br, 6H, H_4 py), 5.59 and 5.02 (br, 3H/3H, $H_{2,6}$ py). $^{13}C\{^1H\}$ NMR (298 K, $CDCl_3$, 100.6 MHz): δ = 150.68 (d, J_{CP} = 28.5 Hz, C_2 py), 149.88 (C_{12}), 147.47 (C_6 py), 143.57 (C_{10} Ph), 139.73 (d, J_{CP} = 13.4 Hz, C_4 py), 134.68 (C_9 Ph), 131.91 (C_{13}), 129.33 (d, J_{CP} = 15.4 Hz, C_3 py), 127.23 (C_7 Ph), 126.30 (C_8 Ph), 123.35 (d, J_{CP} = 3.5 Hz, C_5 py), 121.67 (C_{11}). $^{31}P\{^1H\}$ NMR (298 K, $CDCl_3$, 202.5 MHz): δ = -24.79. Elemental analysis (%) calcd for **P·Mg** ($C_{162}H_{108}N_{18}P_2Mg_3$): C 80.0, H 10.3, N 4.5. Found: C 79.2, H 10.1, N 4.6. HR-MS [ESI, positive ion mode ESI-TOF]: m/z for $C_{147}H_{97}PMg_3N_{15} \{[P(3-py)_3] \cdot (MgTPP)_3 + H\}^+$ calcd: 2176.7376. Found: 2176.7423 (2.2 ppm error).

Synthesis of 3: **1** (100 mg, 0.28 mmol) was dissolved in dry DCM (3 ml). To this was added dropwise SO_2Cl_2 (0.28 ml, 0.28 mmol, 1.0 M in DCM) over 5 min at room temperature. The resulting suspension was stirred for 1 h at room temperature, and all volatiles were removed under vacuum. DCM (20 ml) was added to the precipitate, and the resulting suspension was filtered with a syringe filter to yield a colourless solution that was concentrated under vacuum, and slow diffusion of *n*-hexane (20 mL) at -24 °C yielded **3** as a white powder. Yield: 51 mg (0.12 mmol, 42.6%). 1H NMR (298 K, $MeCN-d_3$, 500 MHz): δ = 9.15 (s, 3H, H_2 py), 8.69 (d, J = 5.0 Hz, 3H, H_6 py), 8.56 (d, J = 8.2 Hz, 3H, H_4 py), 7.58 (dd, J = 5.0/8.2 Hz, 3H, H_5 py). $^{13}C\{^1H\}$ NMR (298 K, $MeCN-d_3$, 100.6 MHz): δ = 152.59 (C_2 py), 150.81 (C_6 py), 143.88 (C_4 py), 144.70 (C_3 py), 125.94 (C_5 py). Elemental analysis (%) calcd for **3** ($C_{15}H_{12}N_3SbCl_2$): C 42.2, H 2.8, N 9.8. Found: C 42.5, H 2.9, N 9.6. HR-MS [MALDI, positive ion mode MALDI-TOF]: m/z for $C_{15}H_{13}N_3SbCl_2 [3+H]^+$ calc: 427.9508. Found: 427.9509 (0.2 ppm error).

Synthesis of 3-py: 3 (50 mg, 0.12 mmol) was dissolved in pyridine (2 ml), and slow diffusion of *n*-hexane (6 ml) at room temperature yielded $\text{Cl}_2\text{Sb}(3\text{-py})_3\cdot\text{Py}$ as white crystals suitable for X-ray crystallography. Yield (calculated as $\text{Cl}_2\text{Sb}(3\text{-py})_3\cdot\text{Py}$): 14 mg (0.027 mmol, 23%). ^1H NMR (298 K, MeCN-d_3 , 500 MHz): δ = 9.28 (s, 3H, H_2 py), 8.77 (d, J = 5.0 Hz, 3H, H_6 py), 8.60 (d, J = 4.4 Hz, 2H, H_8 py), 8.57 (d, J = 8.0 Hz, 3H, H_4 py), 7.84 (t, J = 7.7 Hz, 1H, py H_{10}), 7.60 (dd, J = 5.0/8.0 Hz, 3H, H_5 py), 7.42 (m, 2H, H_9).

Synthesis of 4: 2 (100 mg, 0.22 mmol) was dissolved in dry DCM (3 ml). To this was added dropwise SO_2Cl_2 (0.22 ml, 0.22 mmol, 1.0 M in DCM) over 5 min at room temperature. The resulting suspension was stirred for 1 h at room temperature and all volatiles were removed under vacuum. DCM (20 ml) was added to the precipitate, and the resulting suspension was filtered with a syringe filter to yield a light-yellow solution that was concentrated under vacuum, and slow diffusion of *n*-hexane (20 mL) at -24 °C yielded **4** as yellow blocks suitable for X-ray crystallography. Yield: 61.2 mg (0.12 mmol, 54.1%). ^1H NMR (298 K, MeCN-d_3 , 500 MHz): δ = 9.41 (s, 3H, H_2 py), 8.85 (d, J = 8.4 Hz, 3H, H_4 py), 8.79 (d, J = 4.5 Hz, 3H, H_6 py), 7.70 (dd, J = 4.5/8.4 Hz, 3H, H_5 py). $^{13}\text{C}\{^1\text{H}\}$ NMR (298 K, MeCN-d_3 , 100.6 MHz): δ = 155.46 (C_3 py), 153.94 (C_2 py), 153.07 (C_6 py), 142.70 (C_3 py), 128.77 (C_5 py). Elemental analysis (%) calcd for $\text{Cl}_2\text{Bi}(3\text{N-py})_3$ ($\text{C}_{15}\text{H}_{12}\text{N}_3\text{BiCl}_2$): C 35.0, H 2.4, N 8.2. Found: C 35.2, H 2.5, N 8.2. HR-MS [MALDI, positive ion mode MALDI-TOF]: m/z for $\text{C}_{15}\text{H}_{13}\text{N}_3\text{BiCl}$ [$\text{ClBi}(3\text{N-py})_3$] $^+$ calc: 478.0518. Found: 478.0510 (-1.7 ppm error).

Synthesis of 3-Zn: A Schlenk tube was charged with **3** (10 mg, 0.023 mmol) and ZnTPP (47.72 mg, 0.070 mmol), and 2 ml of CHCl_3 was then added. The resulting dark-purple solution was stirred for 1 hour at r.t. The solution was filtered with a syringe filter into a narrow Schlenk flask under a N_2 atmosphere, and slow diffusion of hexane (20 ml) at r.t. yielded **3-Zn** as purple blocks suitable for X-ray crystallography that were dried under vacuum. Yield (calculated as $\{[(\text{Cl}_2\text{Sb}(3\text{-py})_3)]\cdot(\text{ZnTPP})_3\}$, based on elemental analysis that indicates complete solvent loss from the crystal) 32.3 mg (0.013 mmol, 57.0%). ^1H NMR (298 K, CDCl_3 , 500 MHz): δ = 8.80 (s, 24H, H_{13}), 8.06 (d, J = 7.3 Hz, 24H, H_9 Ph), 7.70 (t, J = 7.5 Hz, 12H, H_7 Ph), 7.60 (t, J = 7.5 Hz, 24H, H_8 Ph), 6.87 (br, 3H, H_4 py), 6.12 (br, 3H, H_5 py), 4.70 (br, 6H, H_6 + H_2 py). $^{13}\text{C}\{^1\text{H}\}$ NMR (298 K, CDCl_3 , 100.6 MHz): δ = 150.14 (C_{12}), 149.14/148.40 (C_2 + C_6 py), 143.16 (C_{10} Ph), 141.06 (C_4 py), 134.63 (C_9 Ph), 134.08 (C_3 py), 131.93 (C_{13}), 127.43 (C_7 Ph), 126.50 (C_8 Ph), 124.02 (C_5 py), 120.94 (C_5 py). Elemental analysis (%) calcd for **3-Zn** ($\text{C}_{147}\text{H}_{96}\text{Cl}_2\text{N}_{15}\text{SbZn}_3$): C 71.7, H 3.9, N 8.5. Found: C 71.4, H 4.2, N 8.3.

Synthesis of 3-Mg: A Schlenk tube was charged with **3** (30 mg, 0.070 mmol) and MgTPP (45 mg, 0.070 mmol), and 2 ml of CHCl_3 was then added. The resulting dark-purple solution was stirred for 1 hour at r.t. The solution was filtered with a syringe filter into a narrow Schlenk flask under a N_2 atmosphere, and slow diffusion of hexane (20 ml) at r.t. yielded **3-Mg** as purple blocks suitable for X-ray crystallography that were dried under vacuum. Yield: 25.3 mg (0.023 mmol, 34%). ^1H NMR (298 K, CDCl_3 , 500 MHz): δ = 8.81 (s, 8H, H_{13}), 8.10 (d, J = 7.7 Hz, 8H, H_9 Ph), 7.86 (d, J = 7.6 Hz, 3H, H_4 py), 7.71 (t, J = 7.7 Hz, 4H, H_7 Ph), 7.64 (t, J = 7.6 Hz, 8H, H_8 Ph), 7.40/7.03 (br, 3H/3H, H_2 + H_6 py), 6.91 (br, 3H, H_5 py). $^{13}\text{C}\{^1\text{H}\}$ NMR (298 K, CDCl_3 , 100.6 MHz): δ = 152.14/151.09 (C_2 + C_6 py), 150.01 (C_{12}), 143.71 (C_{10} py), 141.66 (C_4 py), 135.19 (C_3 py), 134.85 (C_9 Ph), 132.06 (C_{13}), 127.21 (C_7 Ph), 126.38 (C_8 Ph), 124.70 (C_5 py), 121.85 (C_{11}). Elemental analysis (%) calcd for **3-Mg** ($\text{C}_{59}\text{H}_{40}\text{Cl}_2\text{MgN}_7\text{Sb}$): C 66.6, H 3.8, N 9.2. Found: C 66.1, H 4.1, N 8.9.

NMR studies and spectra

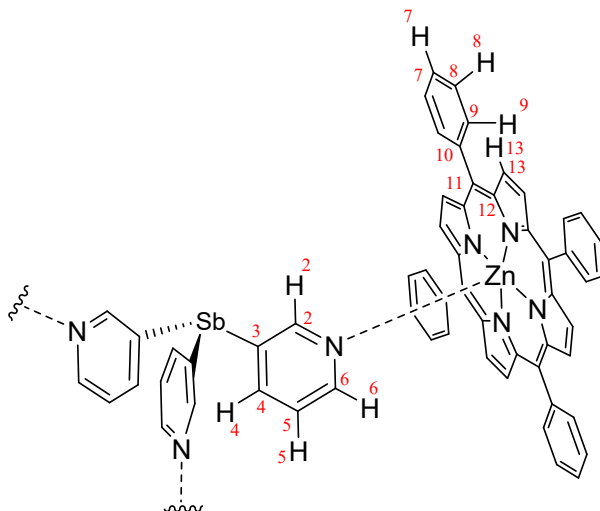


Figure S1. Compound $1\cdot\text{Zn}$, $\{[(\text{Sb}(3\text{-py})_3)]\cdot(\text{ZnTPP})_3\}$, with the atom labelling used in the NMR studies.

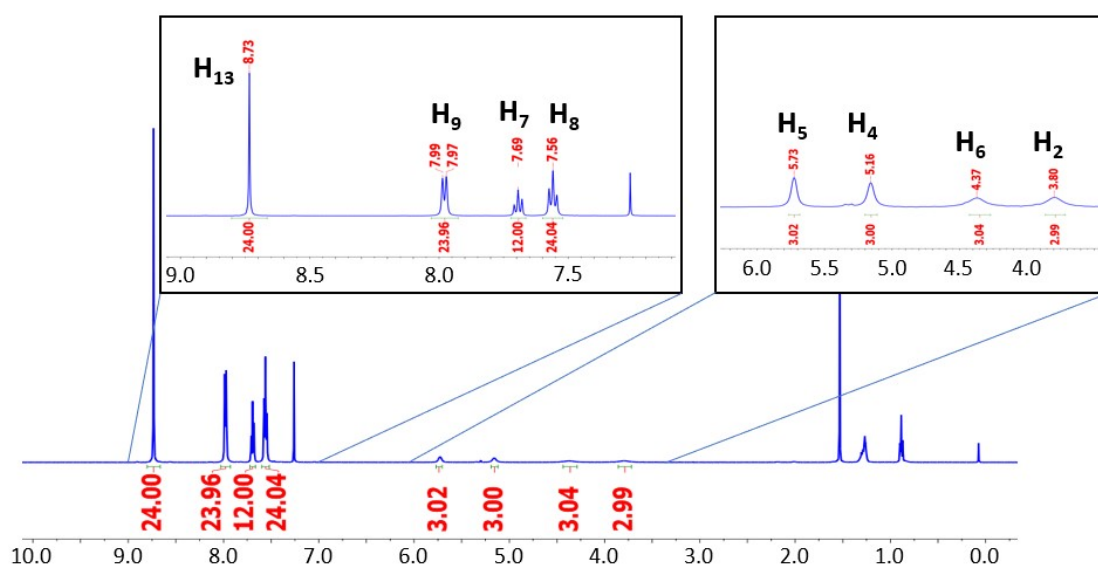


Figure S2. ^1H NMR (298 K, CDCl_3 , 500 MHz) spectrum of $1\cdot\text{Zn}$.

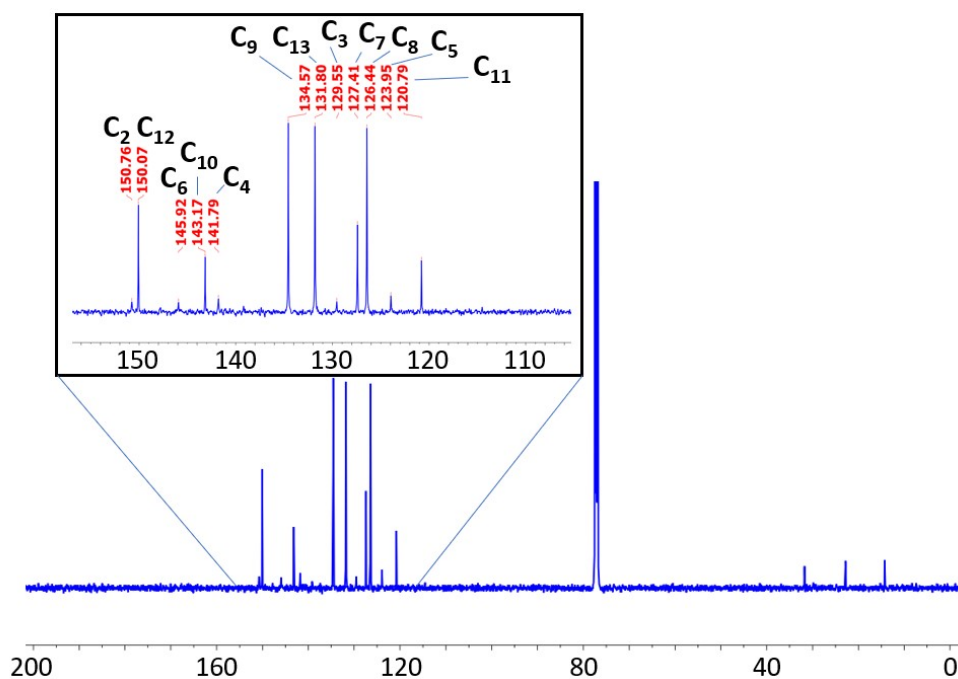


Figure S3. $^{13}\text{C}\{^1\text{H}\}$ NMR (298 K, CDCl_3 , 100.5 MHz) spectrum of $1\cdot\text{Zn}$.

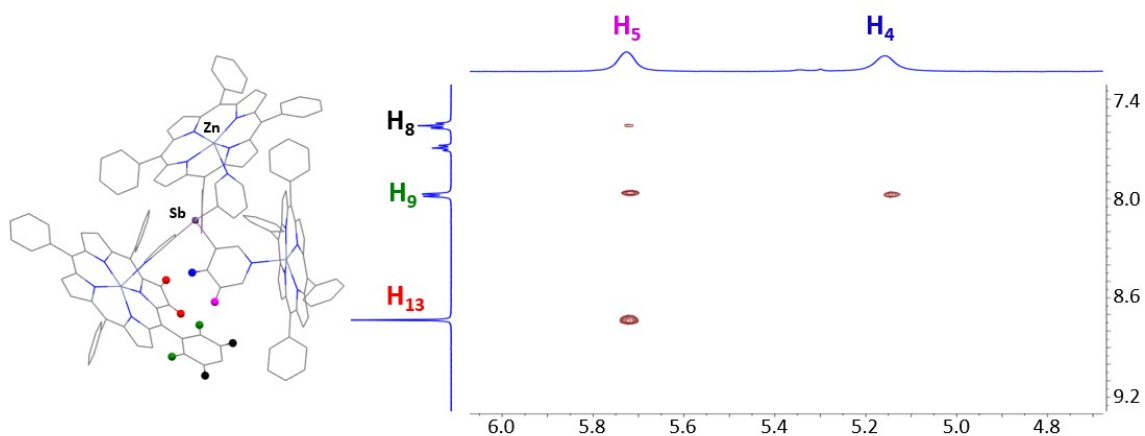


Figure S4. Selected region of the ^1H - ^1H NOESY (298 K, CDCl_3 , mixing time of 800 ms) spectrum of $1\cdot\text{Zn}$. Crosspeaks observed between H_8 and H_9 with H_{13} and pyridinic H_4 protons and between H_9 and pyridinic H_5 arise from intramolecular cross-relaxation of protons that are close to each other in space, confirming the presence of N-Zn linkage in solution.

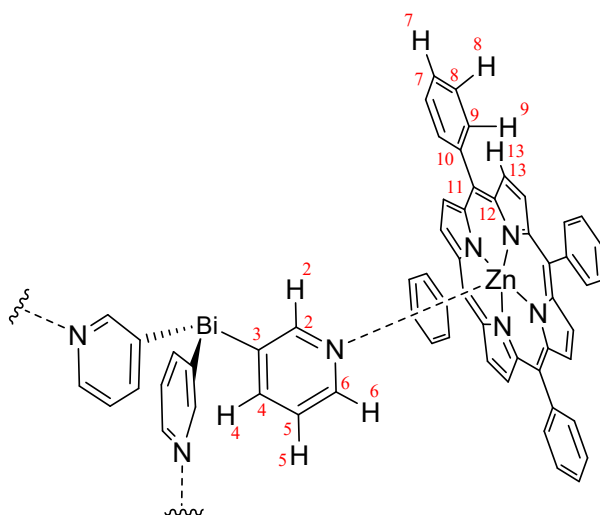


Figure S5. Compound **2-Zn**, $\{[(\text{Bi}(3\text{-py})_3)] \cdot (\text{ZnTPP})_3\}$, with the atom labelling used in the NMR studies.

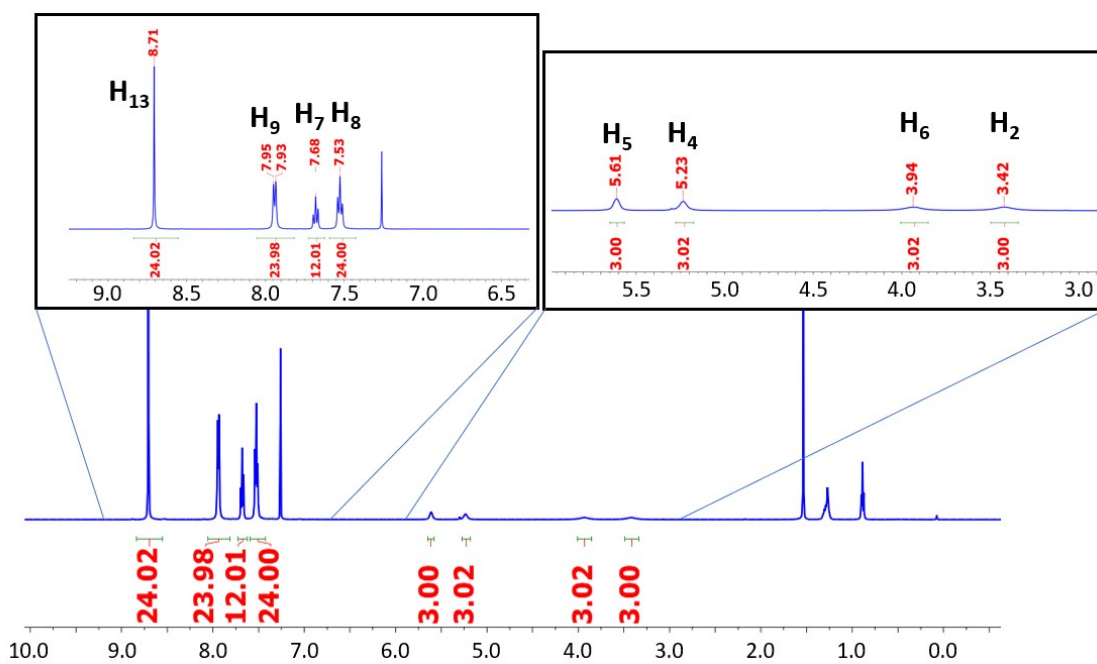


Figure S6. ^1H NMR (298 K, CDCl_3 , 500 MHz) spectrum of **2-Zn**.

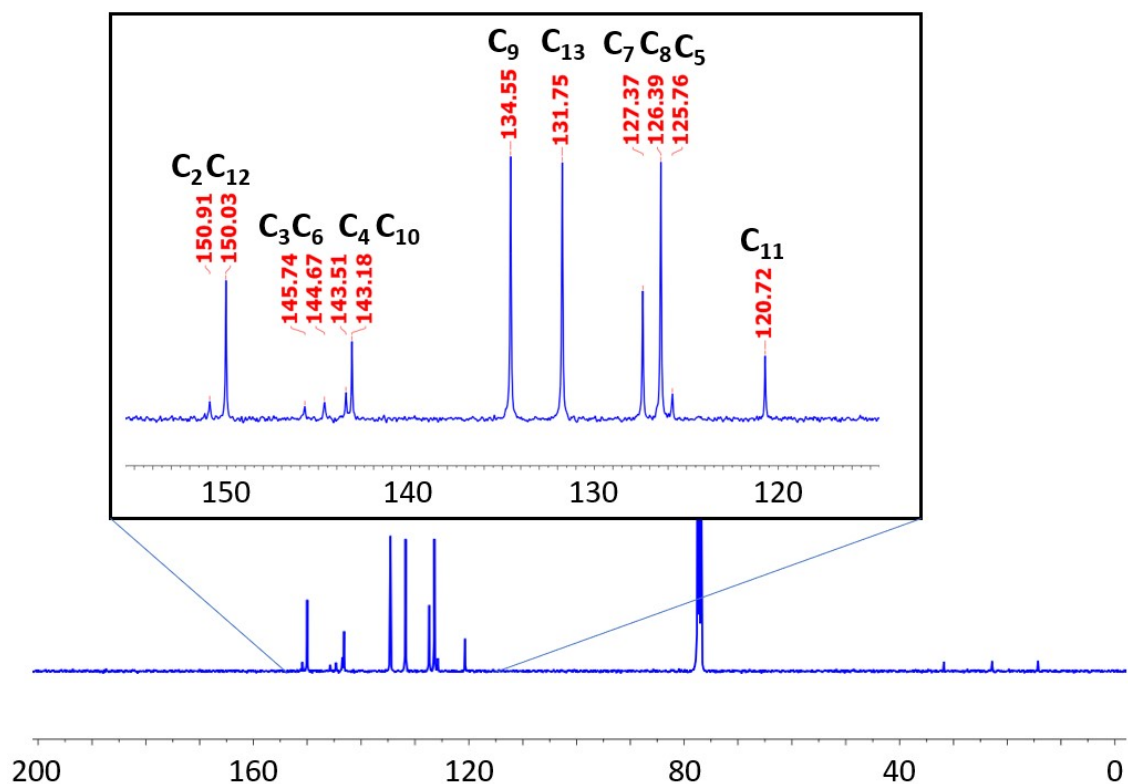


Figure S7. $^{13}\text{C}\{^1\text{H}\}$ NMR (298 K, CDCl_3 , 100.5 MHz) spectrum of $2\cdot\text{Zn}$.

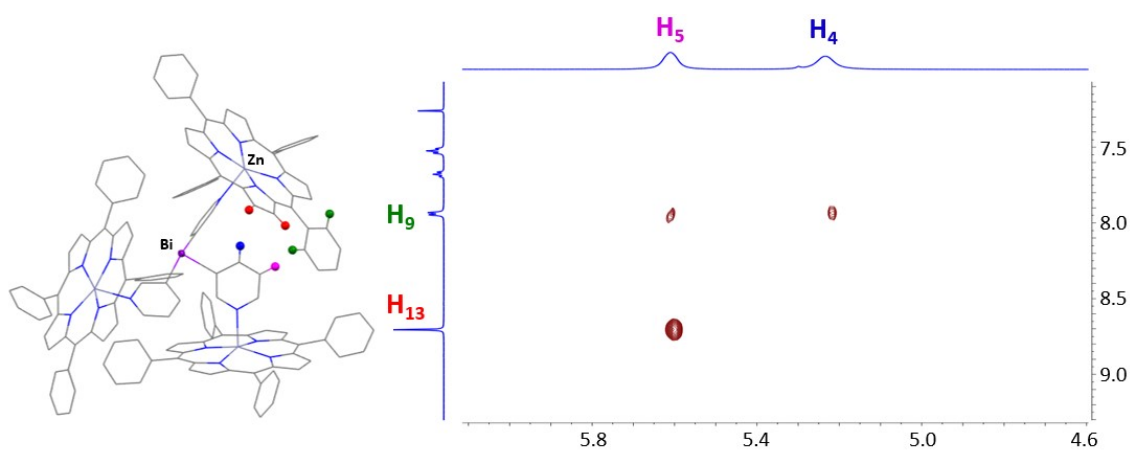


Figure S8. Selected region of the $^1\text{H}\text{-}^1\text{H}$ NOESY (298 K, CDCl_3 , mixing time of 800 ms) spectrum of $2\cdot\text{Zn}$. Crosspeaks observed between H_{13} and pyridinic H_4 protons and between H_9 and H_{13} with pyridinic H_5 arise from intramolecular cross-relaxation of protons that are close to each other in space, confirming the presence of N-Zn linkage in solution.

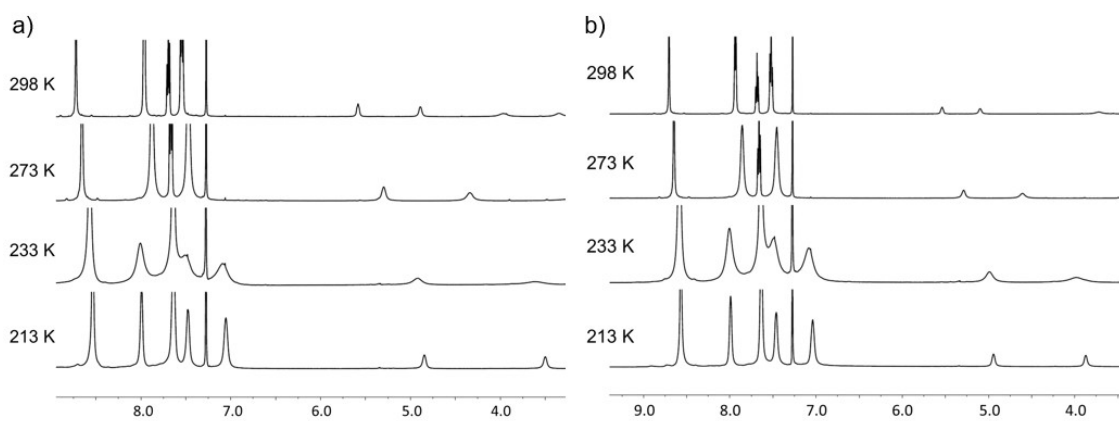


Figure S9. Stacked ¹H NMR spectra of a sample of (a) 1·Zn and (b) 2·Zn in CDCl₃ at 298, 273, 233 and 213 K.

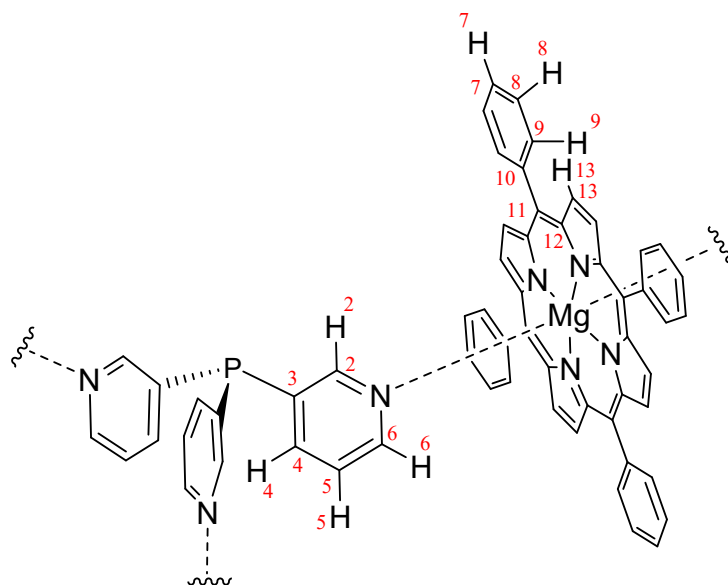


Figure S10. Compound $P \cdot Mg$, $\{[P(3-py)_2]_2 \cdot (MgTPP)_3\}_n$, with the atom labelling used in the NMR studies.

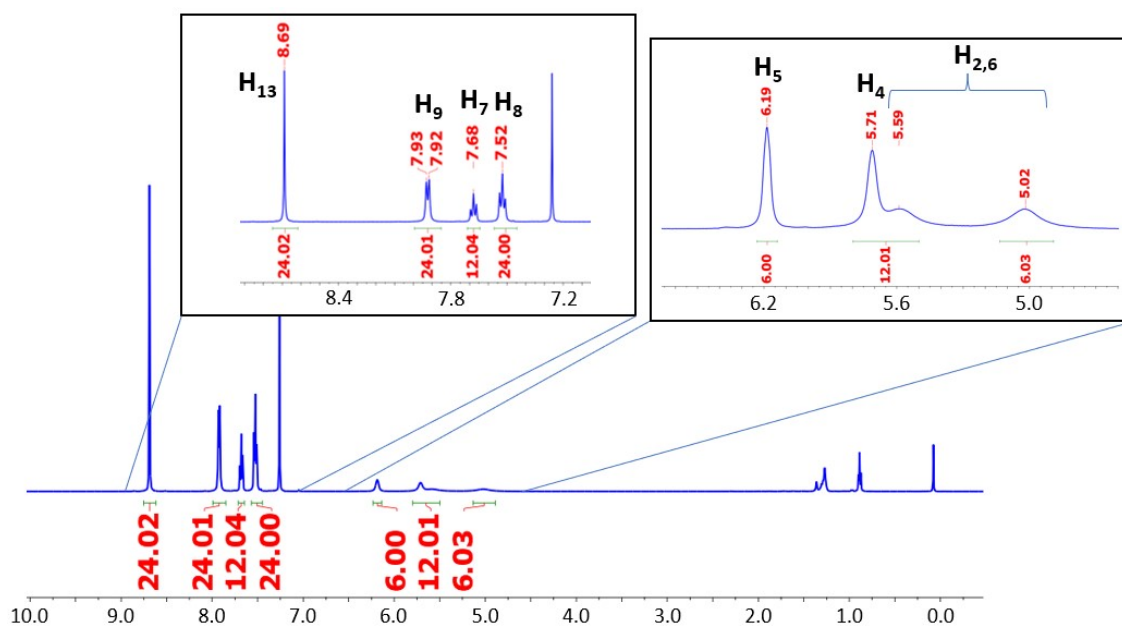


Figure S11. 1H NMR (298 K, $CDCl_3$, 500 MHz) spectrum of $P \cdot Mg$.

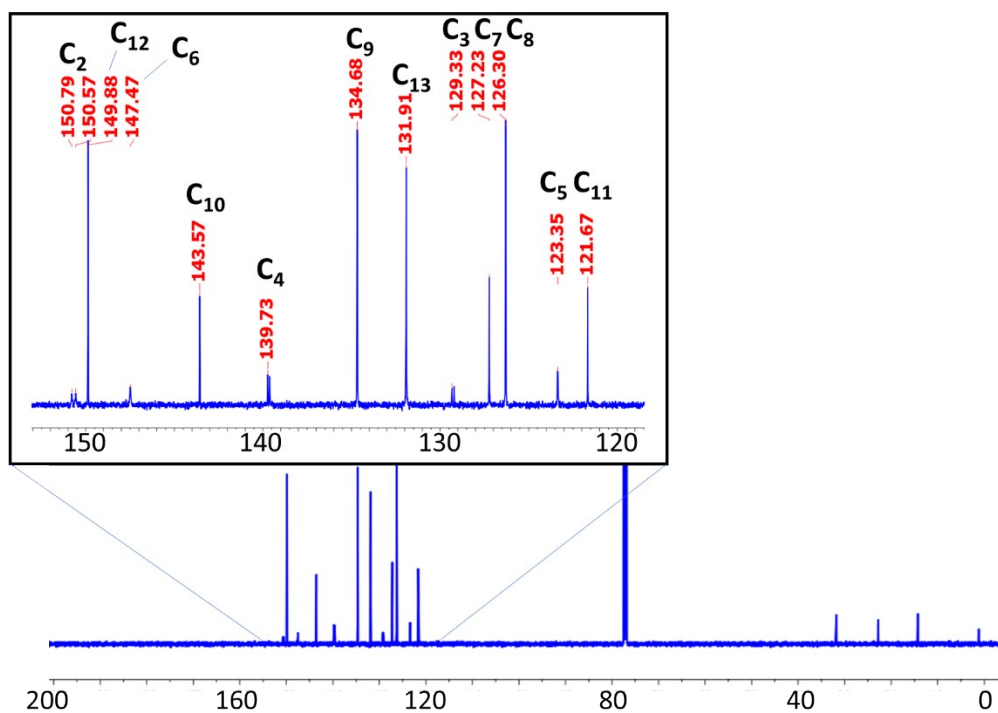


Figure S12. $^{13}\text{C}\{^1\text{H}\}$ NMR (298 K, CDCl_3 , 100.5 MHz) spectrum of $\text{P}\cdot\text{Mg}$.

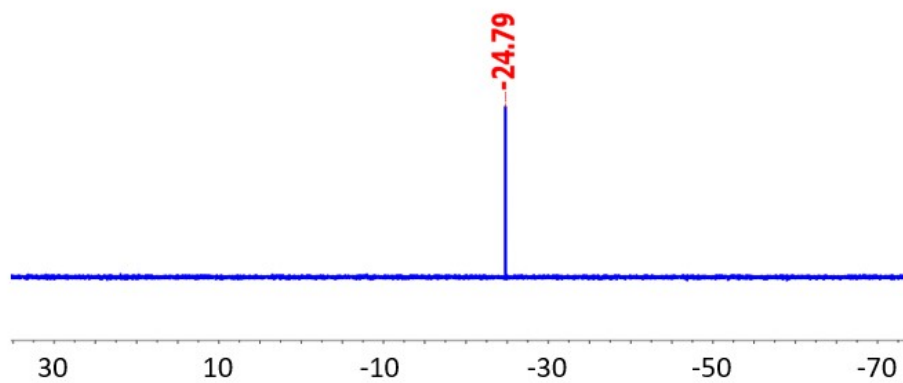


Figure S13. $^{31}\text{P}\{^1\text{H}\}$ NMR (298 K, CDCl_3 , 202.5 MHz) spectrum of $\text{P}\cdot\text{Mg}$.

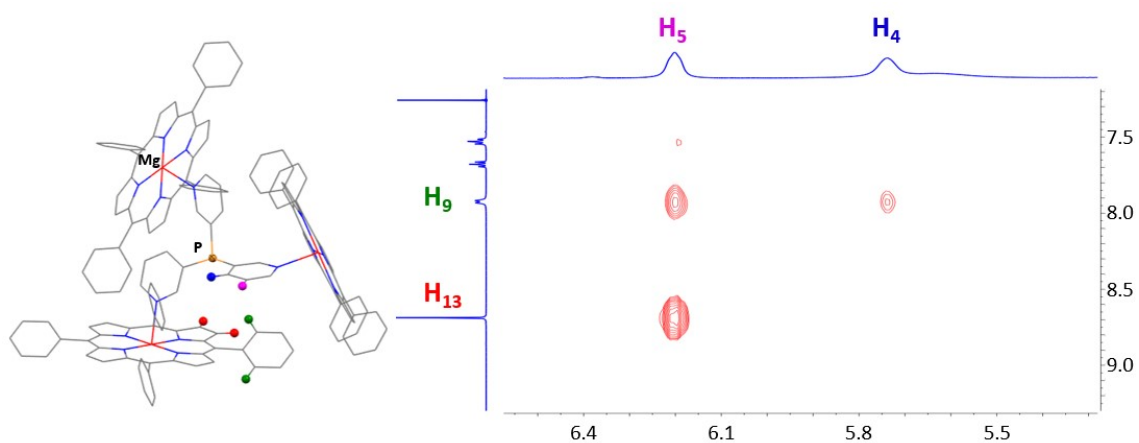


Figure S14. Selected region of the ^1H - ^1H ROESY (298 K, CDCl_3) spectrum of $\text{P}\cdot\text{Mg}$. Crosspeaks observed between H_9 and H_4 with pyridinic H_5 protons and between H_9 with pyridinic H_4 arise from intramolecular cross-relaxation of protons that are close to each other in space, confirming the presence of N-Mg linkage in solution.

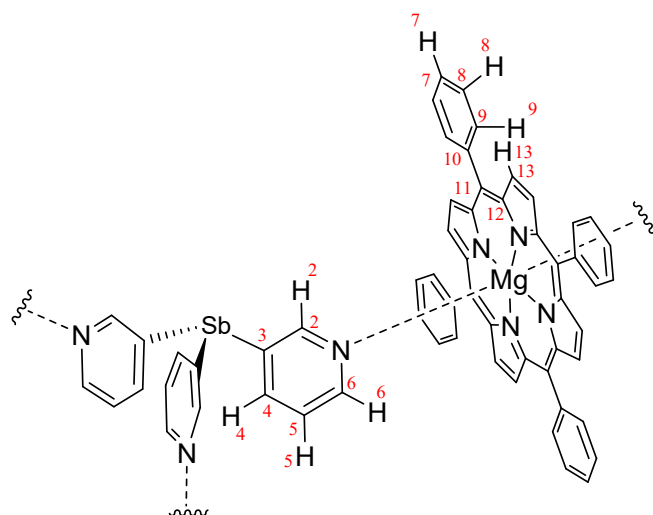
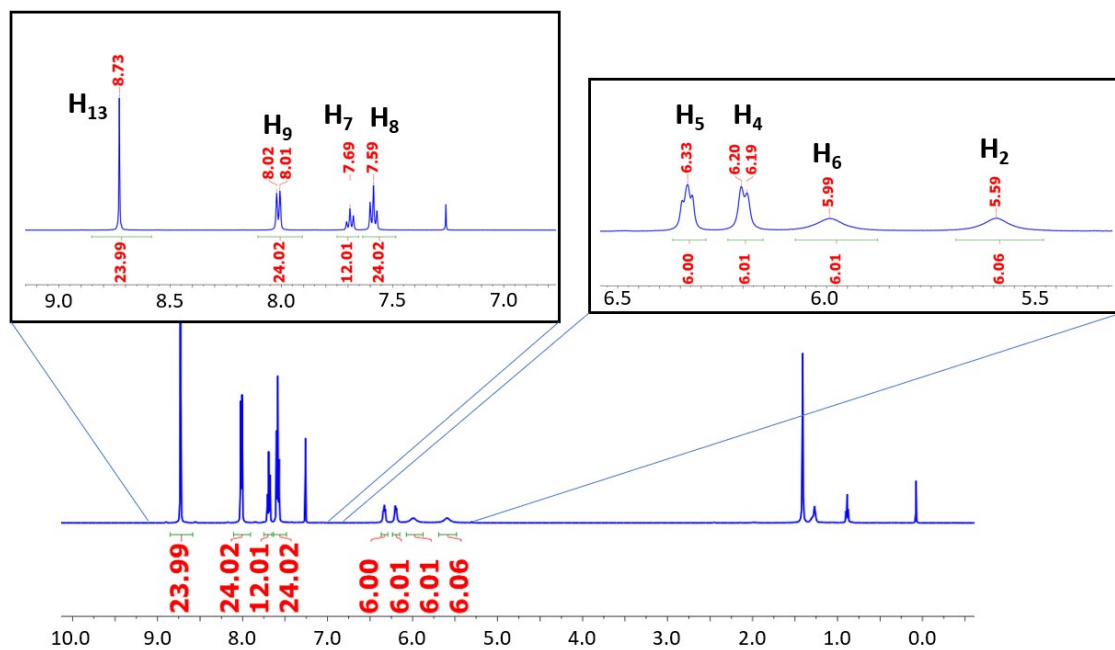
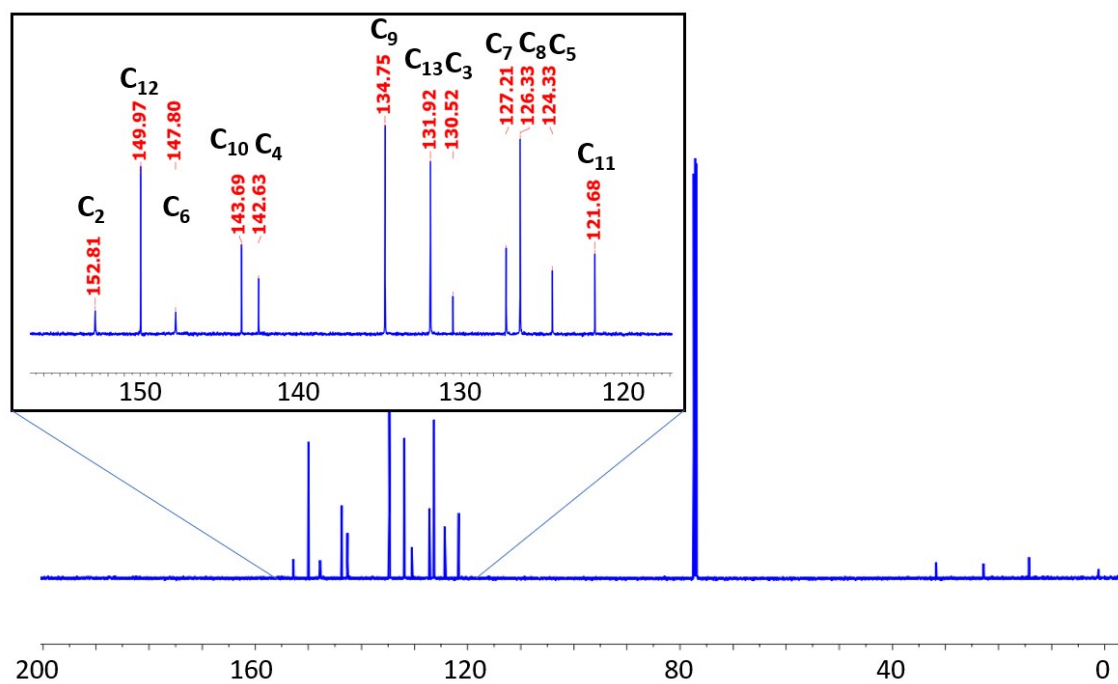


Figure S15. Compound $1\cdot\text{Mg}$, $\{[\text{Sb}(3\text{-py})_3]_2\cdot(\text{MgTPP})_3\}_n$, with the atom labelling used in the NMR studies.

Figure S16. ^1H NMR (298 K, CDCl_3 , 500 MHz) spectrum of $1\cdot\text{Mg}$.Figure S17. $^{13}\text{C}\{^1\text{H}\}$ NMR (298 K, CDCl_3 , 100.5 MHz) spectrum of $1\cdot\text{Mg}$.

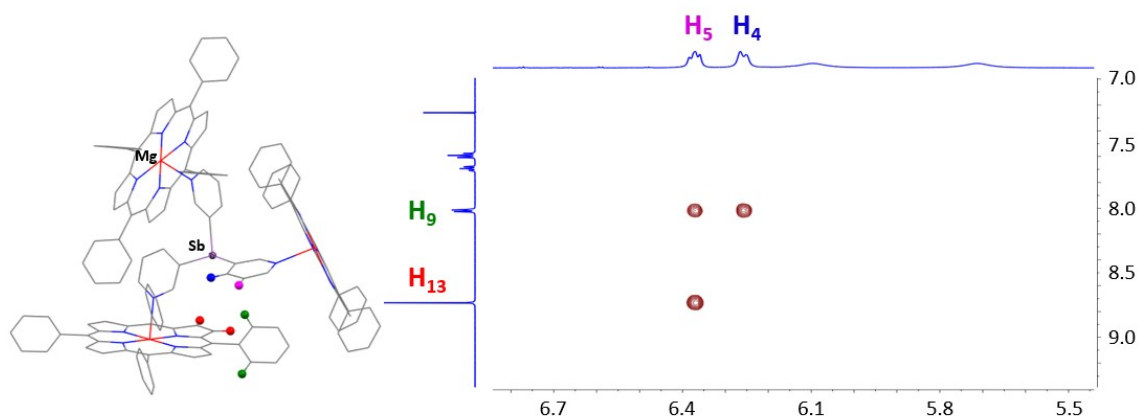


Figure S18. Selected region of the ^1H - ^1H NOESY (298 K, CDCl_3 , mixing time of 800 ms) spectrum of $1 \cdot \text{Mg}$. Crosspeaks observed between H_9 and H_{13} with pyridinic H_5 protons and between H_9 with pyridinic H_4 arise from intramolecular cross-relaxation of protons that are close to each other in space, confirming the presence of N-Mg linkage in solution.

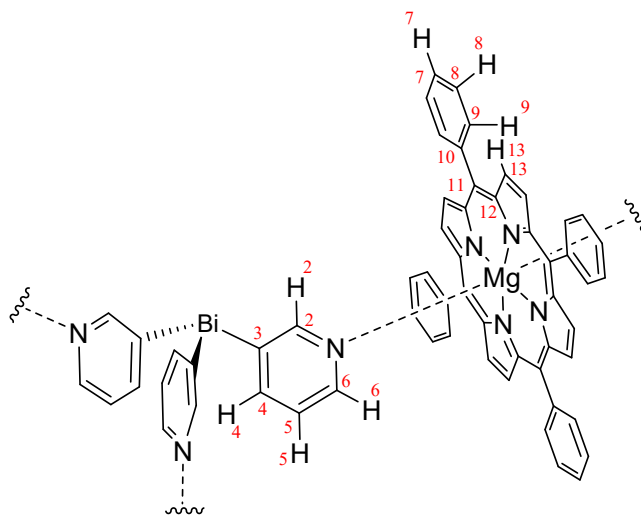


Figure S19. Compound $2 \cdot \text{Mg}$, $\{[\text{Bi}(3\text{-py})_3]_2 \cdot (\text{MgTPP})_3\}_n$, with the atom labelling used in the NMR studies.

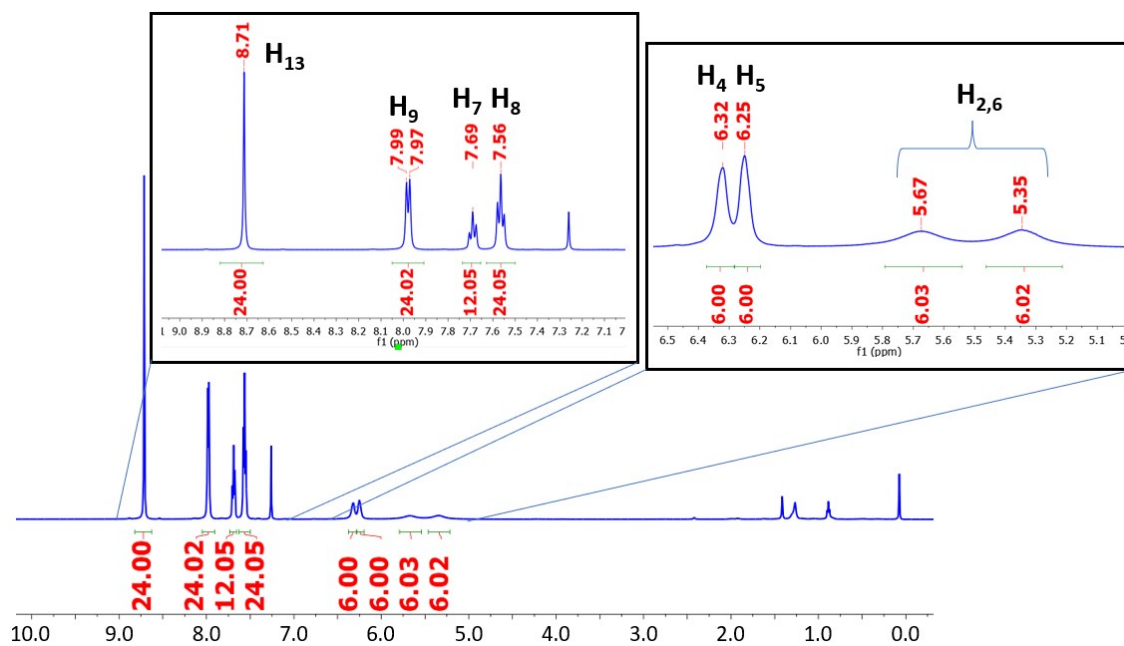


Figure S20. ^1H NMR (298 K, CDCl_3 , 500 MHz) spectrum of $2\cdot\text{Mg}$.

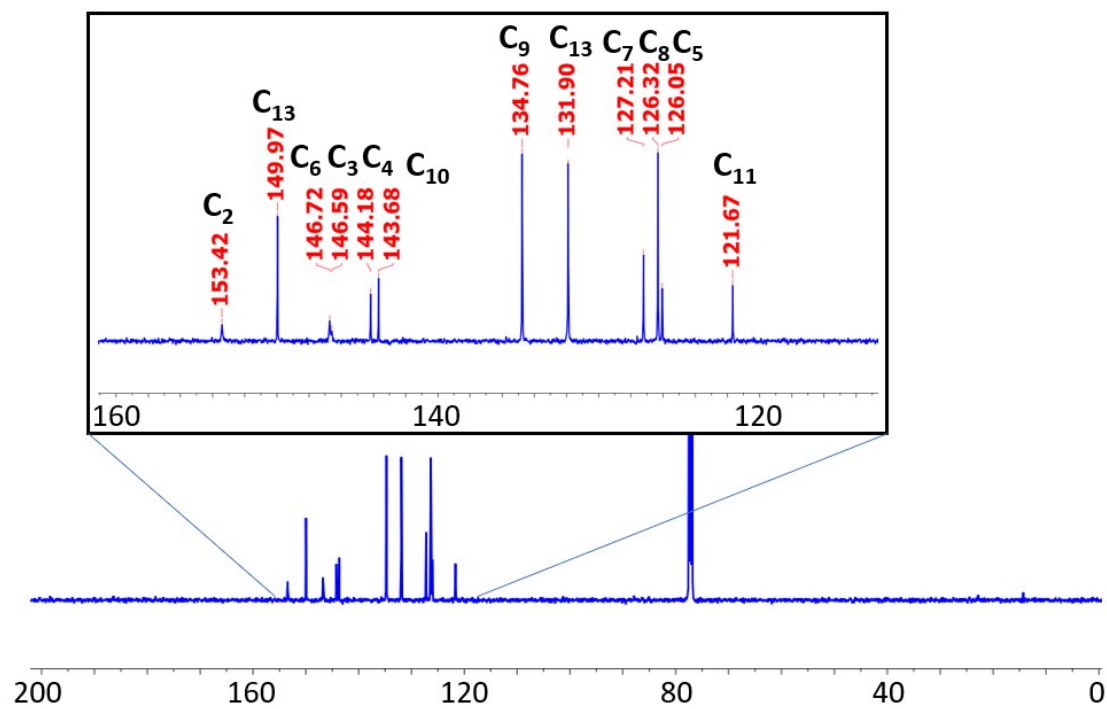


Figure S21. $^{13}\text{C}\{^1\text{H}\}$ NMR (298 K, CDCl_3 , 100.5 MHz) spectrum of $2\cdot\text{Mg}$.

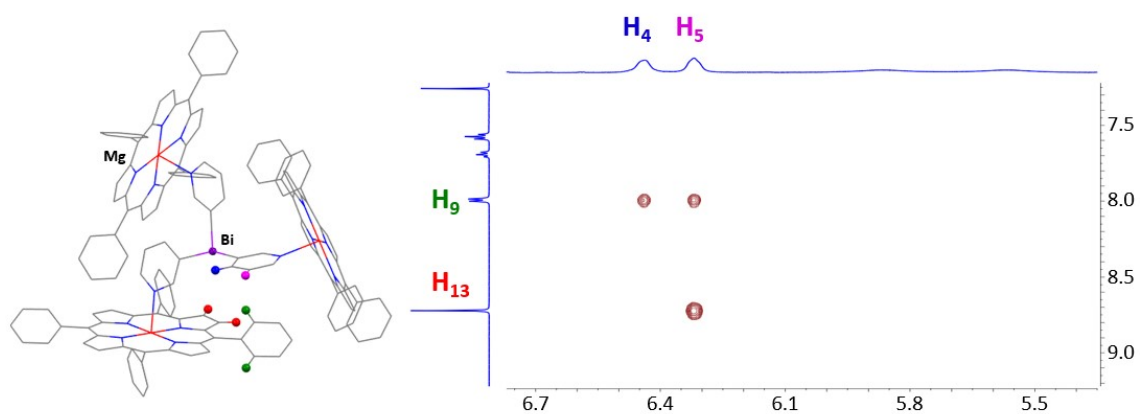


Figure S22. Selected region of the ^1H - ^1H NOESY (298 K, CDCl_3 , mixing time of 800 ms) spectrum of $2 \cdot \text{Mg}$. Crosspeaks observed between H_9 and H_{13} with pyridinic H_5 protons and between H_9 and pyridinic H_4 arise from intramolecular cross-relaxation of protons that are close to each other in space, confirming the presence of N-Mg linkage in solution.

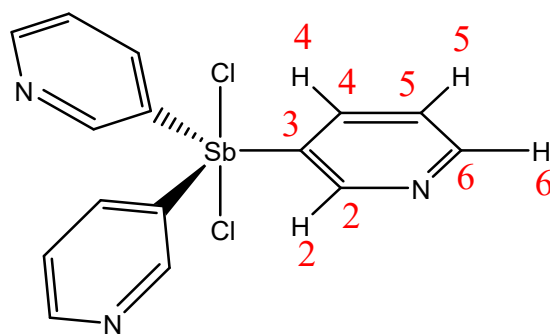


Figure S23. Compound **3** with the atom labelling used in the NMR studies.

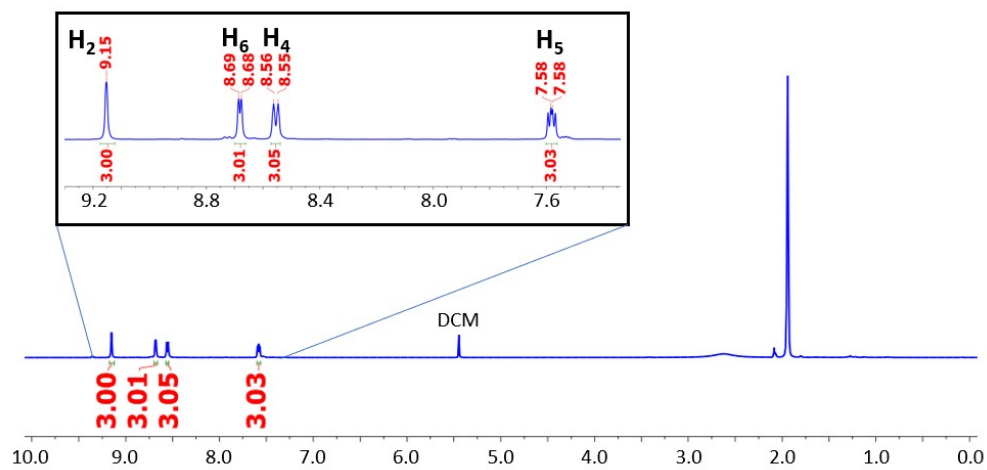


Figure S24. ^1H NMR (298 K, MeCN- d_3 , 500 MHz) spectrum of **3**.

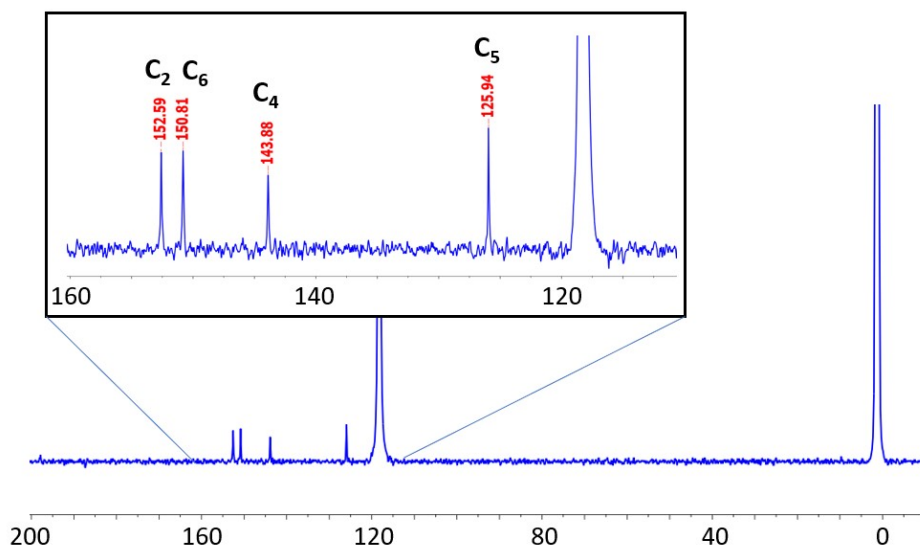


Figure S25. $^{13}\text{C}\{^1\text{H}\}$ NMR (298 K, MeCN- d_3 , 100.5 MHz) spectrum of **3**.

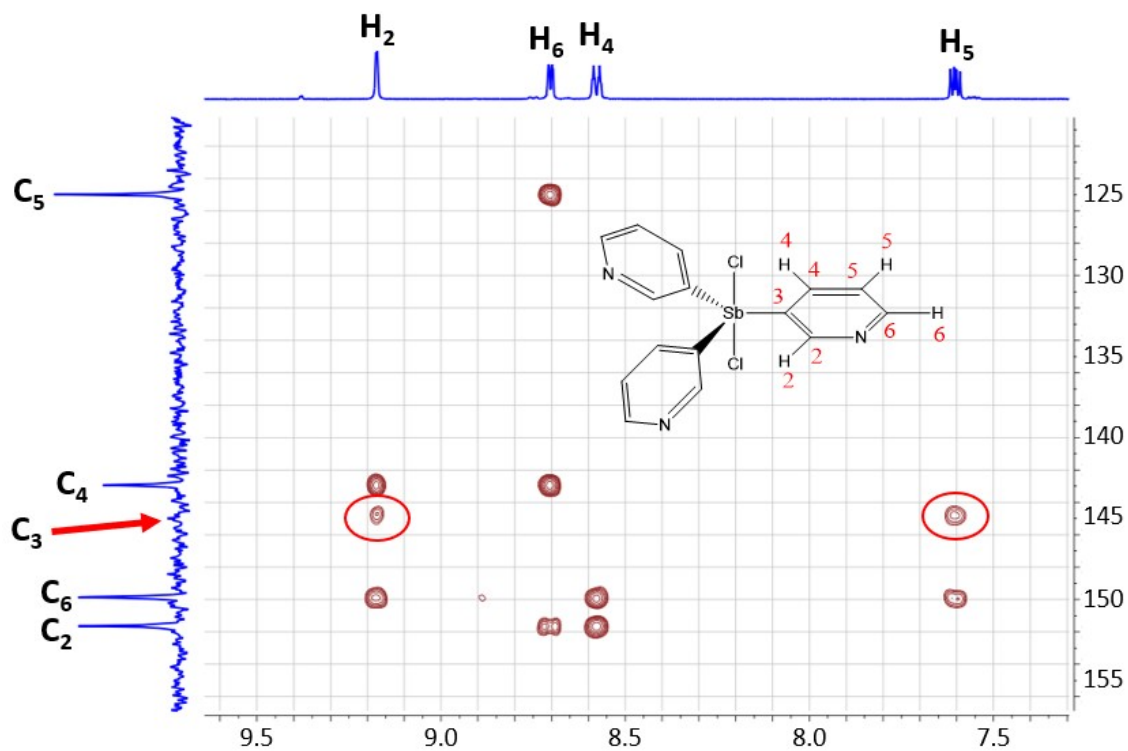


Figure S26. Selected region of the ^1H - ^{13}C HMBC (298 K, MeCN-d_3) spectrum of **3** used for the identification of the Sb-bonded carbon (C_3) (signal at 144.7 ppm).

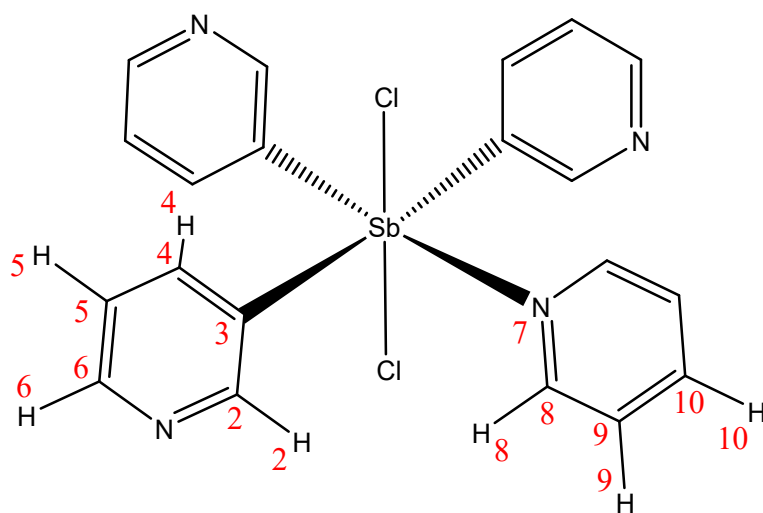


Figure S27. Compound **3**·py with the atom labelling used in the NMR studies.

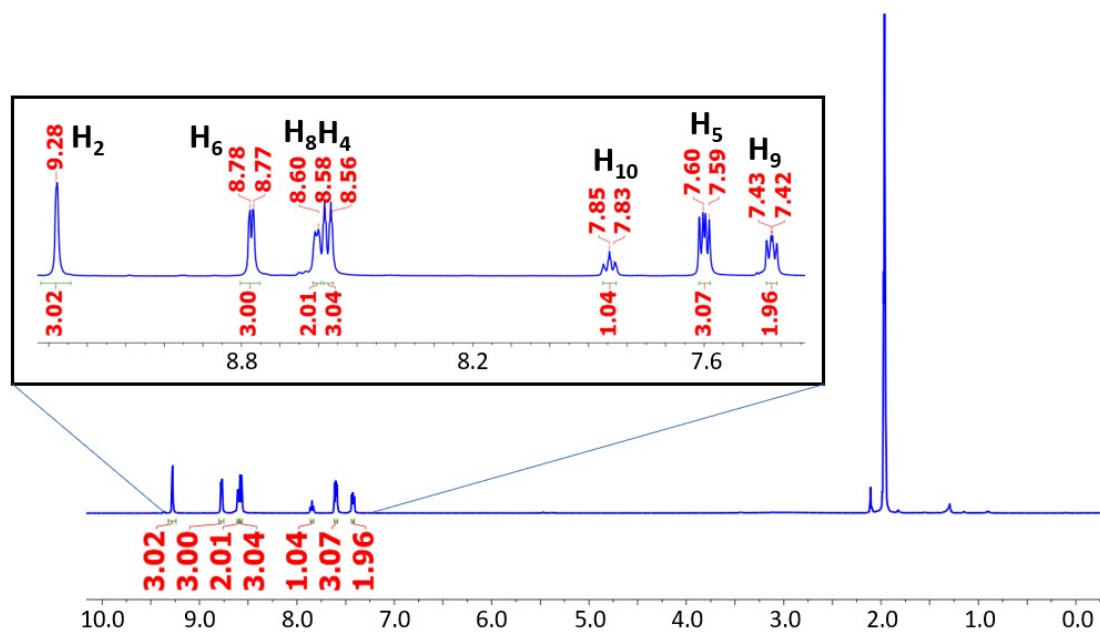


Figure S28. ¹H NMR (298 K, MeCN-d₃, 500 MHz) spectrum of 3-py.

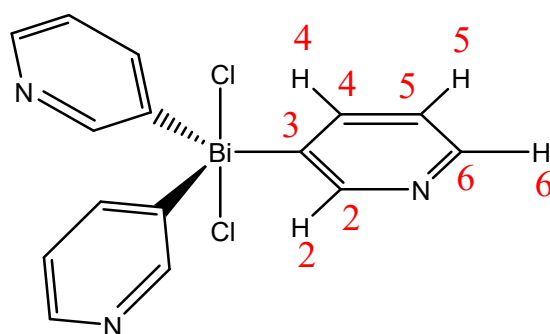


Figure S29. Compound 4 with the atom labelling used in the NMR studies.

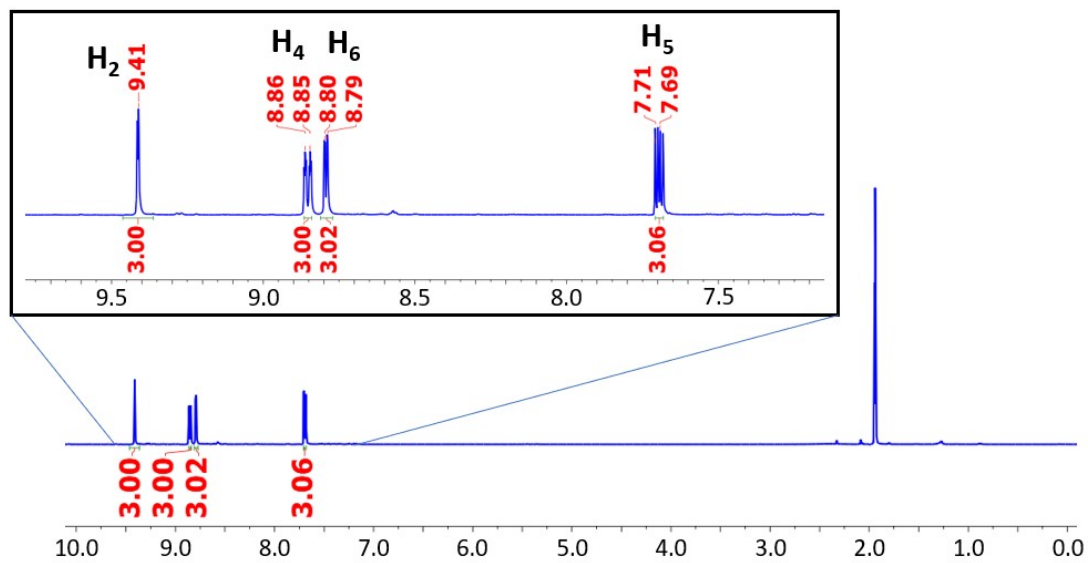


Figure S30. ^1H NMR (298 K, MeCN- d_3 , 500 MHz) spectrum of **4**.

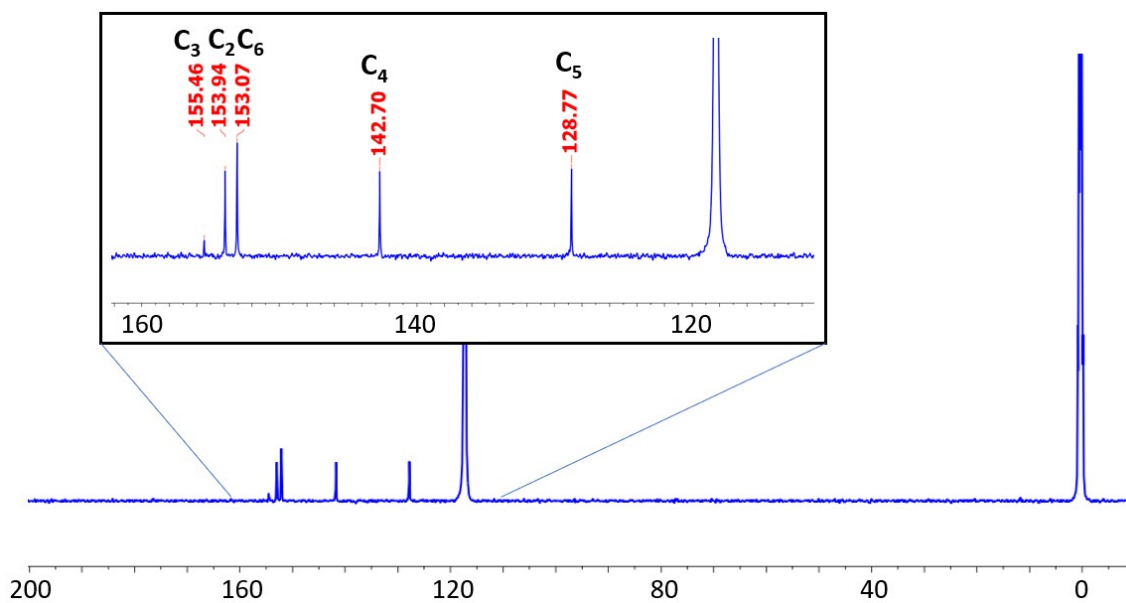


Figure S31. $^{13}\text{C}\{^1\text{H}\}$ NMR (298 K, MeCN- d_3 , 100.5 MHz) spectrum of **4**.

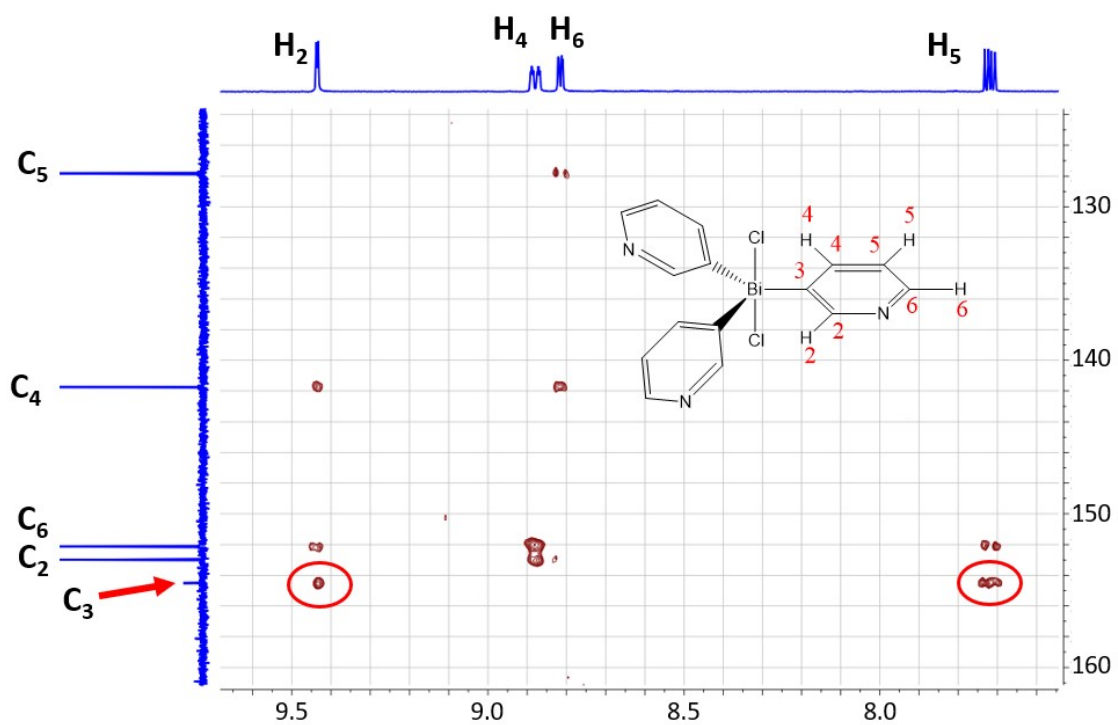


Figure S32. Selected region of the ^1H - ^{13}C HMBC (298 K, MeCN-d_3) spectrum of **4** used for the identification of the Bi-bonded carbon (C_3) (signal at 155.46 ppm).

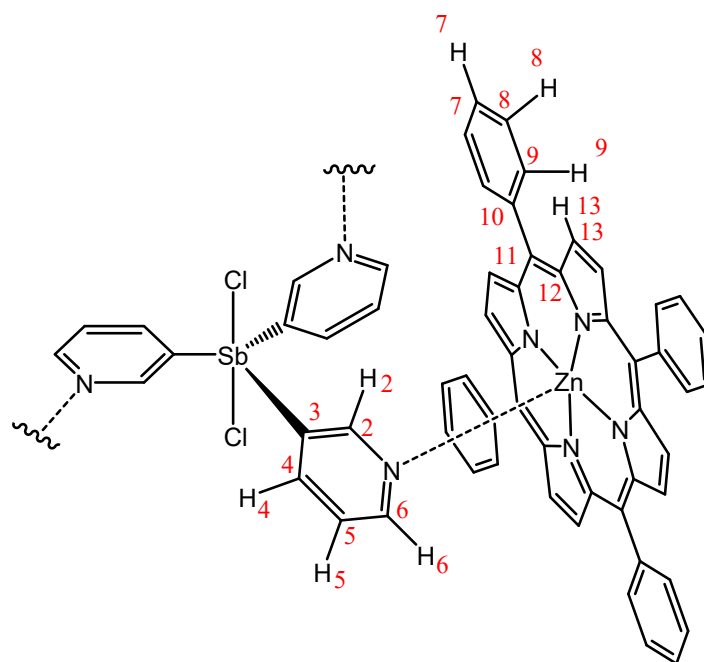


Figure S33. Compound **3**·Zn, $\{[Cl_2Sb(3-py)_3] \cdot (ZnTPP)_3\}$, with the atom labelling used in the NMR studies.

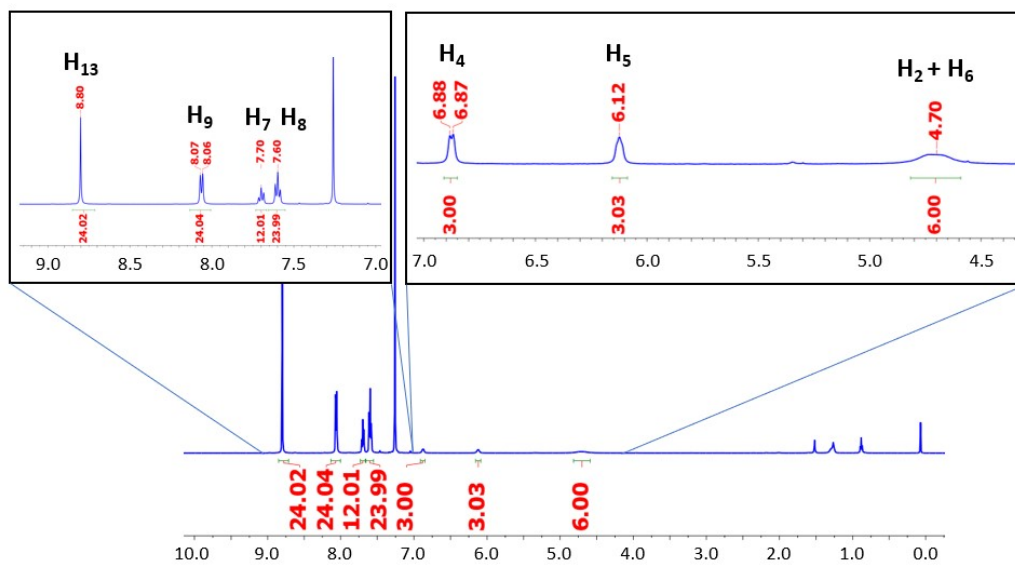


Figure S34. 1H NMR (298 K, $CDCl_3$, 500 MHz) spectrum of **3**·Zn.

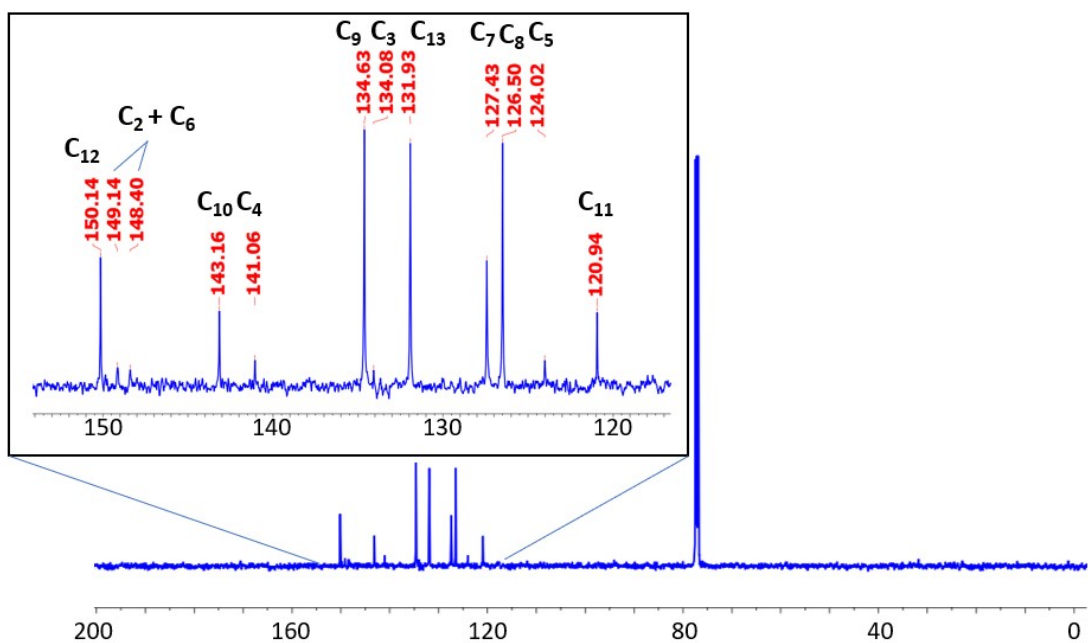


Figure S35. $^{13}\text{C}\{^1\text{H}\}$ NMR (298 K, CDCl_3 , 100.5 MHz) spectrum of $3\cdot\text{Zn}$.

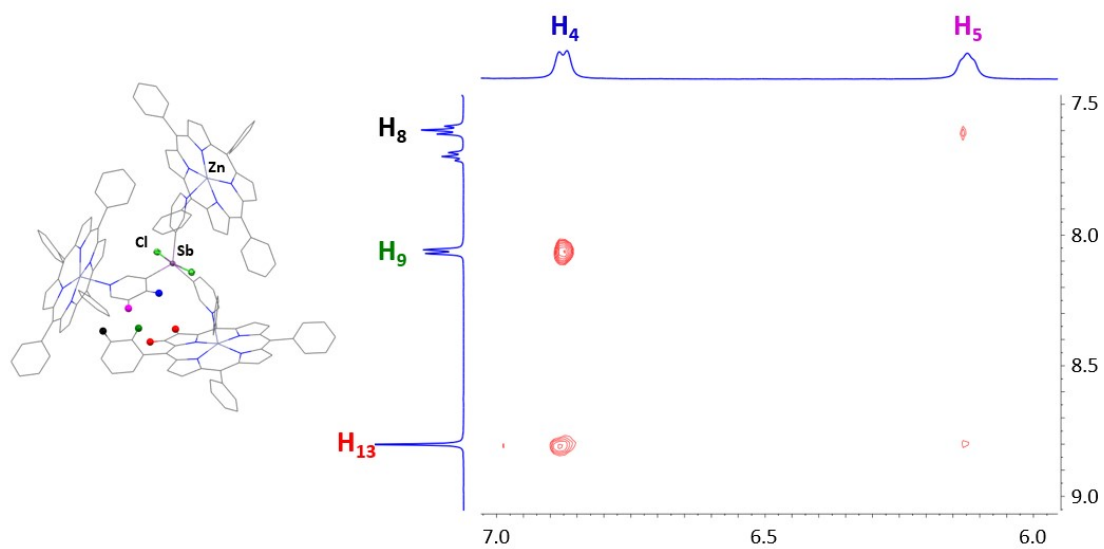


Figure S36. Selected region of the $^1\text{H}-^1\text{H}$ NOESY (298 K, CDCl_3 , mixing time of 800 ms) spectrum of $3\cdot\text{Zn}$. Crosspeaks observed between H_9 and H_{13} with pyridinic H^4 protons and between H_8 and H_{13} with pyridinic H_5 arise from intramolecular cross-relaxation of protons that are close to each other in space, confirming the presence of N-Mg linkage in solution.

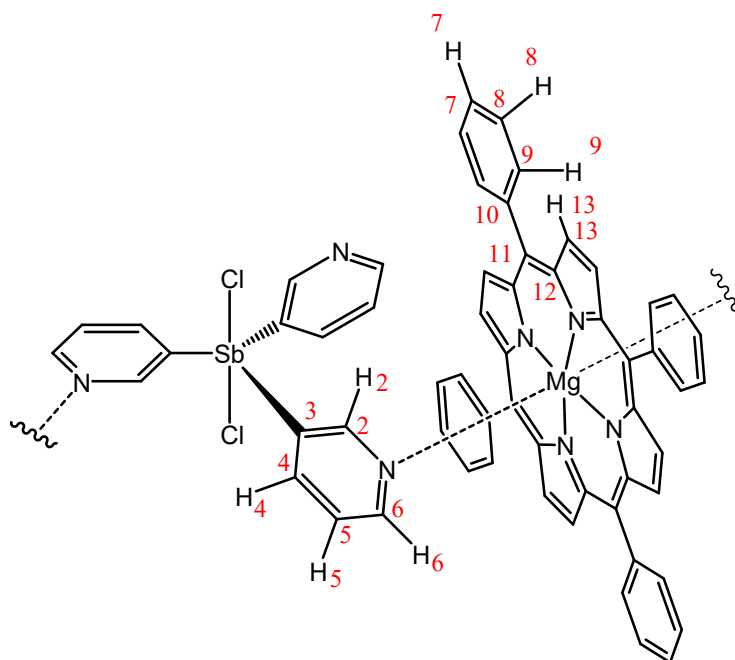


Figure S37. Compound $3 \cdot \text{Mg}$, $\{[(\text{Cl}_2\text{Sb}(3\text{-py})_3)] \cdot (\text{MgTPP})\}_n$, with the atom labelling used in the NMR studies.

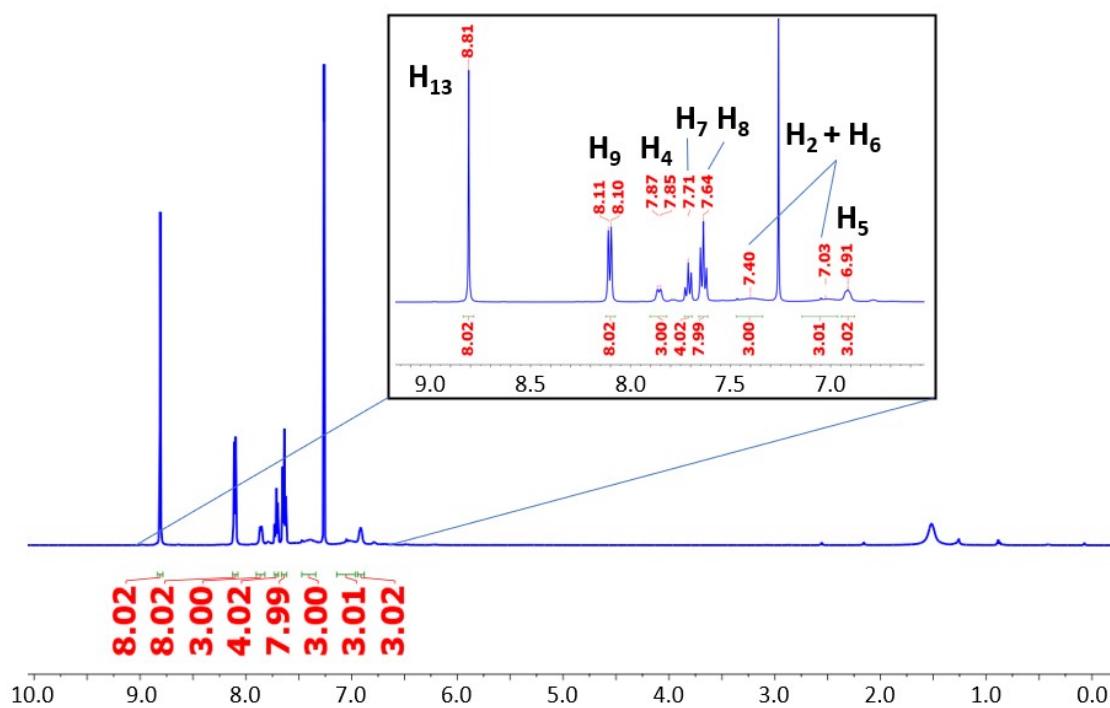


Figure S38. ^1H NMR (298 K, CDCl_3 , 500 MHz) spectrum of $3 \cdot \text{Mg}$.

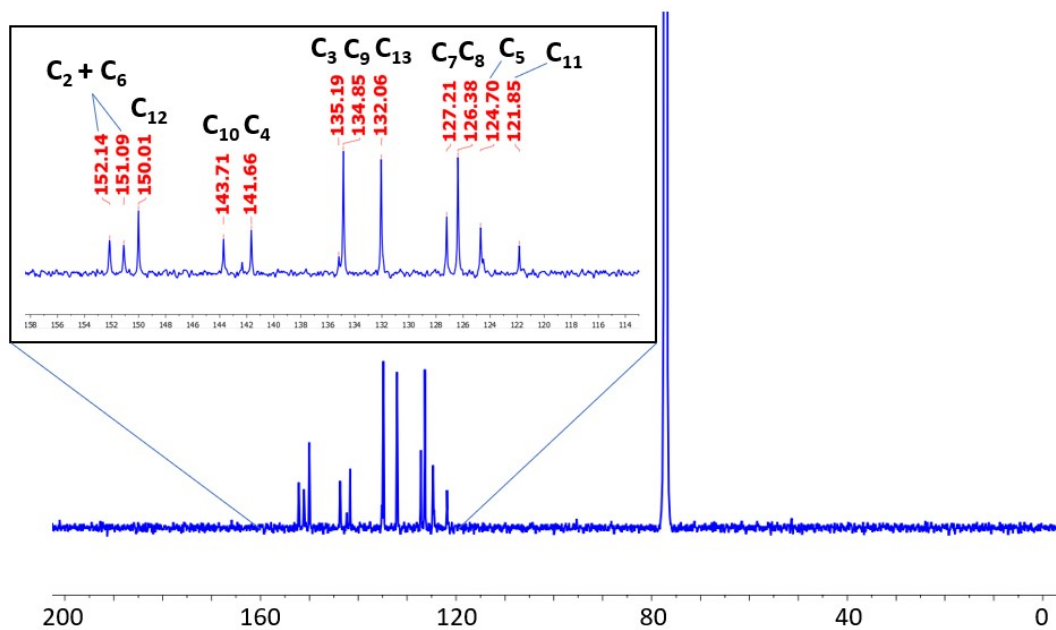


Figure S39. $^{13}\text{C}\{^1\text{H}\}$ NMR (298 K, CDCl_3 , 100.5 MHz) spectrum of 3·Mg.

DOSY Experiments

^1H -DOSY experiments were performed to estimate the hydrodynamic radii of the complexes $1\cdot\text{Zn}$ and $2\cdot\text{Zn}$ in CDCl_3 solution (Figure S40). For $1\cdot\text{Zn}$ and $2\cdot\text{Zn}$, the calculated hydrodynamic radii derived from the diffusion coefficient values ($r_{\text{H DOSY}}$) are consistent with those expected based on the crystallographic radii (typically, $r_{\text{H}} \approx 0.8r_{\text{X-ray}}$).^[7,8]

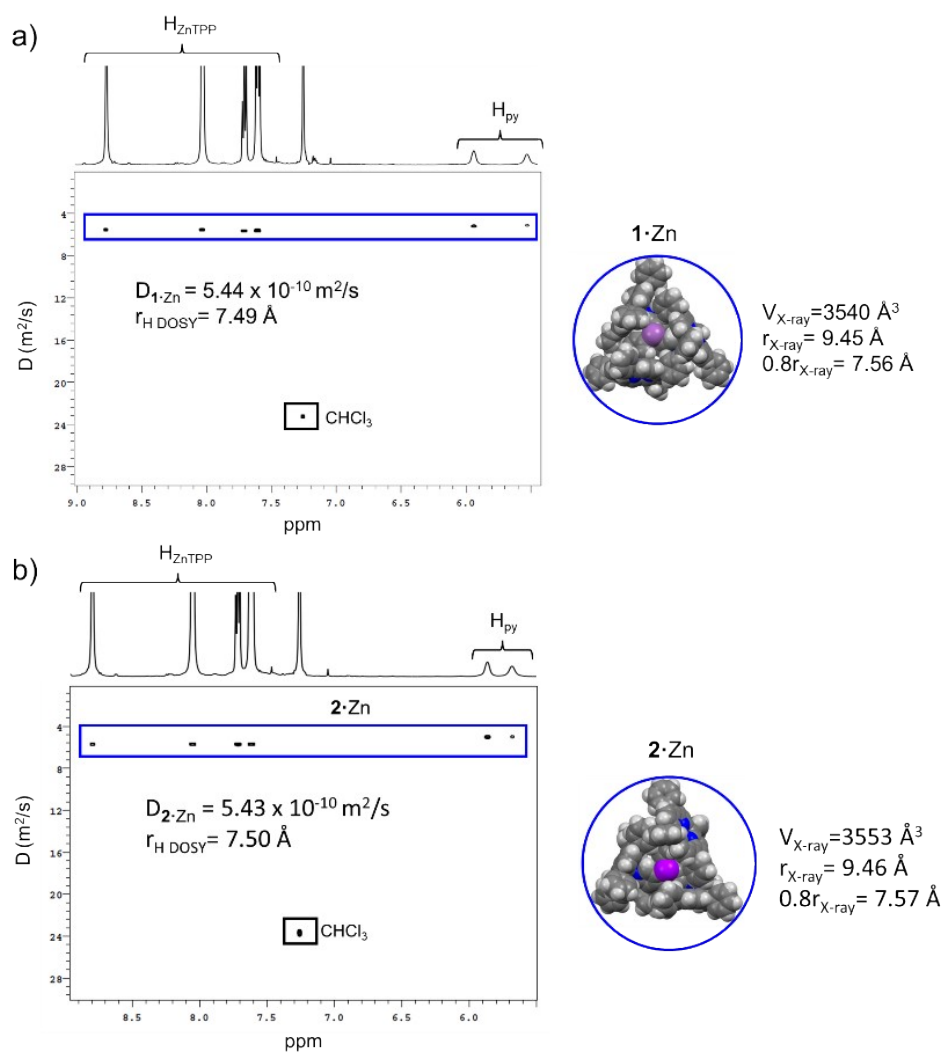


Figure S40. ^1H DOSY NMR spectra of (a) $1\cdot\text{Zn}$ and (b) $2\cdot\text{Zn}$ in CDCl_3 at 298 K. For $1\cdot\text{Zn}$ and $2\cdot\text{Zn}$, the calculated hydrodynamic radii derived from the diffusion coefficient values ($r_{\text{H DOSY}}$) are consistent with those expected based on the crystallographic radii (typically, $r_{\text{H}} \approx 0.8r_{\text{X-ray}}$, see refs 7 and 8).

In order to evaluate the aggregation state of the complexes **P**·Mg, **1**·Mg and **2**·Mg in solution, we estimated their MW using ¹H DOSY by the Stalke method ($ECC_{DSE}^{CDCl_3}$). The DOSY NMR data were analysed using the MW Estimation Software developed by Stalke.^[9-11] ¹H DOSY-ECC-MW estimation of **P**·Mg, **1**·Mg and **2**·Mg in CDCl₃ was carried out at 298 K. Adamantane was used as an internal reference.

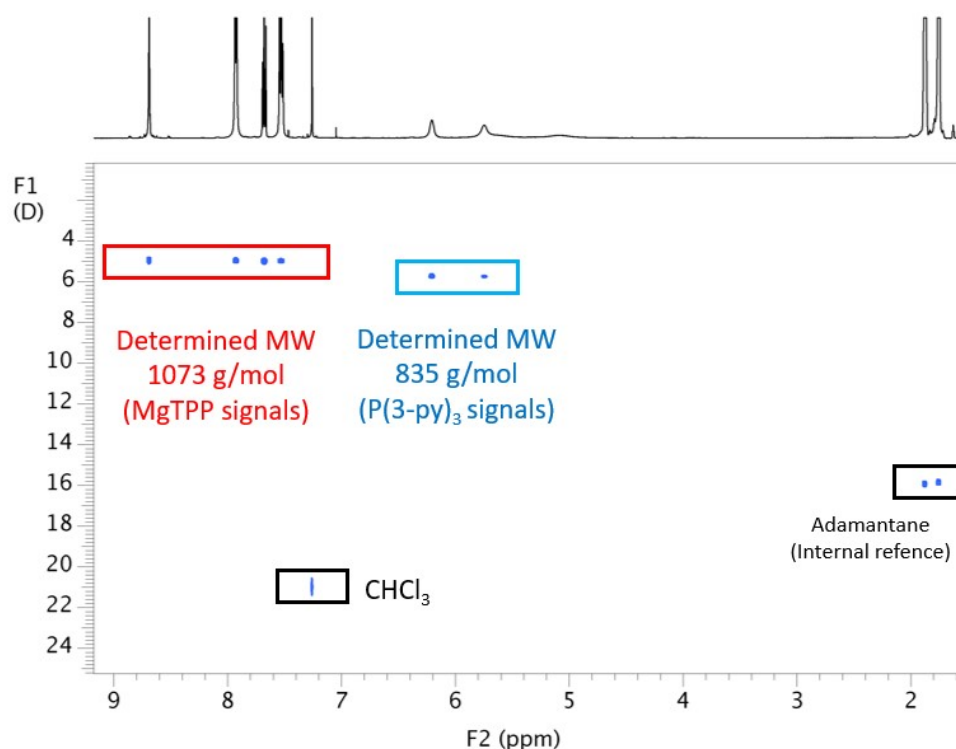


Figure S41. ¹H DOSY NMR spectrum of **P**·Mg and adamantane (internal reference) at 298 K in CDCl₃. The diffusion coefficients (*D*) corresponding to the P(3-py)₃ and MgTPP signals are highlighted in blue and red, respectively.

Compound	<i>D</i> m ² /s	log <i>D</i>	log <i>D</i> _{x, norm}	MW (g/mol)
Adamantane	1.585E-09	-8.7999	-	136.23 ^a
MgTPP	4.921E-10	-9.3079	-9.3235	1073 ^b
P(3-py) ₃	5.681E-10	-9.2456	-9.2612	835 ^b

Table S1. *D*-MW analysis using the ¹H DOSY NMR data obtained for the mixture of **P**·Mg and adamantane (internal reference) at 298 K in CDCl₃. ^aReal MW. ^bMW_{det}.

Aggregate	MW _{det} (MgTPP signals)	MW _{det} (Ligand signals)	MW _{cal} (theoretical)	MW _{Diff} [%]
P(3-py) ₃	-	835	265	-68
MgTPP	1073	-	637	-24
[P(3-py) ₃ ·MgTPP]	1073	835	902	-16 and 8
{[P(3-py) ₃] ₂ ·MgTPP}	1073	835	1168	9 and 40
[P(3-py) ₃ ·(MgTPP) ₂]	1073	835	1539	43 and 84

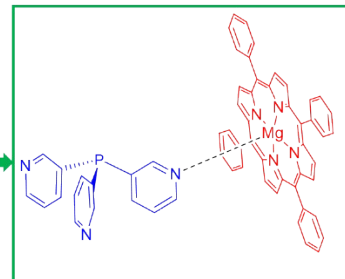


Figure S42. $ECC_{DSE}^{CDCl_3}$ was used to determine the MW_{det} of P·Mg in CDCl₃ at 298 K and the MW_{Diff} for the proposed species.

Note: The deviation is calculated as $M_{Diff} = [(MW_{cal} - MW_{det}) / MW_{det}] \times 100\%$ where MW_{det} is the experimentally determined value and MW_{cal} is the calculated molecular weight for the hypothetical species.

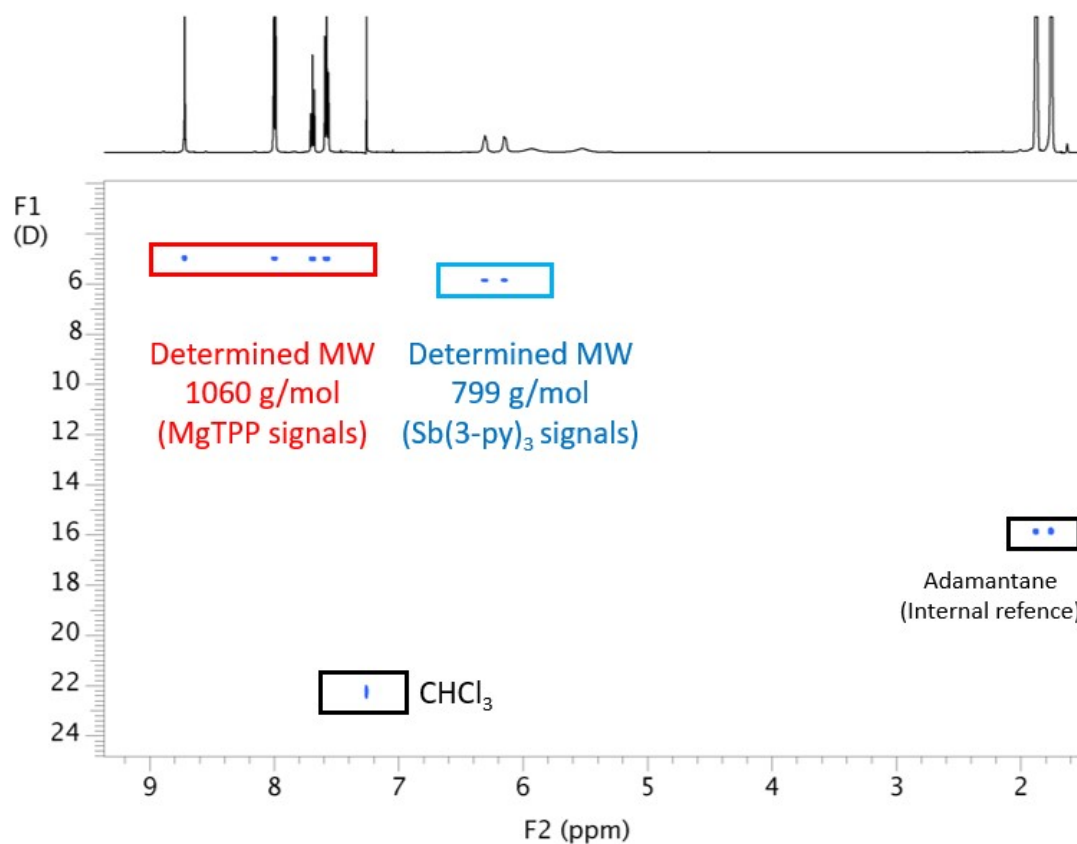


Figure S43. ¹H DOSY NMR spectrum of 1·Mg and adamantane (internal reference) at 298 K in CDCl₃. The diffusion coefficients (D) corresponding to the Sb(3-py)₃ and MgTPP signals are highlighted in blue and red, respectively.

Compound	D m ² /s	$\log D$	$\log D_{x,\text{norm}}$	MW (g/mol)
Adamantane	1.582E-09	-8.8009	-	136.23 ^a
MgTPP	4.944E-10	-9.3059	-9.3205	1060 ^b
Sb(3-py) ₃	5.810E-10	-9.2358	-9.2504	799 ^b

Table S2. D -MW analysis using the ¹H DOSY NMR data obtained for the mixture of 1·Mg and adamantane (internal reference) at 298 K in CDCl₃. ^aReal MW. ^bMW_{det}.

Aggregate	MW _{det} (MgTPP signals)	MW _{det} (Ligand signals)	MW _{cal} (theoretical)	MW _{diff} [%]
Sb(3-py) ₃	-	799	265	-68
MgTPP	1060	-	637	-40
[Sb(3-py) ₃ ·MgTPP]	1060	799	993	-6 and 24
{[Sb(3-py) ₃] ₂ ·MgTPP}	1060	799	1168	9 and 40
[Sb(3-py) ₃ ·(MgTPP) ₂]	1060	799	1539	43 and 84

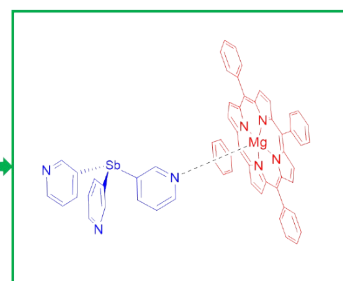


Figure S44. $ECC_{DSE}^{CDCl_3}$ was used to determine the MW_{det} of 1·Mg in CDCl₃ at 298 K and the MW_{Diff} for the proposed species.

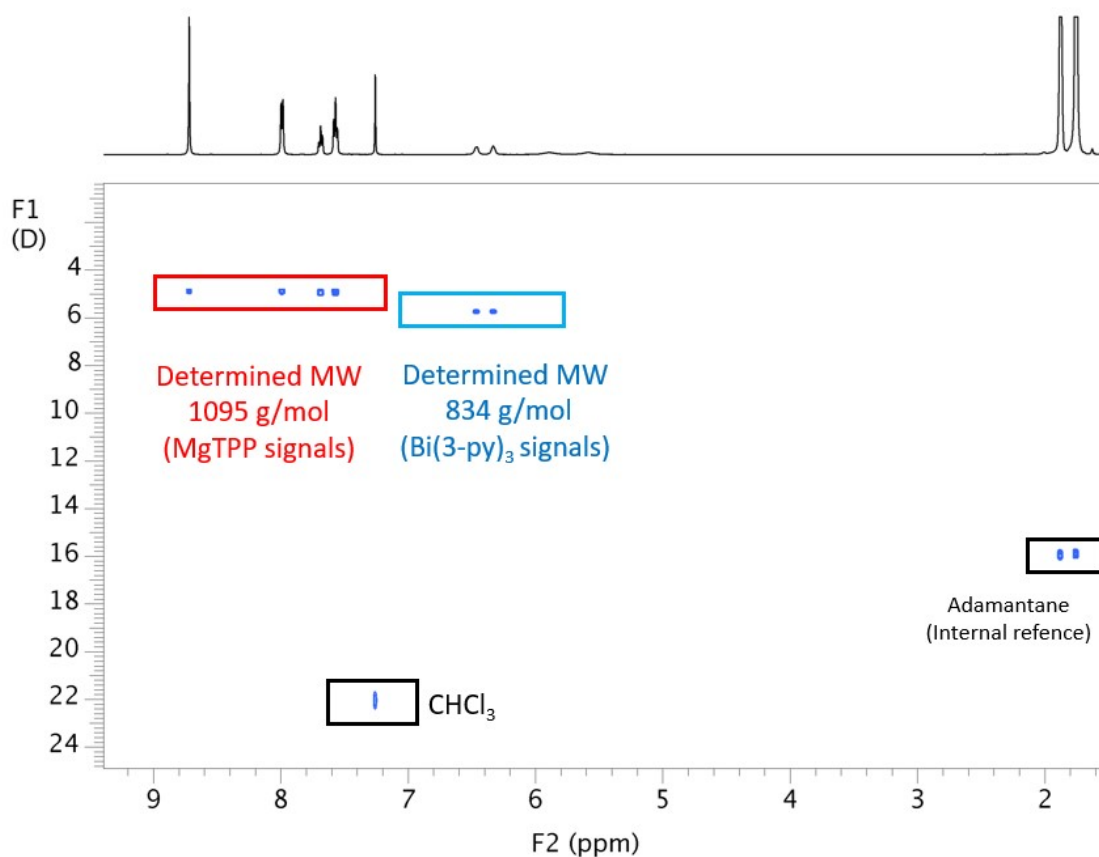


Figure S45. ¹H DOSY NMR spectrum of 2·Mg and adamantane (internal reference) at 298 K in CDCl₃. The diffusion coefficients (D) corresponding to the Sb(3-py)₃ and MgTPP signals are highlighted in blue and red, respectively.

Compound	D m ² /s	log D	log D _{x, norm}	MW (g/mol)
Adamantane	1.588E-09	-8.7992	-	136.23 ^a
MgTPP	4.873E-10	-9.3122	-9.3285	1095 ^b
Bi(3-py) ₃	5.691E-10	-9.2447	-9.2610	834 ^b

Table S3. D-MW analysis using the ¹H DOSY NMR data obtained for the mixture of 2·Mg and adamantane (internal reference) at 298 K in CDCl₃. ^aReal MW. ^bMW_{det}.

Aggregate	MW _{det} (MgTPP signals)	MW _{det} (Ligand signals)	MW _{cal} (theoretical)	MW _{Diff} [%]
Bi(3-py) ₃	-	834	443	-43
MgTPP	1095	-	637	-42
[Bi(3-py) ₃ ·MgTPP]	1095	834	1080	-1 and 30
{[Bi(3-py) ₃] ₂ ·MgTPP}	1095	834	1315	20 and 58
[Bi(3-py) ₃ ·(MgTPP) ₂]	1095	834	1734	58 and 108

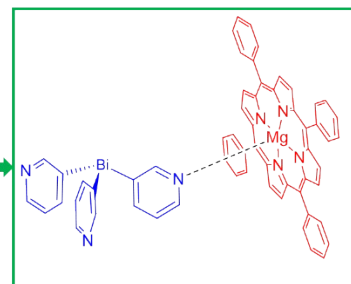


Figure S46. $ECC_{DSE}^{CDCl_3}$ was used to determine the MW_{det} of 2·Mg in CDCl₃ at 298 K and the MW_{Diff} for the proposed species.

Binding data analysis

The NMR titration data were fitted using Dynafit^[12] to perform non-linear least-squares regression of the host–guest binding data. The reaction mechanism in the script file follows the step-wise mechanism:



It is important to remember that the equilibrium constant always refers to the reaction proceeding from left to right. K_1 , K_2 and K_3 are the association equilibrium constants, with the dimension M^{-1} . The association equilibrium constants and mass balance equations are as follows:

$$K_1 = \frac{[\text{H.G}]}{[\text{H}][\text{G}]}$$

$$K_2 = \frac{[\text{H.G.G}]}{[\text{H.G}][\text{G}]}$$

$$K_3 = \frac{[\text{H.G.G.G}]}{[\text{H.G.G}][\text{G}]}$$

$$[\text{H}]_0 = [\text{H}] + [\text{H.G}] + [\text{H.G.G}] + [\text{H.G.G.G}]$$

$$[\text{G}]_0 = [\text{G}] + [\text{H.G}] + 2[\text{H.G.G}] + 3[\text{H.G.G.G}]$$

To stabilize the fitting results, the following physically reasonable constraints were applied: The chemical shifts of ligands **1** and **2** change monotonously as the number of ZnTPP molecules in the assemblies increases. Thus, we assumed a linear dependence of the chemical shifts on the number of guest molecules.

In order to estimate the association constants (K_1 , K_2 and K_3) of compounds **1** and **2** (hosts) with ZnTPP (guest), the dilution method was applied. A 10^{-3} M solution of each compound in CDCl_3 was prepared, and a known volume was transferred to an NMR tube (500 μL). The titration was carried out by adding known portions of a stock solution of ZnTPP (10^{-2} M) in CDCl_3 to cover a wide range of equivalents. The progress of the titration was monitored by the chemical shifts of the peaks of H_4 and H_5 of the ligands **1** and **2**.

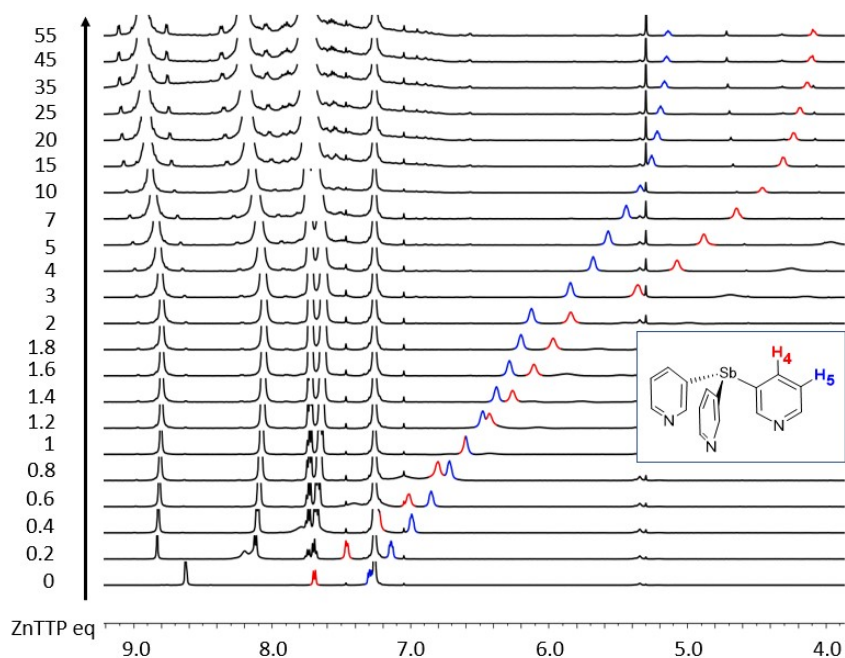
Titration study of $\text{Sb}(\text{3-py})_3$ with ZnTPP

Figure S47. Stacked $^1\text{H-NMR}$ spectra of the titration of ligand **1** with up to 55 equivalents of ZnTPP. The signals of the ligands that were followed are highlighted in red (H_4) and blue (H_5), respectively.

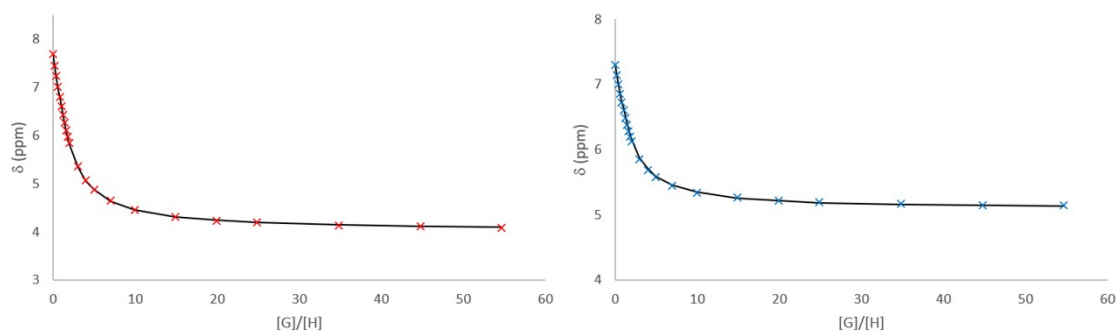


Figure S48. Experimental values of chemical shifts of the $\text{Sb}(\text{3-py})_3$ signals (H_4 in red and H_5 in blue) against $[\text{G}]/[\text{H}]$, and theoretical values obtained from the non-linear regression to a 1:3 binding isotherm (black lines).

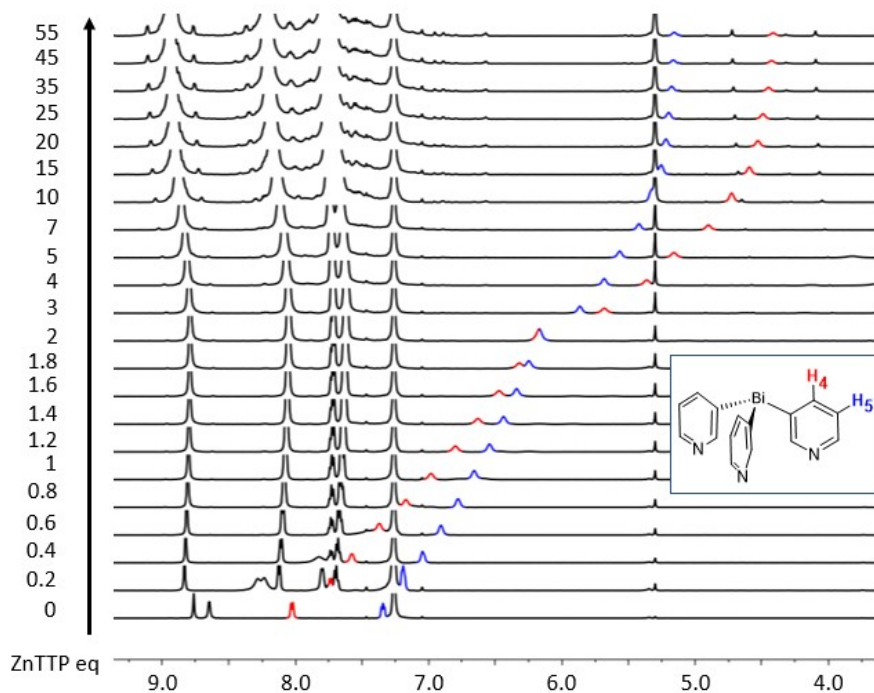
Titration study of $\text{Bi}(3\text{-py})_3$ with ZnTPP

Figure S49. Stacked ^1H -NMR spectra of the titration of ligand **2** with up to 55 equivalents of ZnTPP. The signals of the ligands that were followed are highlighted in red (H_4) and blue (H_5), respectively.

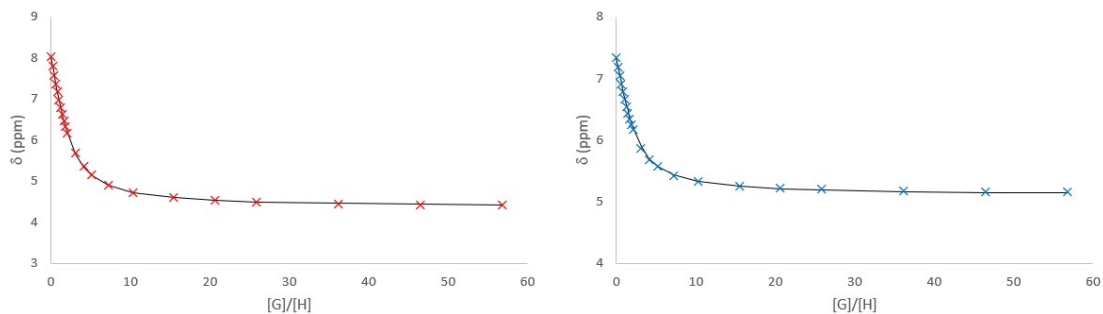


Figure S50. Experimental values of the chemical shifts of the $\text{Bi}(3\text{-py})_3$ signals (H_4 in red and H_5 in blue) against $[\text{G}]/[\text{H}]$, and theoretical values obtained from the non-linear regression to a 1:3 binding isotherm (black lines).

High resolution mass data

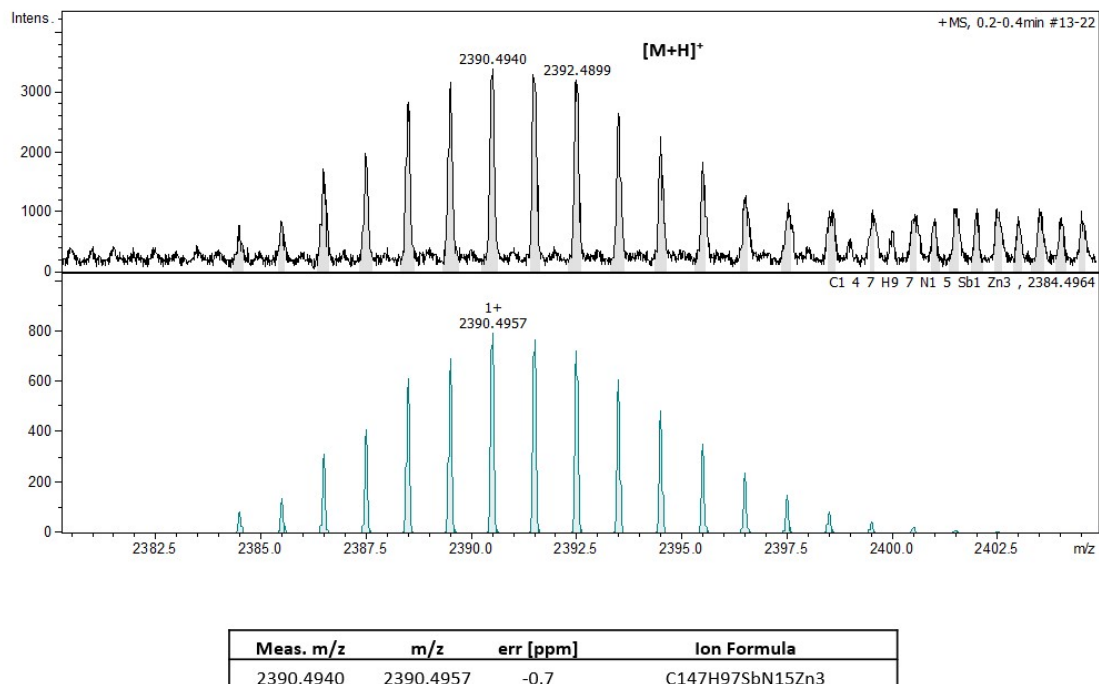


Figure S51. HR-MS (ESI-TOF) (positive mode) of $\{[Sb(3-py)_3] \cdot (ZnTPP)_3\} (1 \cdot Zn)$ showing the expected $[M+H]^+$ peak at m/z 2390.4940 (calcd 2390.4957; -0.7 ppm error) (top) and simulation (bottom).

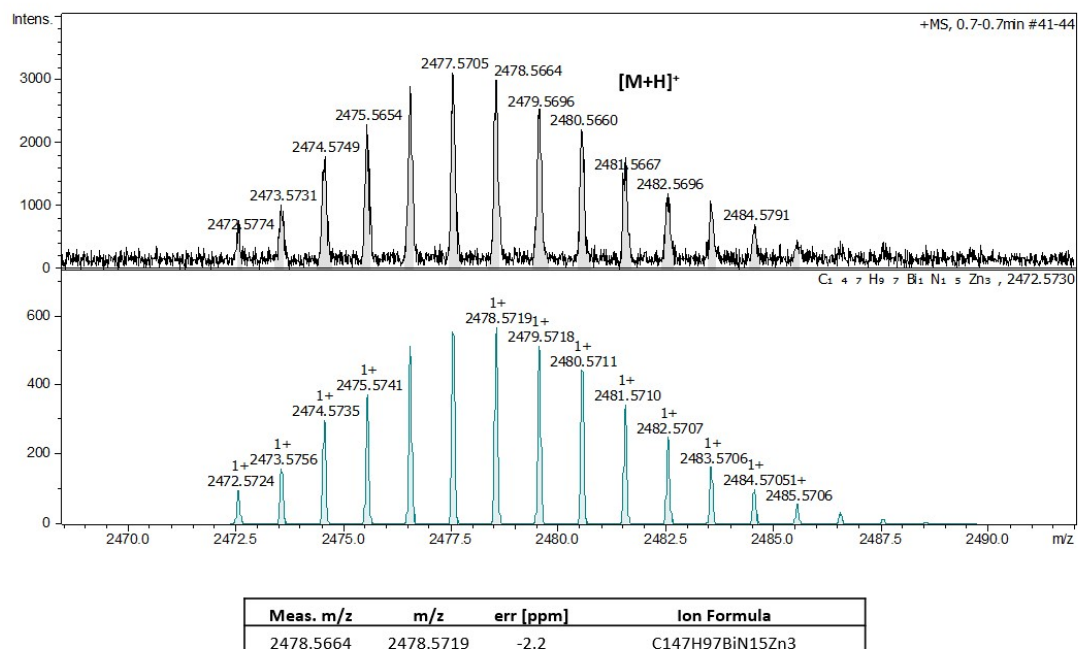


Figure S52. HR-MS (ESI-TOF) (positive mode) of $\{[Bi(3-py)_3] \cdot (ZnTPP)_3\} (2 \cdot Zn)$ showing the expected $[M+H]^+$ peak at m/z 2478.5664 (calcd 2478.5719; -2.2 ppm error) (top) and the simulated data (bottom).

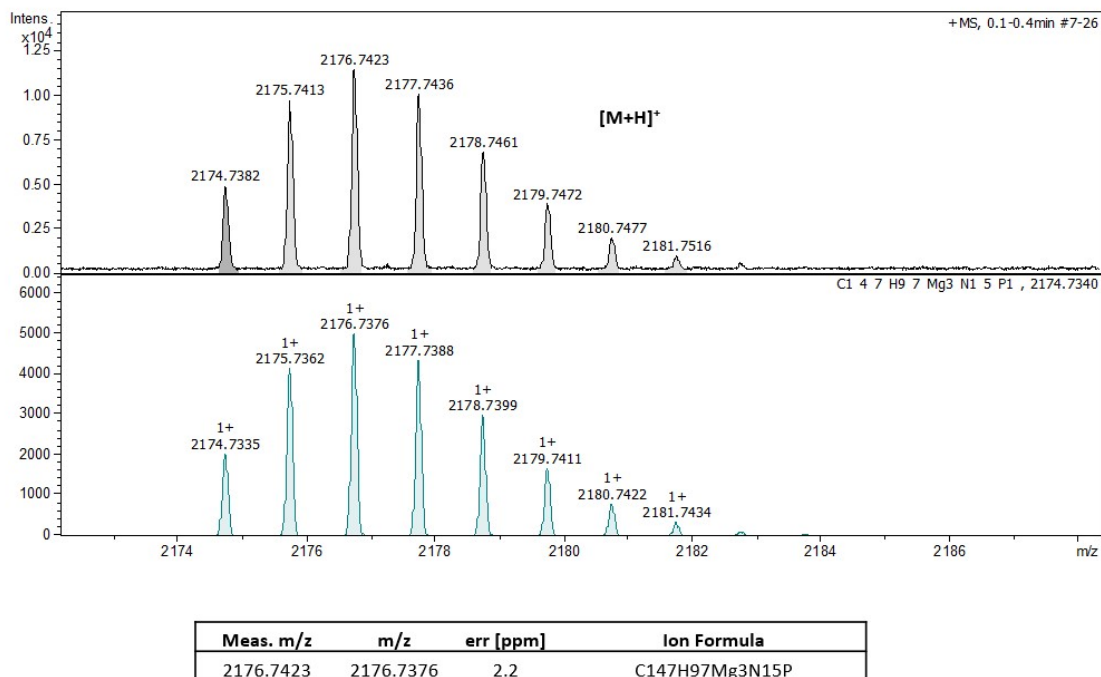


Figure S53. HR-MS (ESI-TOF) (positive mode) of $\{[P(3\text{-py})_3] \cdot (MgTPP)_3\}$ showing the expected $[M+H]^+$ peak at m/z 2176.7423 (calcd 2176.7376; 2.2 ppm error) (top) and simulated data (bottom).

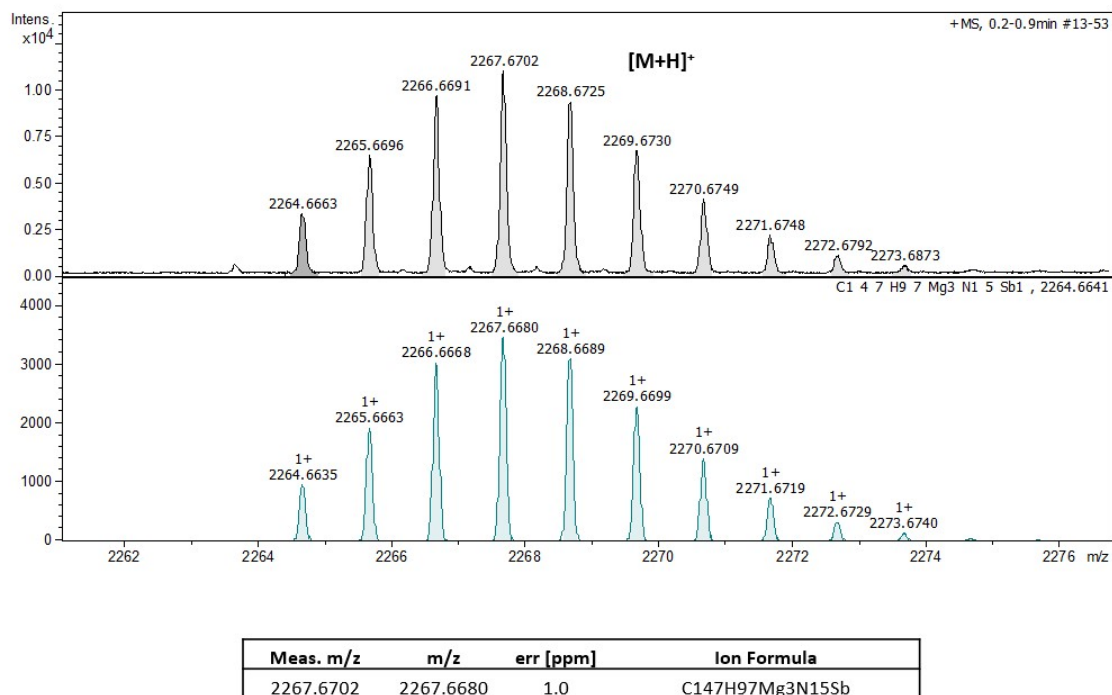


Figure S54. HR-MS (ESI-TOF) (positive mode) of $\{[Sb(3\text{-py})_3] \cdot (MgTPP)_3\}$ showing the expected $[M+H]^+$ peak at m/z 2267.6702 (calcd 2267.6680; 1.0 ppm error) (top) and simulated data (bottom).

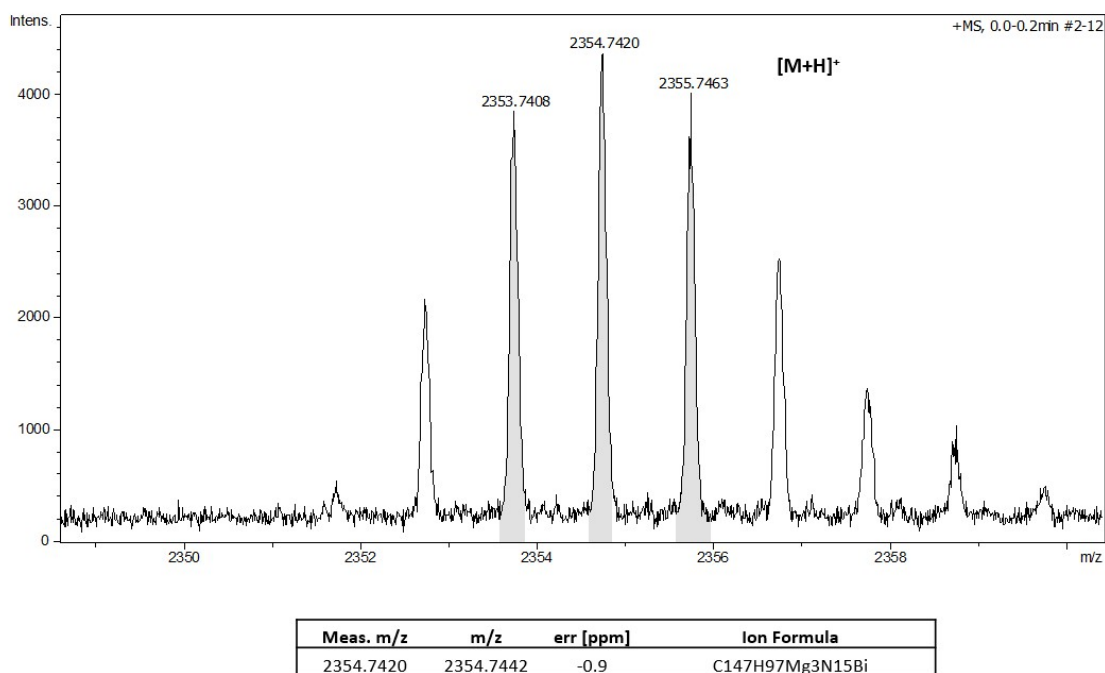


Figure S55. HR-MS (ESI-TOF) (positive mode) of $\{[Bi(3-py)_3] \cdot (MgTPP)_3\}$ showing the expected $[M+H]^+$ peak at m/z 2354.7420 (calcd 2354.7442; -0.9 ppm error).

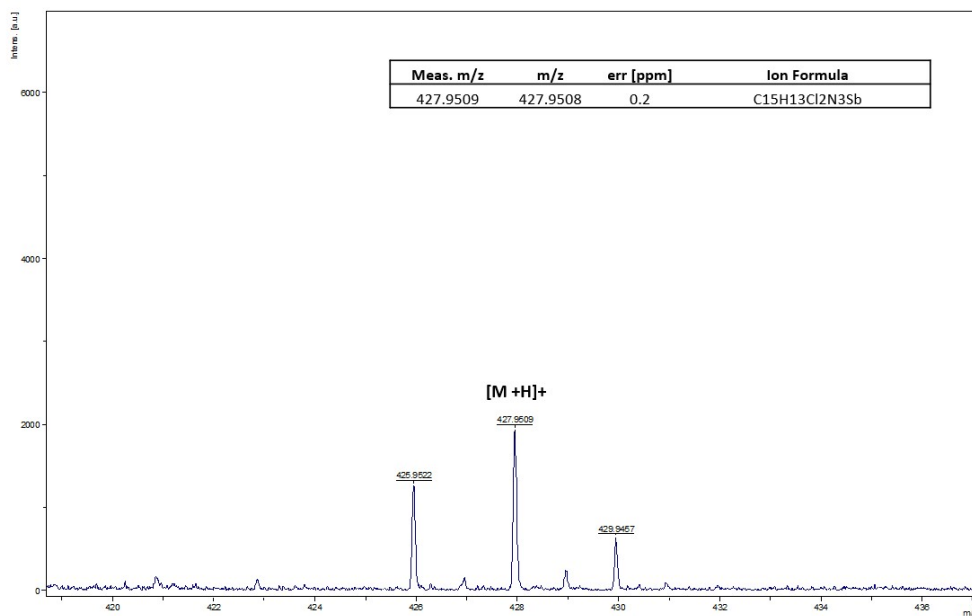


Figure S56. HR-MS (MALDI-TOF) (positive mode) of **3** showing the $[M+H]^+$ peak at m/z 427.9509 (calcd 427.9508; 0.2 ppm error).

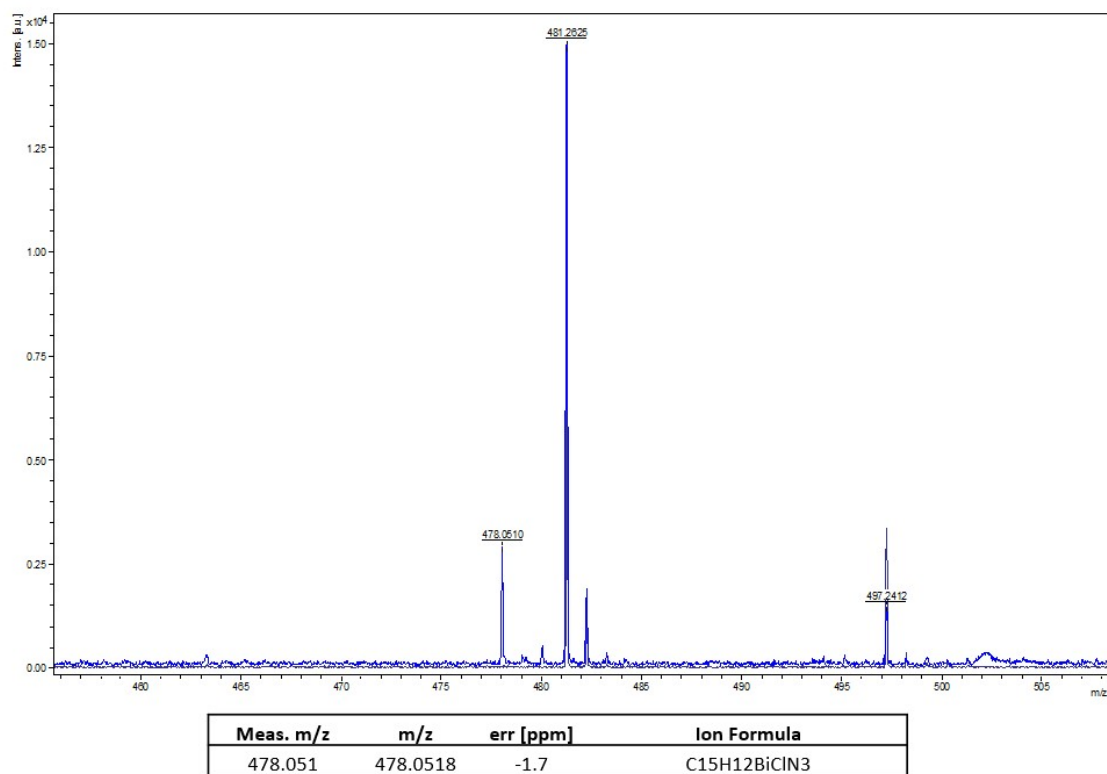


Figure S57. HR-MS (ESI-TOF) (positive mode) of **4** showing the expected $[M-Cl]^+$ peak at m/z 478.0510 (calcd 478.0518; -1.7 ppm error).

X-ray crystallographic studies

Details of the data collections and structural refinements are given in Table S4. Further details of the methods of refinement of the structures are as follows.

The refinement was straightforward for compounds **4** and **3·Py**.

In the rest of the structures, the capsules are well-ordered, but there are additional voids in the lattice with solvents that were not always clearly resolved. The refinement details are given below.

1 α Zn-closed

Four CHCl₃ molecules could be found in the asymmetric unit. Two were relatively ordered, while the other two (which were located outside the capsule) were very poorly resolved and could not be modelled satisfactorily. Additional void space exists, with clear peaks in electron density but no clearly resolvable solvent molecules. Omitting the two poorly resolved molecules of CHCl₃ and applying the Olex2 solvent mask yielded R1 = 5.89% and WR2 = 17.05%. In the calculated solvent mask, 449 electrons were found in a volume of 1379 cubic angstroms in two voids per unit cell. The crystallization solvent was CHCl₃/hexane, and this is consistent with the presence of roughly 8 CHCl₃ per unit cell (i.e., 4 CHCl₃ per formula unit), which account for 464 electrons per unit cell. The crystals were observed to lose solvent very quickly during the preparation of the sample, and therefore the exact amount of CHCl₃ is expected to vary among crystals due to partial loss of CHCl₃.

2 α Zn-closed

Three well-defined molecules of CHCl₃ were located in the asymmetric unit, along with two very poorly defined CHCl₃ molecules (located outside the capsule) that could not be satisfactorily modelled. Moreover, additional void space exists, with clear peaks in the residual electron density but no clearly identifiable solvent molecules. Therefore, the model presented here involves the removal of the two poorly defined CHCl₃ molecules and the use of the Olex2 solvent mask. 435 electrons were found in a volume of 1176 cubic angstroms in one void per unit cell. The crystallization solvent was CHCl₃/hexane, and this is consistent with roughly 8 CHCl₃ per unit cell (i.e., 4 CHCl₃ per formula unit), which account for 464 electrons per unit cell. The crystals were observed to lose solvent very quickly during the preparation of the sample, and therefore the exact amount of CHCl₃ is expected to vary among crystals due to the partial loss of CHCl₃.

1 α Zn-open

The molecular capsule was clearly resolved, but very poorly defined solvent molecules were present in the unit cell. Among them, a relatively well-defined molecule of CHCl₃ and a very poorly defined molecule of hexane were identified outside the molecular capsule. The hexane was treated as a rigid body, leading to a suboptimal refinement. In addition to this, several clear peaks in the residual electron density in solvent-accessible voids were present, but there were no clearly identifiable solvent molecules. The poorly

refined molecule of hexane was thus removed and the olex2 solvent mask was applied. In the calculated solvent mask, 259 electrons were found in a volume of 1016 cubic angstroms in two voids per unit cell, with poorly defined molecules of solvent. The crystallization solvent was CHCl_3 /hexane, and NMR spectroscopy indicated the presence of both CHCl_3 and hexane in the bulk crystalline sample. Although this could be consistent with the presence of roughly three molecules of hexane and two molecules of CHCl_3 in the unit cell (accounting for 266 electrons per unit cell), the exact proportion of the solvents in the crystal is difficult to determine due to their similar electron count. Moreover, the crystals were observed to lose solvent very quickly during the preparation of the sample, and therefore the exact amount of hexane or CHCl_3 is expected to vary among crystals due to their partial loss.

2 α Zn-open

A relatively poorly defined molecule of hexane was present in the lattice. Restraints were used to maintain sensible bond distances and geometry, and this molecule was treated as a rigid body in the final refinement cycles. Further solvent was present in the asymmetric unit, as evidenced by the presence of clear peaks in the residual electron density in solvent-accessible voids with no clearly identifiable solvent molecules; thus, the Olex2 solvent mask was used. 167 electrons were found in a volume of 760 cubic angstroms in two voids per unit cell. The crystallization solvent was CHCl_3 /hexane, and NMR spectroscopy indicated the presence of both CHCl_3 and hexane in the bulk crystalline sample. Although this could be consistent with the presence of roughly two molecules of hexane and one molecule of CHCl_3 in the unit cell (accounting for 158 electrons per unit cell), the exact proportion of the solvents in the crystal is difficult to determine due to their similar electron count. Moreover, the crystals were observed to lose solvent very quickly during the preparation of the sample, and therefore, the exact amount of hexane or CHCl_3 is expected to vary among crystals due to their partial loss. The alternative approach of removing the molecule of hexane and applying the olex2 solvent mask (i.e., leaving only the molecular capsule with no solvent molecules) produces $R1 = 5.66\%$ and $WR2 = 10.61\%$. Although this solution is not provided, it is indicative of the level that the R-factors may be expected to reach.

3 α Zn

In addition to three well-defined molecules of CHCl_3 , further void spaces with clear residual electron density peaks were present, which probably contain further molecules of CHCl_3 . This was treated using the Olex2 solvent mask. 121 electrons were found in a volume of 401 cubic angstroms in one void per unit cell. The crystallization solvent was CHCl_3 /hexane, and this is consistent with the presence of roughly 2 CHCl_3 per unit cell, which account for 116 electrons per unit cell.

3 α Mg

There are clear residual electron density peaks in void spaces corresponding to poorly defined molecules of solvent. A solvent mask was calculated, and 206 electrons were found in a volume of 685 cubic angstroms in one void per unit cell. The crystallization solvent was CHCl_3 /hexane, and this is consistent with the presence of roughly 4 CHCl_3 per unit cell, which account for 232 electrons per unit cell.

2 α Mg

1/3 CHCl₃ was present in the asymmetric unit (corresponding to two molecules per formula unit, i.e., six per unit cell). In addition to this, there was further CHCl₃ that could not be modelled, which was handled by applying the olex2 solvent mask. In the calculated solvent mask, 1114 electrons were found in a volume of 5596 cubic angstroms in one void per unit cell. The crystallization solvent was CHCl₃/hexane, and this is consistent with the presence of roughly 6 CHCl₃ per formula unit (i.e., roughly 1 CHCl₃ per asymmetric unit; 18 CHCl₃ per unit cell), which account for 1044 electrons per unit cell. The crystals were observed to lose solvent very quickly during the preparation of the sample, and therefore the exact amount of CHCl₃ or hexane is expected to vary among crystals due to their partial loss.

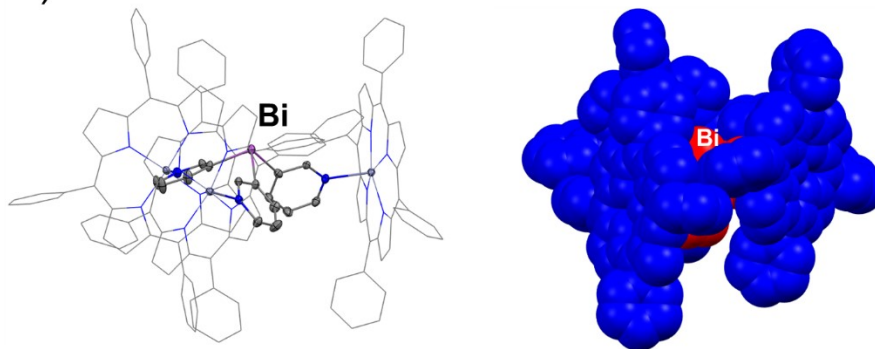
1 α Mg

1/3 CHCl₃ was present in the asymmetric unit, along with further CHCl₃ in the lattice. One CHCl₃ was refined with the occupancy constrained to 0.5 and with restraints to assure a reasonable geometry and ADPs. The rest of the CHCl₃ could not be modelled satisfactorily and was handled using the olex2 solvent mask. In the calculated solvent mask, 537 electrons were found in a volume of 3105 cubic angstroms in two voids per unit cell. This is consistent with roughly 3 CHCl₃ molecules per formula unit, which account for 522 electrons (9 CHCl₃ molecules per unit cell). The crystals were observed to lose solvent very quickly during the preparation of the sample, and therefore the exact amount of CHCl₃ or hexane is expected to vary among crystals due to their partial loss.

P α Mg

Despite our best efforts, the solvent present in the lattice could not be modelled satisfactorily and was handled using the olex2 solvent mask. 1214 electrons were found in a volume of 6206 cubic angstroms in two voids per unit cell. The crystallization solvent was CHCl₃/hexane, and this is consistent with the presence of roughly 7 CHCl₃ per formula unit (i.e., roughly 21 CHCl₃ per unit cell) which account for 1218 electrons per unit cell. The crystals were observed to lose solvent very quickly during the preparation of the sample, and therefore the exact amount of CHCl₃ and therefore the exact amount of CHCl₃ or hexane is expected to vary among crystals due to their partial loss.

a) 2·Zn-closed



b) 2·Zn-open

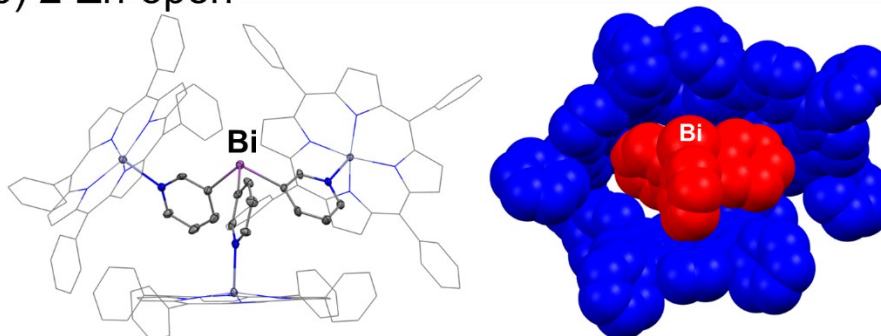


Figure S58. Solid-state structures of closed-capsule conformers of 2·Zn (a, left) and open-capsule conformer for 2·Zn (b, left). Space filling views of the X-ray structures (a, b, right); ligand 2 is indicated in red, and the three ZnTPP moieties in blue. Colour key: C (grey), Zn (dark grey), N (blue) and Bi (purple).

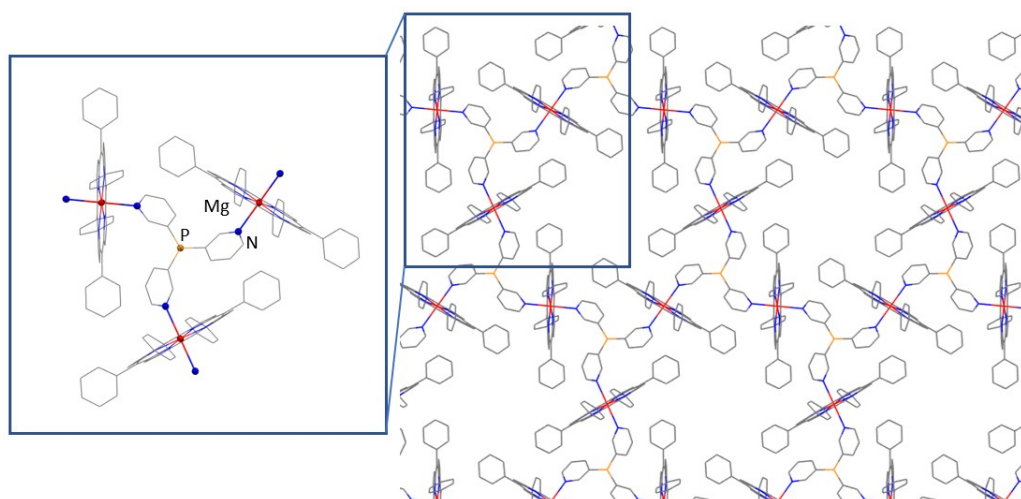


Figure S59. X-ray structure of the 2D polymeric structure of P·Mg formed through N---Mg interactions with the highlighted {[P(3-py)₃]·(MgTPP)₃} unit. Displacement ellipsoids at 50% probability. H atoms are omitted for clarity. Colour key: C (grey), N (blue), P (orange) and Mg (red).

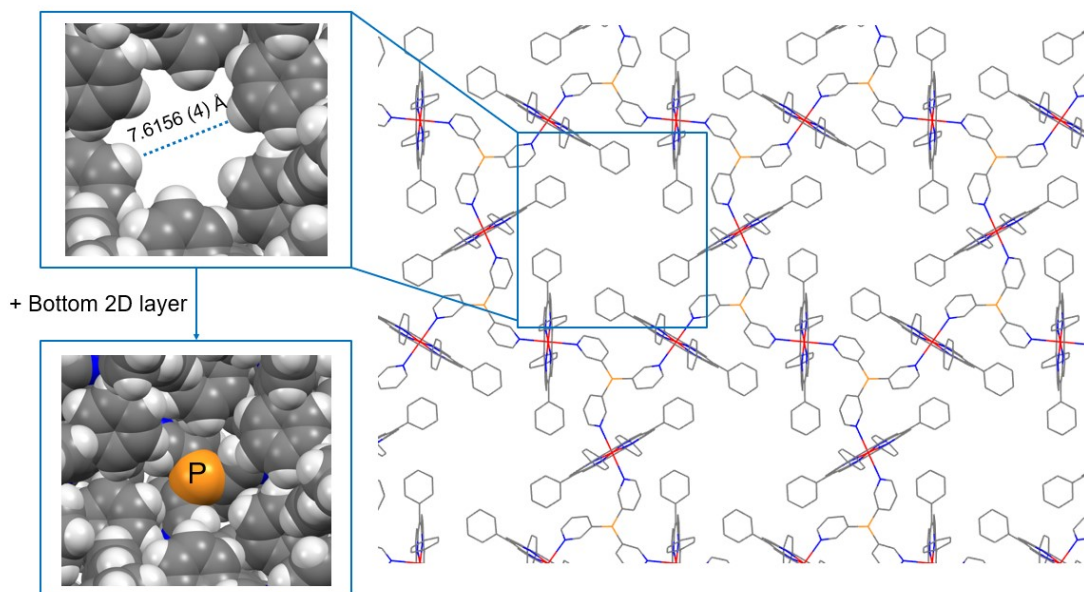


Figure S60. X-ray structure of the 2D polymeric structure of **P**·Mg formed through N---Mg interactions with the highlighted hexagonal window. Displacement ellipsoids at 50% probability. H atoms are omitted for clarity. Colour key: C (grey), N (blue), P (orange) and Mg (red).

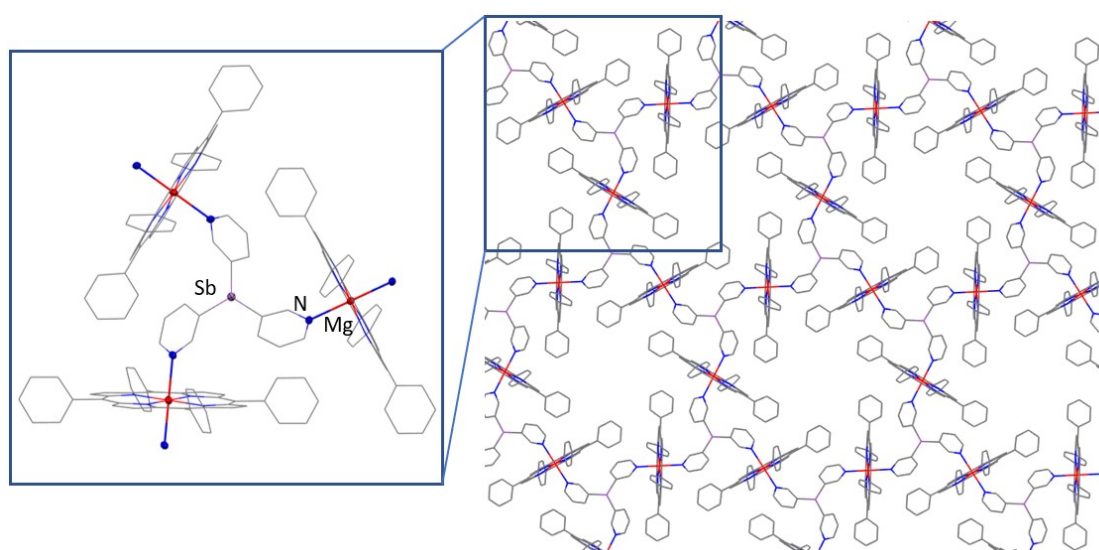


Figure S61. X-ray structure of the 2D polymeric structure of **1**·Mg formed through N---Mg interactions with the highlighted $\{[\text{Sb}(\text{3-py})_3] \cdot (\text{MgTPP})_3\}$ unit. Displacement ellipsoids at 50% probability. H atoms are omitted for clarity. Colour key: C (grey), N (blue), Sb (light purple) and Mg (red).

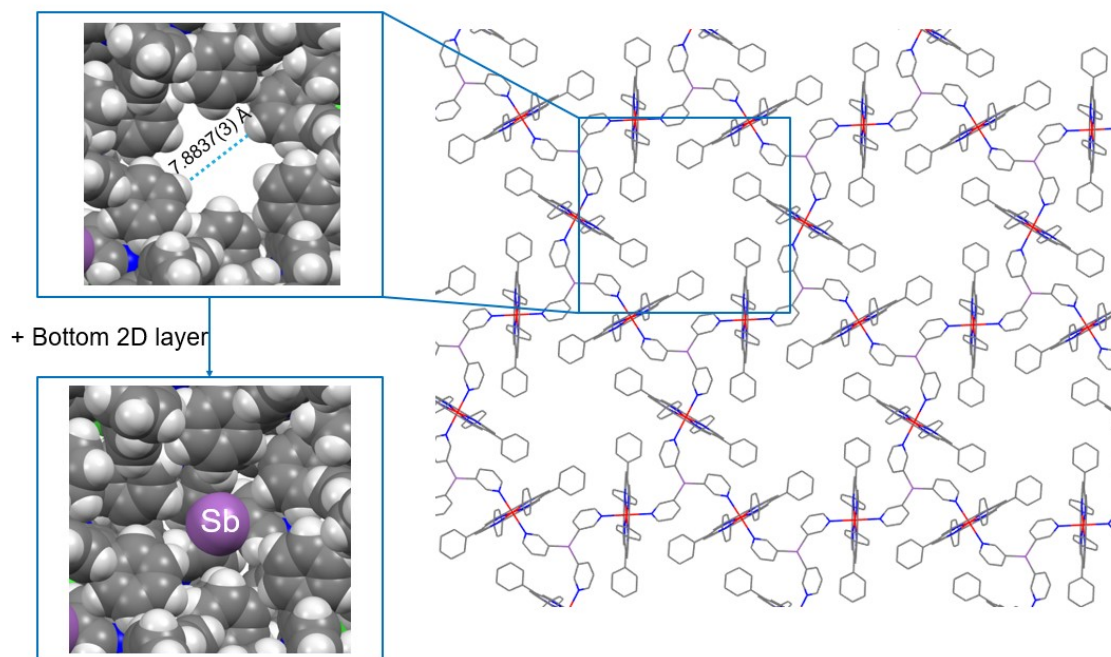


Figure S62. X-ray structure of the 2D polymeric structure of **1**·Mg formed through N---Mg interactions with the highlighted hexagonal window. Displacement ellipsoids at 50% probability. H atoms are omitted for clarity. Colour key: C (grey), N (blue), Sb (light purple) and Mg (red).

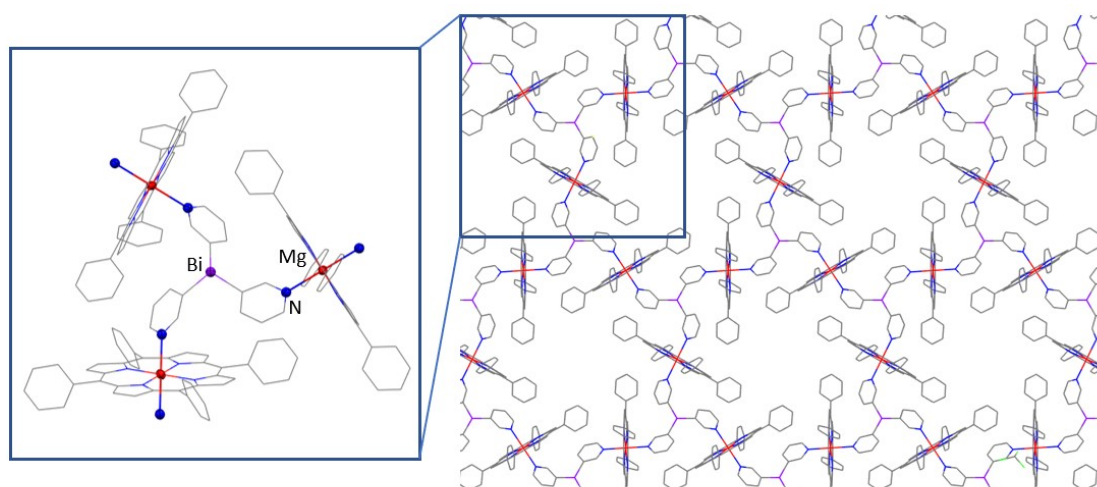


Figure S63. X-ray structure of the 2D polymeric structure of **2**·Mg formed through N---Mg interactions with the highlighted $\{[\text{Bi}(3\text{-py})_3] \cdot (\text{MgTPP})_3\}$ unit. Displacement ellipsoids at 50% probability. H atoms are omitted for clarity. Colour key: C (grey), N (blue), Bi (purple) and Mg (red).

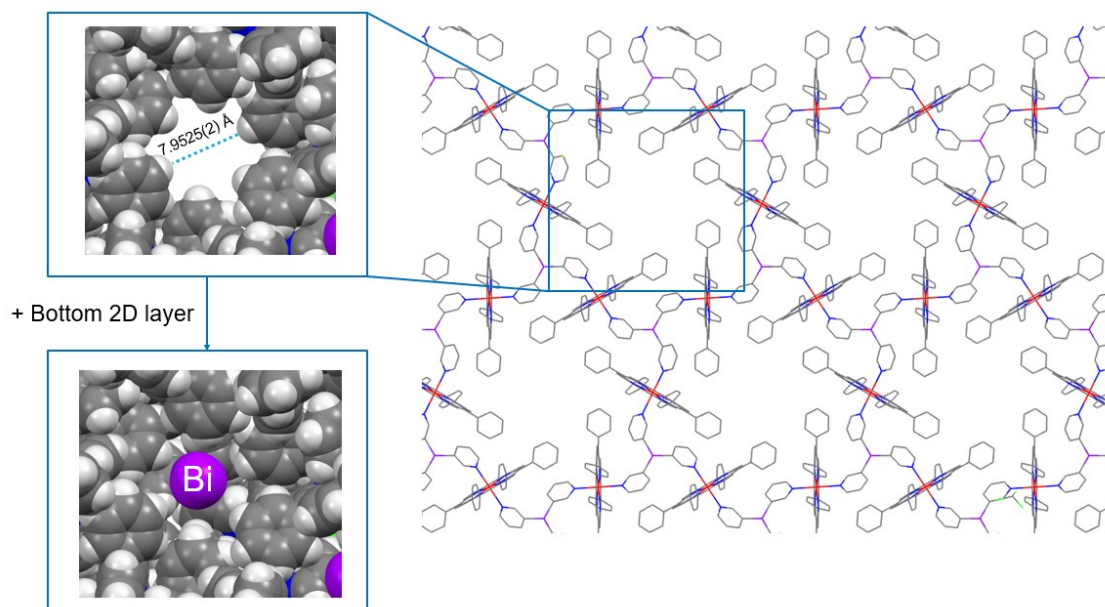


Figure S64. X-ray structure of the 2D polymeric structure of **2·Mg** formed through N---Mg interactions with the highlighted hexagonal window. Displacement ellipsoids at 50% probability. H atoms are omitted for clarity. Colour key: C (grey), N (blue), Bi (purple) and Mg (red).

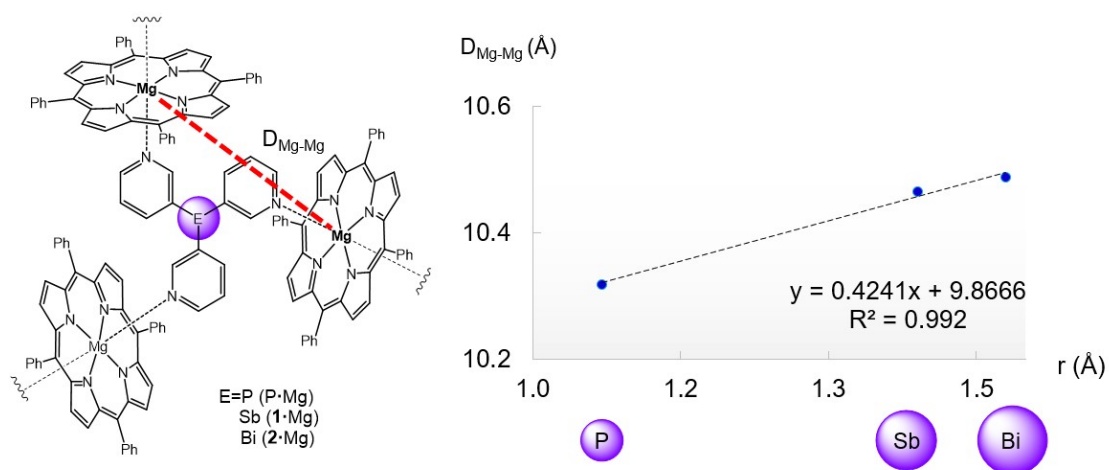


Figure S65. Correlation between the covalent radii of the bridgehead atom and the effective size of the capsule in the X-ray structures of $\{[P(3-py)_3] \cdot (MgTPP)_3\}$, **1·Mg** and **2·Mg**.

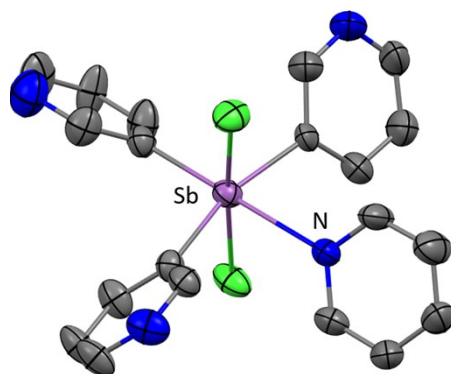


Figure S66. Molecular structure of $\text{Cl}_2\text{Sb}(\text{3N-py})_3\cdot\text{Py}$ (**3·py**). Displacement ellipsoids at 50% probability. H atoms are omitted for clarity. Selected bond lengths (Å) and angles (deg): Sb–C_{py} 2.14(1)–2.146(8); Sb–Cl 2.449(2)–2.465(2); Sb–N 2.441(7); C_{py}–Sb–C_{py} 97.3(3)–97.4(3); C_{py}–Sb–N 82.0(3)–83.3(3). Colour key: C (grey), Cl (green), N (blue) and Sb (light purple).

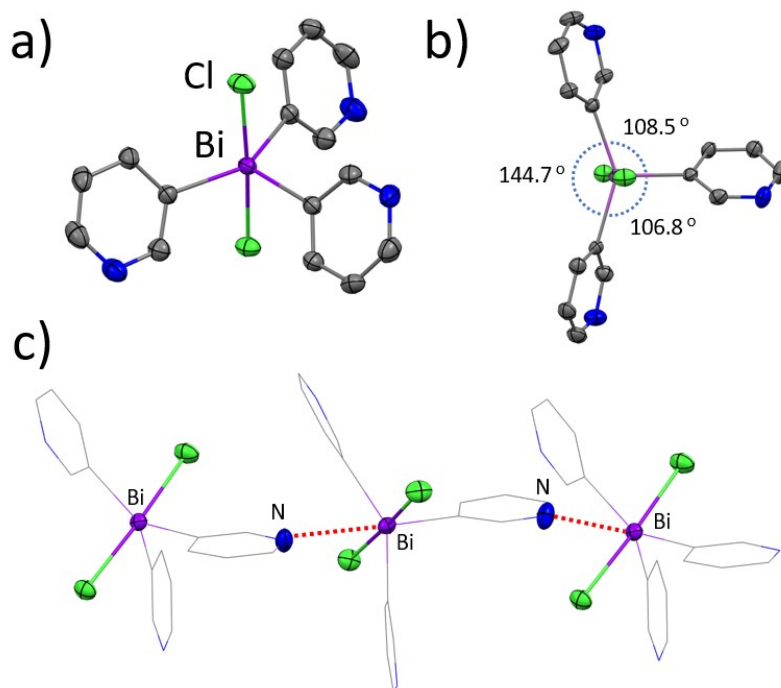


Figure S67. (a) Molecular structure of the monomeric unit of $\text{Cl}_2\text{Bi}(\text{3N-py})_3$ (**4**). (b) Values of the three C–Bi–C angles for the X-ray structure of **4**. (c) Formation of the 1D polymeric structure through Bi–N interactions between the monomeric units. Displacement ellipsoids at 50% probability. H atoms are omitted for clarity. Selected bond lengths (Å) and angles (deg): Bi–C_{py} 2.215(8)–2.228(8); Bi–Cl 2.572(2)–2.595(2); C_{py}–Bi–C_{py} 106.8(2)–144.7(2). Colour key: C (grey), Cl (green), N (blue) and Bi (purple).

Table S4. Crystallographic data

Identification code	1·Zn-closed	2·Zn-closed	1·Zn-open
CCDC Number	2195695	2195698	2195696
Empirical formula	$C_{149}H_{98}Cl_6N_{15}SbZn_3$	$C_{150}H_{98}BiCl_9N_{15}Zn_3$	$C_{148}H_{97}Cl_3N_{15}SbZn_3$
Formula weight	2628.98	2834.57	2509.61
Temperature/K	180(2)	180(2)	180(2)
Crystal system	triclinic	triclinic	triclinic
Space group	P-1	P-1	P-1
a/Å	13.4042(3)	13.3955(3)	11.5963(3)
b/Å	21.6415(7)	21.5477(7)	21.0912(5)
c/Å	24.8568(8)	25.0484(8)	28.0154(6)
$\alpha/^\circ$	92.283(3)	92.054(3)	86.6057(18)
$\beta/^\circ$	99.219(2)	98.955(2)	79.266(2)
$\gamma/^\circ$	94.883(2)	94.962(2)	77.064(2)
Volume/Å ³	7081.2(4)	7106.2(4)	6560.1(3)
Z	2	2	2
$\rho_{\text{calc}}/\text{g/cm}^3$	1.233	1.325	1.27
μ/mm^{-1}	0.857	1.958	0.862
F(000)	2680	2858	2564
Crystal size/mm ³	0.41 × 0.30 × 0.10	0.44 × 0.11 × 0.04	0.59 × 0.28 × 0.20
Radiation	MoK α	MoK α	MoK α
2 θ range for data collection/ $^\circ$	3.092 to 50.094	4.85 to 50.082	4.346 to 50.116
Index ranges	-15 ≤ h ≤ 15, -25 ≤ k ≤ 25, -19 ≤ l ≤ 29	-15 ≤ h ≤ 15, -19 ≤ k ≤ 25, -29 ≤ l ≤ 29	-9 ≤ h ≤ 13, -25 ≤ k ≤ 24, -33 ≤ l ≤ 33
Reflections collected	57165	56986	43227
Independent reflections	25014 [R _{int} = 0.0416, R _{sigma} = 0.0672]	25082 [R _{int} = 0.0498, R _{sigma} = 0.0882]	23158 [R _{int} = 0.0295, R _{sigma} = 0.0579]
Data/restraints/parameters	25014/0/1567	25082/0/1603	23158/0/1531
Goodness-of-fit on F ²	1.033	1.058	1.023
Final R indexes [I ≥ 2 σ (I)]	R ₁ = 0.0589, wR ₂ = 0.1506	R ₁ = 0.0566, wR ₂ = 0.1448	R ₁ = 0.0530, wR ₂ = 0.1297
Final R indexes [all data]	R ₁ = 0.0864, wR ₂ = 0.1705	R ₁ = 0.0910, wR ₂ = 0.1588	R ₁ = 0.0704, wR ₂ = 0.1409
Max/min $\Delta\rho$ [eÅ ⁻³]	1.93/-1.57	1.65/-1.50	1.60/-1.09

Identification code	2·Zn-open	P·Mg	1·Mg
CCDC Number	2195699	2195704	2195694
Empirical formula	$C_{153}H_{110}BiN_{15}Zn_3$	$C_{162}H_{108}Mg_3N_{18}P_2$	$C_{167}H_{113}Cl_{15}Mg_3N_{18}Sb_2$
Formula weight	2563.64	2441.53	3219.93
Temperature/K	180(2)	220(2)	220(2)
Crystal system	triclinic	trigonal	trigonal
Space group	P-1	R-3	R-3
a/Å	11.5622(5)	20.6368(12)	20.9301(8)
b/Å	21.0461(8)	20.6368(12)	20.9301(8)
c/Å	27.9789(9)	37.744(2)	37.6852(17)
$\alpha/^\circ$	86.862(3)	90	90
$\beta/^\circ$	79.147(3)	90	90
$\gamma/^\circ$	76.921(3)	120	120
Volume/Å ³	6512.6(4)	13920.8(18)	14297.0(13)
Z	2	3	3
$\rho_{\text{calc}}/\text{cm}^3$	1.307	0.874	1.122
μ/mm^{-1}	1.95	0.078	0.551
F(000)	2612	3816	4902
Crystal size/mm ³	0.55 × 0.11 × 0.05	0.46 × 0.35 × 0.13	0.37 × 0.30 × 0.13
Radiation	MoK α	MoK α	MoK α
2 θ range for data collection/ $^\circ$	3.678 to 50.052	3.138 to 49.456	5.854 to 49.44
Index ranges	-13 ≤ h ≤ 13, -20 ≤ k ≤ 25, -33 ≤ l ≤ 33	-20 ≤ h ≤ 24, -24 ≤ k ≤ 10, -38 ≤ l ≤ 44	-12 ≤ h ≤ 24, -22 ≤ k ≤ 18, -38 ≤ l ≤ 44
Reflections collected	43773	10431	10644
Independent reflections	22999 [R _{int} = 0.0885, R _{sigma} = 0.1619]	5282 [R _{int} = 0.0522, R _{sigma} = 0.1022]	5421 [R _{int} = 0.0464, R _{sigma} = 0.0952]
Data/restraints/parameters	22999/27/1538	5282/0/280	5421/39/328
Goodness-of-fit on F ²	0.934	0.948	0.975
Final R indexes [I ≥ 2 σ (I)]	R ₁ = 0.0598, wR ₂ = 0.1096	R ₁ = 0.0684, wR ₂ = 0.1786	R ₁ = 0.0583, wR ₂ = 0.1567
Final R indexes [all data]	R ₁ = 0.1171, wR ₂ = 0.1290	R ₁ = 0.1173, wR ₂ = 0.2074	R ₁ = 0.0968, wR ₂ = 0.1727
Max/min $\Delta\rho$ [eÅ ⁻³]	1.60/-1.27	0.22/-0.25	0.86/-0.55

Identification code	2·Mg	3·Py	4
CCDC Number	2195697	2195701	2195703
Empirical formula	C ₁₆₄ H ₁₁₀ Bi ₂ Cl ₆ Mg ₃ N ₁₈	C ₂₀ H ₁₇ Cl ₂ N ₄ Sb	C ₁₅ H ₁₂ BiCl ₂ N ₃
Formula weight	3036.28	506.02	514.16
Temperature/K	220(2)	293(2)	293(2)
Crystal system	trigonal	monoclinic	monoclinic
Space group	R-3	Pn	P2 ₁ /c
a/Å	20.9744(6)	9.8444(6)	9.4717(14)
b/Å	20.9744(6)	7.4353(4)	15.5617(7)
c/Å	37.5959(13)	14.6876(8)	14.976(2)
α/°	90	90	90
β/°	90	106.385(6)	134.03(3)
γ/°	120	90	90
Volume/Å ³	14323.5(10)	1031.41(11)	1587.1(6)
Z	3	2	4
ρ _{calc} /cm ³	1.056	1.629	2.152
μ/mm ⁻¹	1.979	1.608	11.441
F(000)	4572	500	960
Crystal size/mm ³	0.37 × 0.23 × 0.19	0.15 × 0.11 × 0.09	0.39 × 0.24 × 0.16
Radiation	MoKα	MoKα	Mo Kα
2θ range for data collection/°	4.614 to 51.394	6.974 to 58.958	6.788 to 59.528
Index ranges	-15 ≤ h ≤ 24, -25 ≤ k ≤ 13, -37 ≤ l ≤ 45	-9 ≤ h ≤ 13, -10 ≤ k ≤ 10, -19 ≤ l ≤ 17	-9 ≤ h ≤ 13, -20 ≤ k ≤ 21, -20 ≤ l ≤ 17
Reflections collected	11221	5224	8305
Independent reflections	6058 [R _{int} = 0.0260, R _{sigma} = 0.0514]	3348 [R _{int} = 0.0326, R _{sigma} = 0.0561]	3779 [R _{int} = 0.0315, R _{sigma} = 0.0484]
Data/restraints/parameters	6058/0/292	3348/2/244	3779/0/190
Goodness-of-fit on F ²	1.006	1.065	1.013
Final R indexes [I ≥ 2σ (I)]	R ₁ = 0.0338, wR ₂ = 0.0799	R ₁ = 0.0376, wR ₂ = 0.0685	R ₁ = 0.0322, wR ₂ = 0.0580
Final R indexes [all data]	R ₁ = 0.0450, wR ₂ = 0.0837	R ₁ = 0.0483, wR ₂ = 0.0773	R ₁ = 0.0500, wR ₂ = 0.0659
Max/min Δρ [eÅ ⁻³]	1.52/-0.76	1.10/-0.55	1.22/-1.08
Flack parameter		-0.01(3)	

Identification code	3·Zn	3·Mg
CCDC Number	2195702	2195700
Empirical formula	$C_{150}H_{99}Cl_{11}N_{15}SbZn_3$	$C_{59}H_{40}Cl_2MgN_7Sb$
Formula weight	2819.25	1063.94
Temperature/K	180(2)	293(2)
Crystal system	triclinic	triclinic
Space group	P-1	P-1
a/Å	13.5059(4)	11.6920(4)
b/Å	16.2547(4)	13.9994(5)
c/Å	30.3809(8)	19.8328(5)
$\alpha/^\circ$	95.529(2)	78.498(3)
$\beta/^\circ$	93.028(2)	76.874(3)
$\gamma/^\circ$	90.230(2)	70.708(3)
Volume/Å ³	6629.1(3)	2956.48(17)
Z	2	2
$\rho_{\text{calc}}/\text{cm}^3$	1.412	1.195
μ/mm^{-1}	1.018	0.608
F(000)	2864	1080
Crystal size/mm ³	0.43 × 0.35 × 0.24	0.32 × 0.17 × 0.15
Radiation	MoK α	MoK α
2 θ range for data collection/ $^\circ$	4.166 to 50.162	3.524 to 50.414
Index ranges	-16 ≤ h ≤ 15, -19 ≤ k ≤ 19, -36 ≤ l ≤ 36	-13 ≤ h ≤ 13, -16 ≤ k ≤ 14, -23 ≤ l ≤ 23
Reflections collected	53489	26850
Independent reflections	23428 [R _{int} = 0.0373, R _{sigma} = 0.0618]	10623 [R _{int} = 0.0303, R _{sigma} = 0.0417]
Data/restraints/parameters	23428/0/1621	10623/0/634
Goodness-of-fit on F ²	1.028	1.03
Final R indexes [I ≥ 2 σ (I)]	R ₁ = 0.0547, wR ₂ = 0.1326	R ₁ = 0.0369, wR ₂ = 0.0786
Final R indexes [all data]	R ₁ = 0.0799, wR ₂ = 0.1501	R ₁ = 0.0528, wR ₂ = 0.0864
Max/min $\Delta\rho$ [eÅ ⁻³]	1.35/-1.28	0.61/-0.76

Table S5. Selected bond length and angles.

(E = Sb, Bi)	1·Zn-closed	2·Zn-closed	1·Zn-open	2·Zn-open
E–C _{py}	2.146(5)– 2.158(5)	2.235(6)– 2.261(5)	2.147(5)–2.163(4)	2.226(7)–2.269(6)
C _{py} –E–C _{py}	95.4(2)–96.0(2)	93.0(2)–94.2(2)	91.2(2)–101.3(2)	89.6(2)–99.8(3)
N–Zn	2.149(4)– 2.194(4)	2.149(5)– 2.184(5)	2.175(3)–2.211(4)	2.171(5)–2.211(6)

(E = P, Sb, Bi)	P·Mg	1·Mg	2·Mg
E–C _{py}	1.843(4)	2.155(4)	2.236(4)
C _{py} –E–C _{py}	100.78(13)	94.60(15)	93.13(12)
N–Mg	2.374(2)	2.330(4)	2.324(3)

(E = Sb, Bi)	3·py	4
E–C _{py}	2.14(1)–2.146(8)	2.215(8)–2.228(8)
C _{py} –E–C _{py}	97.3(3)–97.4(3)	106.8(2)–144.7(2)
E–Cl	2.449(2)–2.465(2)	2.572(2)–2.595(2)

(M = Zn, Mg)	3·Zn	3·Mg
Sb–C _{py}	2.109(4)–2.11(4)	2.102(3)–2.123(3)
C _{py} –Sb–C _{py}	115.6(2)–128.3(2)	119.4(1)–120.6(1)
N–M	2.178(4)–2.228(4)	2.380(2)–2.3850(18)
Sb–Cl	2.423(1)–2.460(1)	2.4384(9)–2.4426(9)

Determination of the size of the capsules

In addition to the discussion of the Zn–Zn distances in the main text, the “effective size” of the ligand (within the capsules) can be quantified by measuring the distances between the C in position 6 in the pyridyl rings (Figure S68b, blue). As observed in the X-ray structures, the average C---C distance increases descending in the group, 7.214, 7.407 and 7.450 Å (average) for P, Sb and Bi respectively, thus leading to larger capsules (see discussion in the main text).

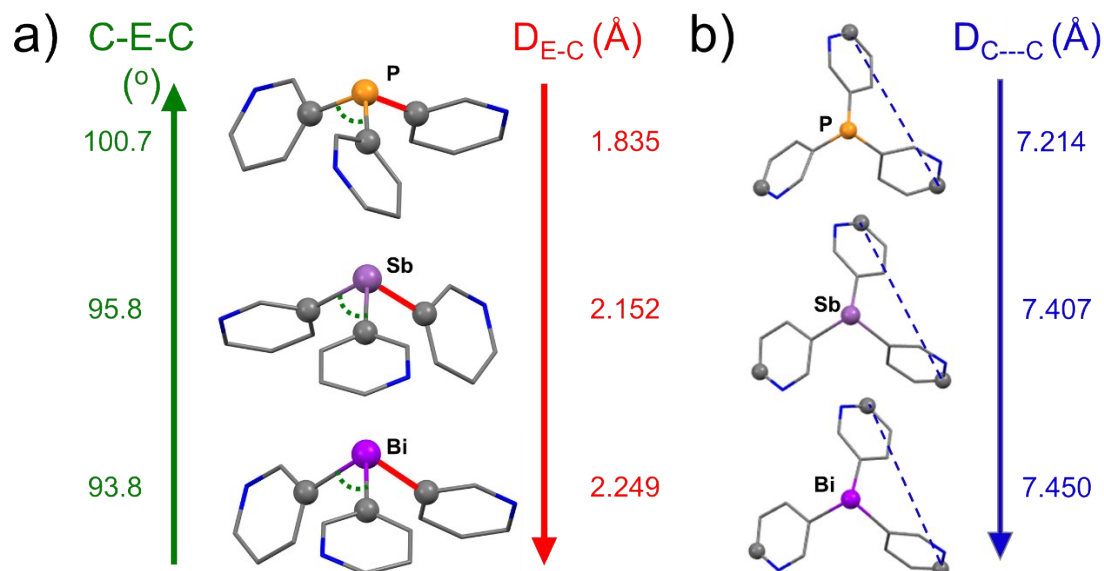


Figure S68. Trends in the average C–E–C angles (a, green), E–C distances (a, red) and C₆–C₆ distances (b, blue) in the X-ray structures of the capsules $\{[E(3-py)_3] \cdot (ZnTPP)_3\}$ (E = P, Sb and Bi). Colour key: C (grey), N (blue), P (orange), Sb (light purple), Bi (purple).

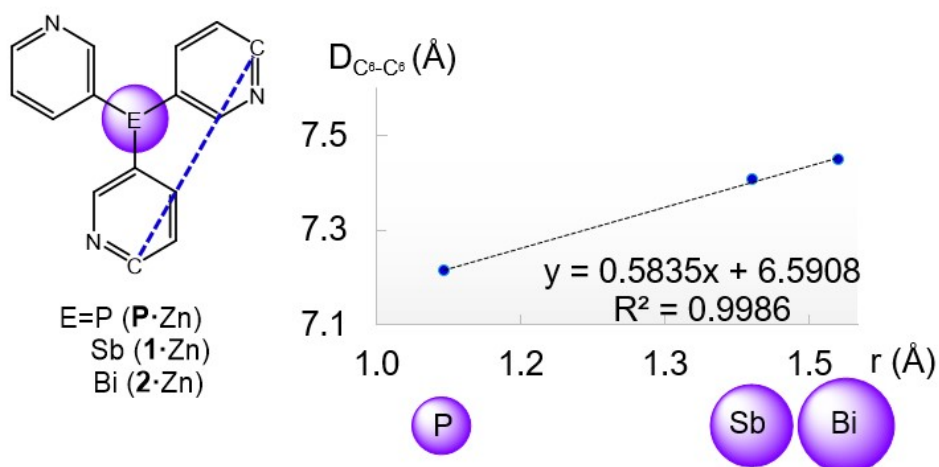


Figure S69. Linear correlation between the covalent radii of the bridgehead atom and the C₆–C₆ distances in the X-ray structures of $\{[P(3-py)_3] \cdot (ZnTPP)_3\}$, 1·Zn-closed and 2·Zn-closed.

There is a also direct correlation between the volume of the capsules {[P(3-py)3]·(ZnTPP)3}, **1**·Zn and **2**·Zn (2836, 2879 and 2912 Å³) and the covalent radii of the bridgehead atom in the E(3-py)₃ ligand. The online tool Voss Volume Voxelator was utilized to calculate the volume of the capsule (using a 1.2 Å probe radius and medium grid).^[13] Molecular graphics and analyses were performed with UCSF Chimera.^[14]

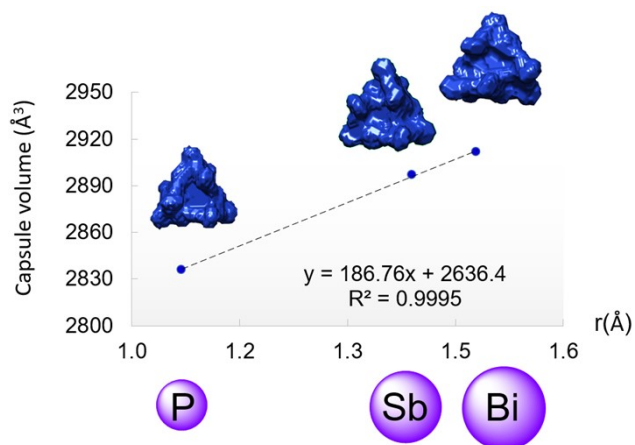
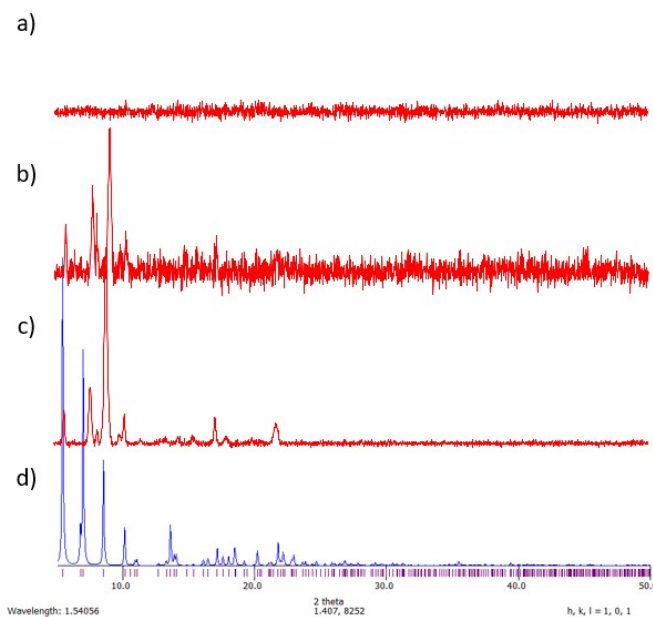


Figure S70. Linear correlation between the covalent radii of the bridgehead atom and the volume of the capsule in **P**·Zn, **1**·Zn and **2**·Zn.

Powder X-ray diffraction studies

Powder X-ray diffraction studies show that **P·Mg**, **1·Mg** and **2·Mg** are still crystalline after keeping the sample under prolonged vacuum or treatment at 100 °C (10 min) and subsequently 200 °C (10 min). The p-XRD patterns show some differences with respect to the predicted ones, suggesting that the framework structure has changed upon solvent removal but the materials are still crystalline, with somewhat broader peaks indicative of defect formation and less regularity, as well as changes in the pattern (with exception of **P·Mg**, for which no peaks were observed after treatment at 200 °C).



*Figure S71. Comparison of predicted (d, blue) and the experimental (red) XRPD patterns for compound **P·Mg** after 60 h under vacuum (c), heating the sample at 100 °C for 10 min (b) and heating the sample at 200 °C for 10 min (a). The significant difference between the observed and predicted p-XRD appears to be the result from the loss of lattice solvent.*

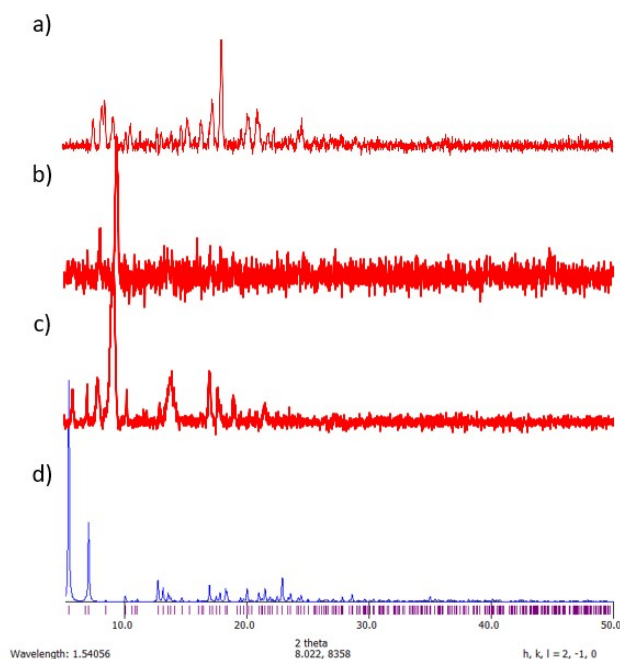


Figure S72. Comparison of predicted (d, blue) and the experimental (red) XRPD patterns for compound 1·Mg after 60 h under vacuum (c), heating the sample at 100 °C for 10 min (b) and heating the sample at 200 °C for 10 min (a). The significant difference between the observed and predicted p-XRD appears to be the result from the loss of lattice solvent.

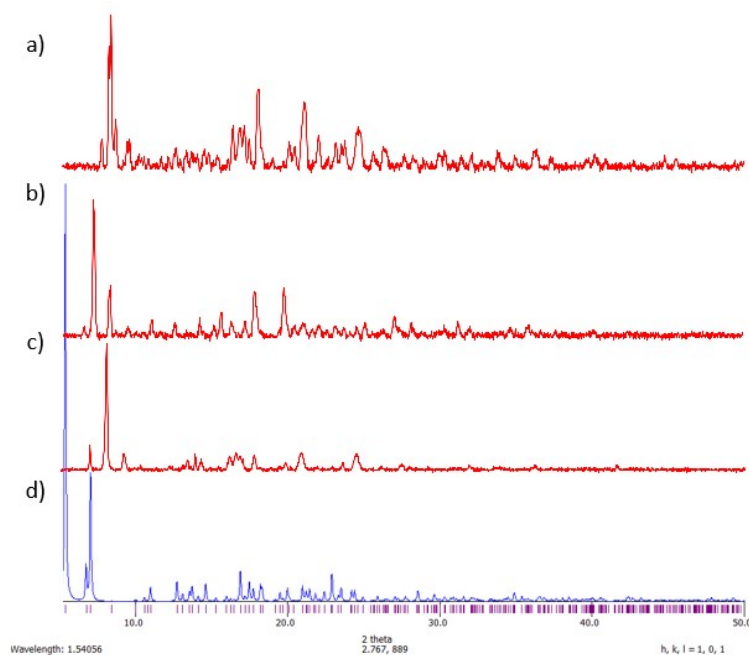


Figure S73. Comparison of predicted (d, blue) and the experimental (red) XRPD patterns for compound 2·Mg after 60 h under vacuum (c), heating the sample at 100 °C for 10 min (b) and heating the sample at 200 °C for 10 min (a). The significant difference between the observed and predicted p-XRD appears to be the result from the loss of lattice solvent.

TGA and TGA-MS studies

The thermal stabilities of compounds **P**·Mg, **1**·Mg and **2**·Mg were studied via dynamic thermogravimetric analysis (TGA) on a TA-Q500 analyzer, using nitrogen gas flow (60 mL/min). The samples were heated at 20 °C/min using the Hi-Res method. The first weight loss of the samples below 50 °C was related to the loss of solvent from the material. The weight loss below 200 °C is associated with solvent trapped in the crystals (see Figure S74). This corresponds to a total solvent (CHCl₃ and hexane, observed to be present by ¹H NMR in DMSO) weight loss of 4.89 wt% (FW of 125) for **P**·Mg and 3.41 wt% (FW of 92) for **1**·Mg (Figure S75 and S76). In both cases, weight loss above 280 °C should be associated with the degradation of the compound (see Figure S75 and S76). The second cycle after keeping the samples at 250 °C for 10 min shows no weight loss before the generalized degradation temperature of the material, indicating that all the possible occluded solvent was removed and that the compounds were thermally stable.

A different behaviour was observed for compound **2**·Mg (See Figure S74 in green and S77). Similarly to **P**·Mg and **1**·Mg, **2**·Mg underwent a weight loss of 6.23 wt% (from solvent loss) in the range from 110 to 170 °C (Figure S77). The removal of hexane and chloroform was confirmed by TGA-MS (Figure S78) in which two peaks at *m/z* 86 (hexane) and 119 (chloroform) are observed below 200 °C as well as by ¹H NMR in DMSO-d₆. However, in this case, the TGA-MS also indicates a weight loss just above 200 °C, due to the loss of pyridine (a peak at *m/z* 79 was observed by TGA-MS) which should be associated with the partial degradation of the compound (Figure S78). The release of pyridine from **2**·Mg was also confirmed by ¹H NMR, because after heating a solid sample of **2**·Mg for 10 min at 250 °C, decomposition was evident with the presence of free pyridine in the ¹H NMR spectrum. This degradation is in contrast to the behaviour of **P**·Mg and of **1**·Mg, for which no decomposition was observed by ¹H NMR (i.e., after heating at 250 °C for 10 min in DMSO-d₆, no free pyridine (or any other symptom of decomposition) was observed by NMR or by TGA studies).

However, after observing the BET results (see next section), we carried out a further thermogravimetric study treating the samples under degassing conditions similar to those used in the adsorption isotherms. Surprisingly, it was observed that after this treatment, the dynamic TGA curves of **P**·Mg and of **1**·Mg were different, since now weight losses appeared between 200 °C and the generalized degradation temperature of the material. Therefore, it seems that after the elimination of the solvent occluded in the framework, the structure is capable of undergoing modification, probably as **2**·Mg did.

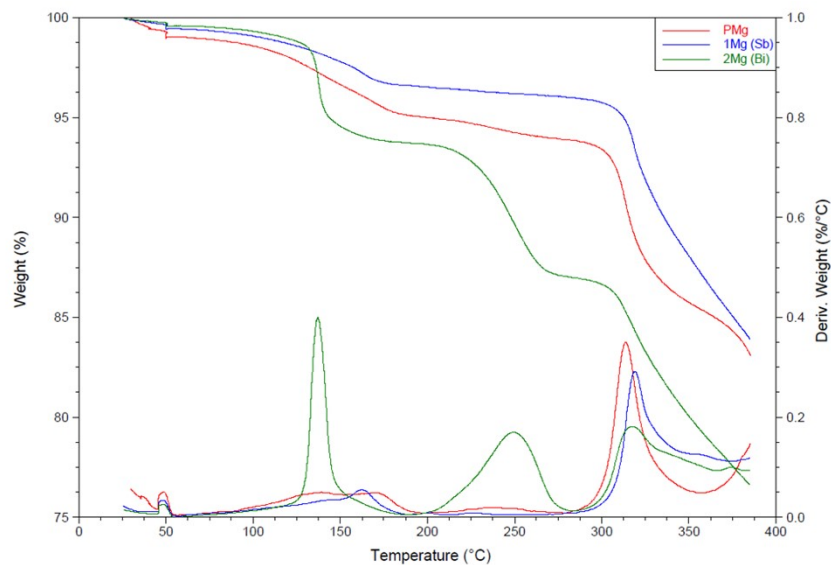


Figure S74. TGA thermograms of $P \cdot Mg$ (red), $1 \cdot Mg$ (blue) and $2 \cdot Mg$ (green) after keeping the sample under vacuum.

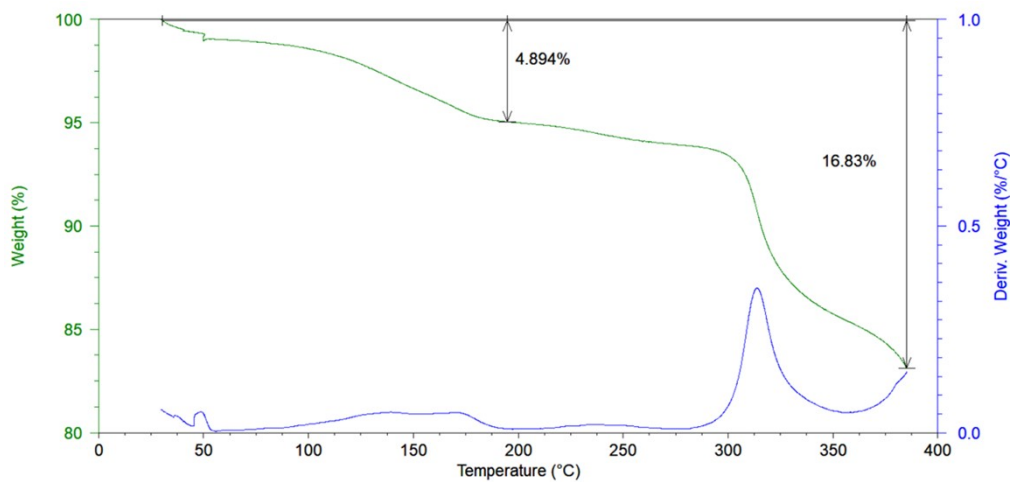


Figure S75. TGA thermogram of $P \cdot Mg$.

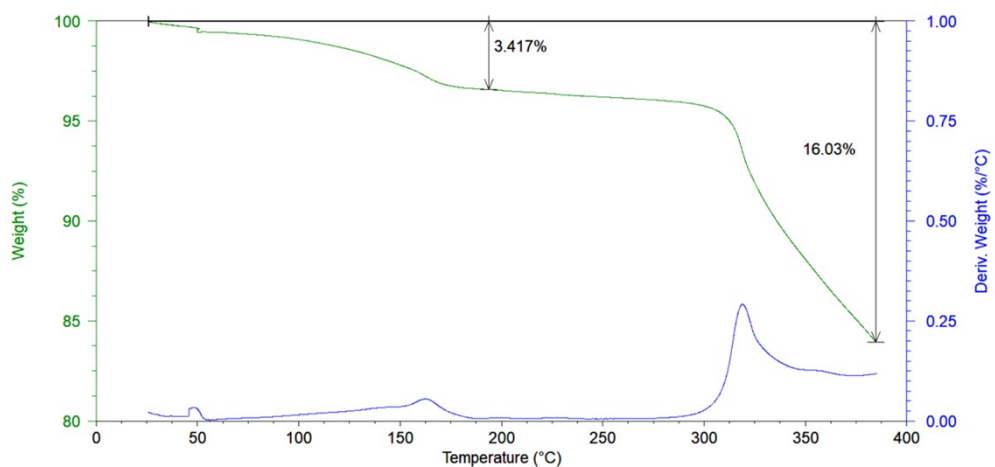


Figure S76. TGA thermogram of $1 \cdot Mg$.

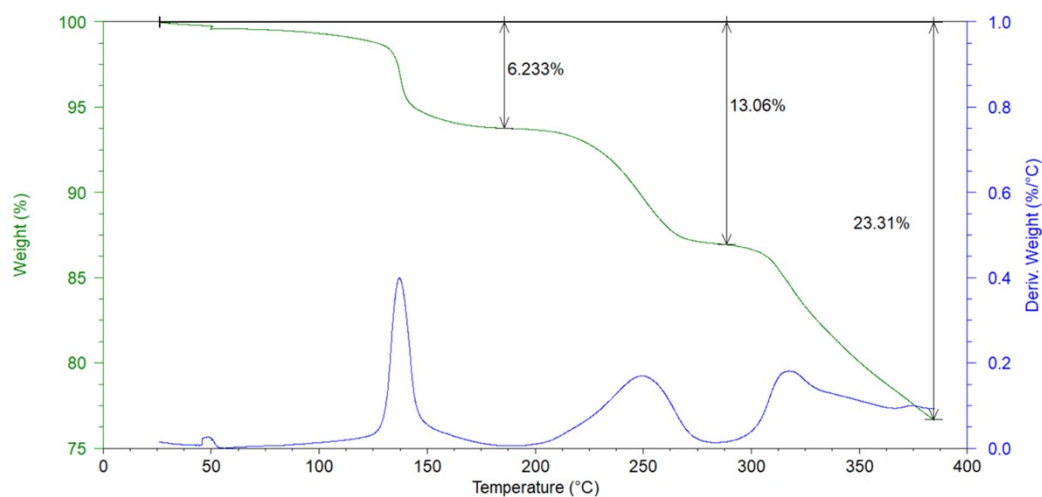


Figure S77. TGA thermogram of 2·Mg.

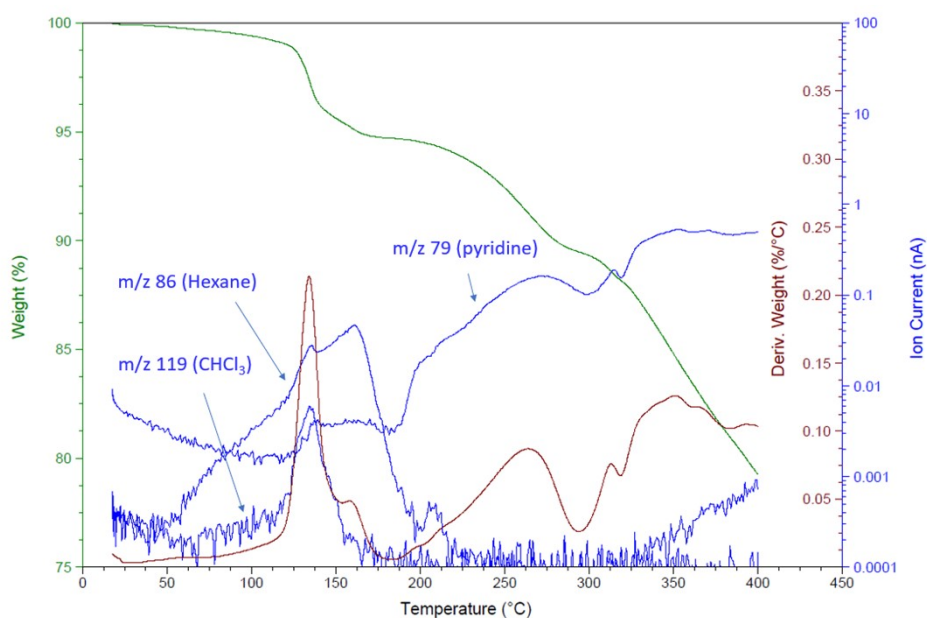


Figure S78. TGA-MS analysis of 2·Mg showing the weight loss associated with m/z 86 (hexane), 119 (chloroform) and 79 (pyridine). The latter was observed above 200 °C. The experiment was conducted on a TA Q-500 thermobalance (TA Instruments) combined with a mass spectrometer (MS) ThermoStar GSD 301T (Pfeiffer Vacuum GmbH, Germany).

N₂ and CO₂ Sorption experiments

Samples were degassed under high vacuum at 150 °C for 12 hours before the adsorption measurements. N₂ adsorption-desorption isotherms at 77 K were measured in an automatic device ASAP2420 (Micromeritics) or in a NOVA800 (Anton Parr) at 273 K for CO₂. The BET equation was applied in the 0.05–0.25 p/p° range to the N₂ isotherms. Micropore volume was determined by applying the Dubinin-Radushkevich (DR) equation to the N₂ adsorption isotherm at $p/p_0 < 0.15$ or to the CO₂ adsorption isotherm. Total pore volume was determined as the amount of N₂ adsorbed as liquid at $p/p_0 = 0.975$ (Gurvich Rule).

The results obtained are gather in the tables S6 and S7:

Table S6. Porosity parameters from N₂.

	$S_{\text{BET}} / \text{m}^2\text{g}^{-1}$	$V_{\text{total}} \times 10^3 / \text{cm}^3\text{g}^{-1}$	$V_{\text{micro}} \times 10^3 / \text{cm}^3\text{g}^{-1}$
P·Mg	0.64	0.8	0.2
2·Mg	1.7	4	0.7

Table S7. Porosity parameters from CO₂.

	$S_{\text{DR}} / \text{m}^2\text{g}^{-1}$	$V_{\text{micro}} \times 10^3 / \text{cm}^3\text{g}^{-1}$	E / kJmol^{-1}
P·Mg	76	27	18.66
2·Mg	41	14	18.27

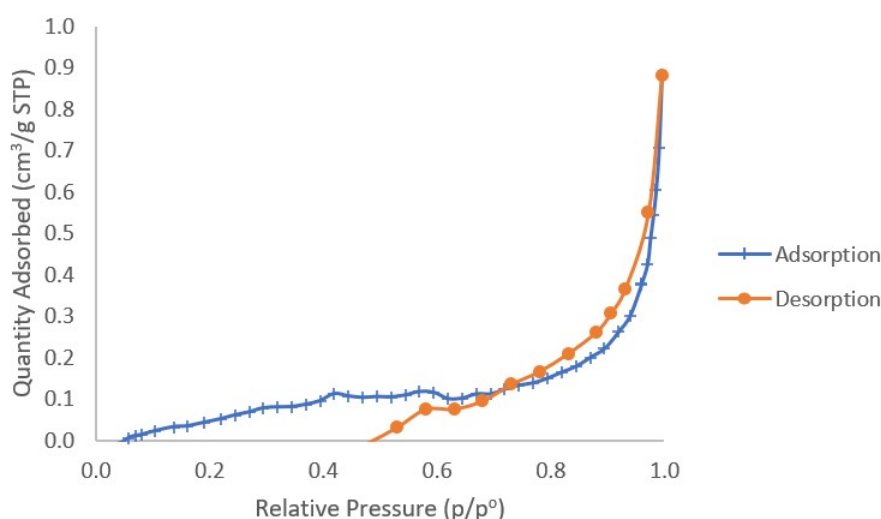


Figure S79. N₂ adsorption-desorption isotherms for P·Mg.

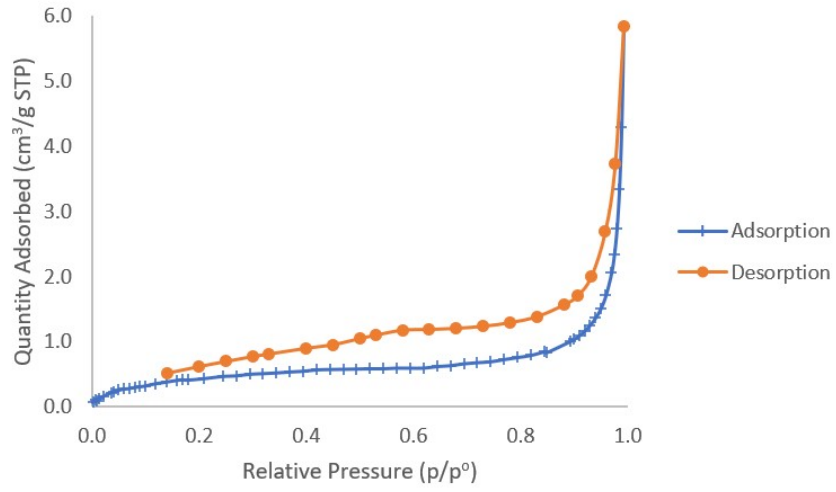


Figure S80. N₂ adsorption-desorption isotherms for 2·Mg.

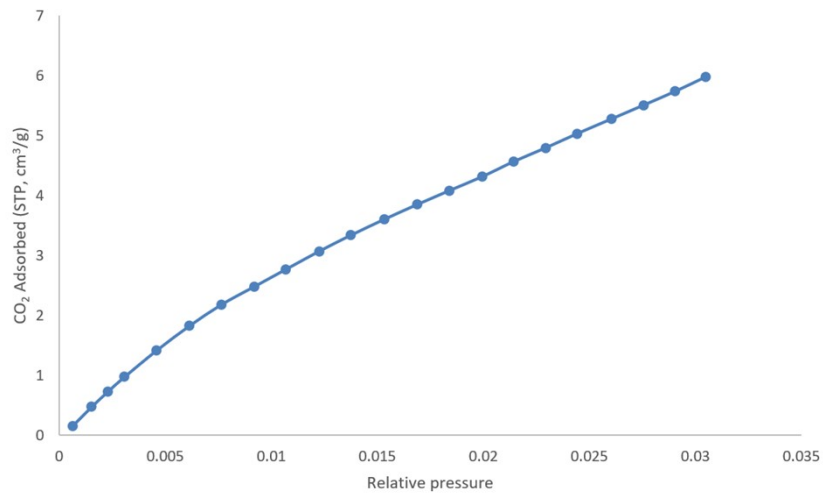


Figure S81. CO₂ adsorption isotherm for P·Mg.

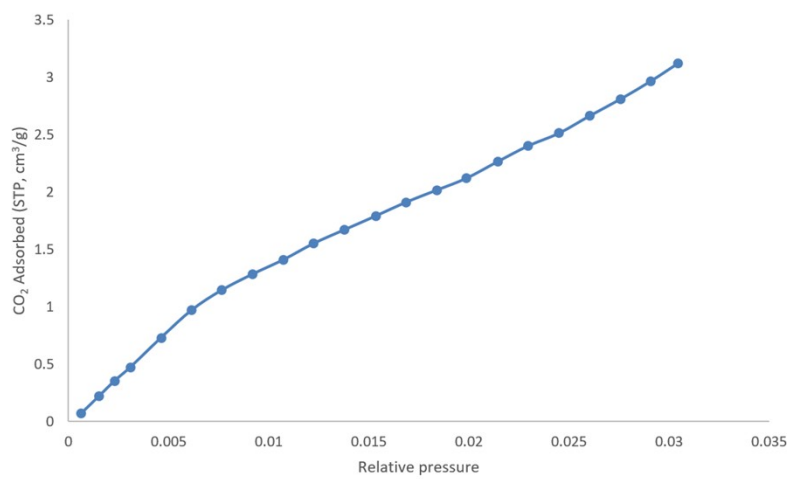


Figure S82. CO₂ adsorption isotherm for 2-Mg.

Computational details

All computations were carried out using the Gaussian16 package,^[15] in which the hybrid method of Austin, Petersson and Frisch with spherical atom dispersion terms (APFD) was applied.^[16] The triple zeta cc-pVTZ-PP basis set with effective core potentials was used for the heavy atoms (Zn, Sb and Bi)^[17–20], as found in the basis set exchange library,^[21–23] and 6-31G(d,p) was used for the rest of the atoms. Geometry optimizations were performed without symmetry restrictions using the initial coordinates derived from X-ray data when available, and frequency analyses were performed to ensure that a minimum structure with no imaginary frequencies was achieved in each case. The visualization of the calculation results was performed with GaussView 6.1.^[24]

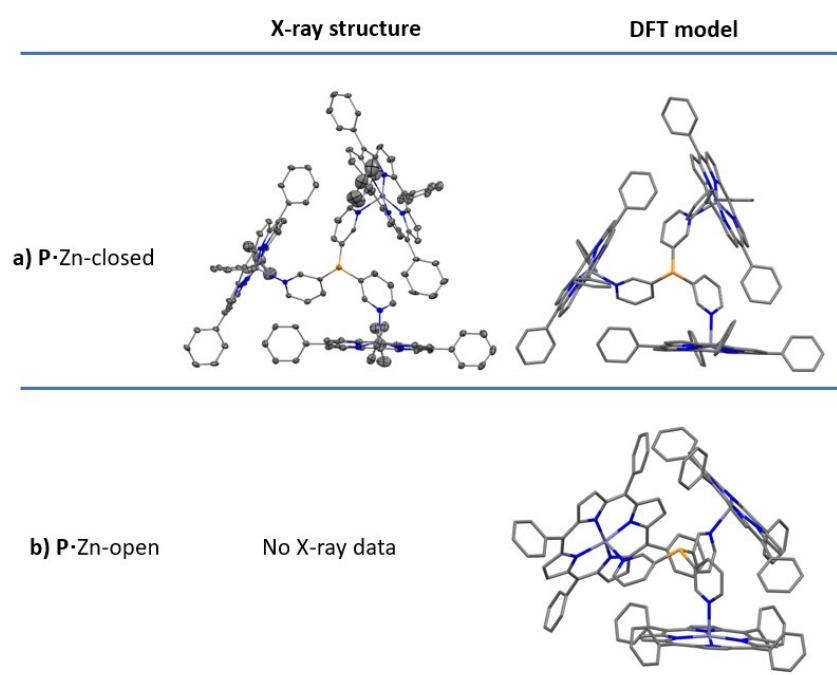


Figure S83. a) Comparison of the X-ray structure^[25] and the DFT-calculated structure of the conformer P·Zn-closed showing minimal structure changes. b) DFT-calculated structure of the conformer P·Zn-open, there is no X-ray data available for P·Zn-open.

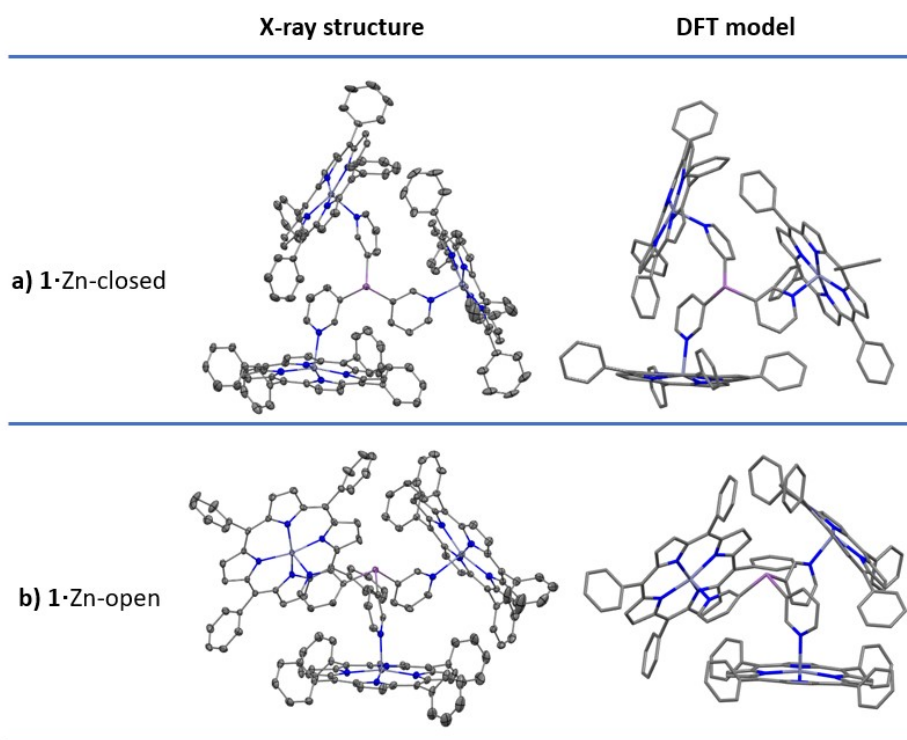


Figure S84. a) Comparison of the X-ray structure and the DFT-calculated structure of the conformer 1·Zn-closed showing minimal structure changes. b) Comparison of the X-ray structure and the DFT-calculated structure of the conformer 1·Zn-open showing minimal structure changes.

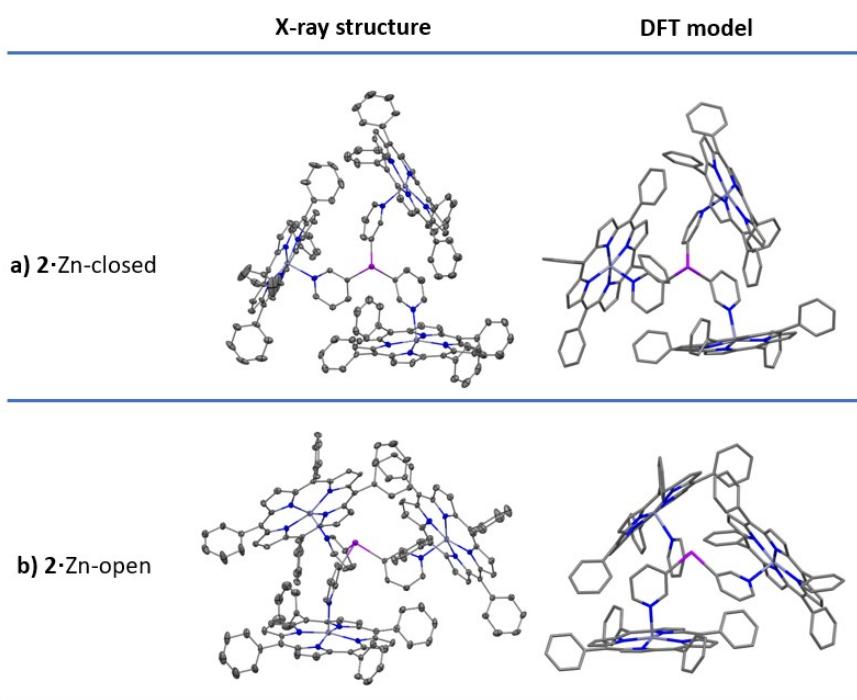
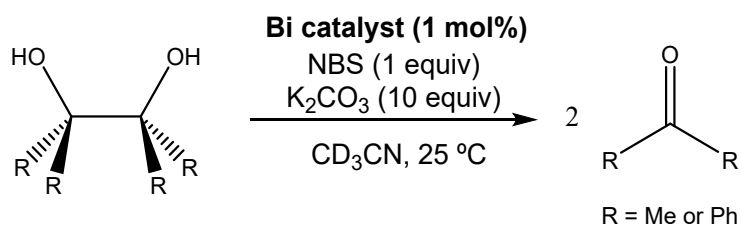


Figure S85. a) Comparison of the X-ray structure and the DFT-calculated structure of the conformer 2·Zn-closed showing minimal structure changes. b) Comparison of the X-ray structure and the DFT-calculated structure of the conformer 2·Zn-open showing minimal structure changes.

Preliminary catalytic studies

General procedure for Bi-catalyzed cleavage of 1,2 diols.

In a narrow Schlenk tube, the corresponding 1,2-diol (0.14 mmol), K_2CO_3 (1.4 mmol, 10 equiv.) and the Bi catalyst (**2** or **2**·Zn, 1 mol%) were dissolved in 1 mL of CD_3CN and stirred for 5 min. After that, a solution of NBS (0.14 mmol, 1 equiv.) in 0.5 mL of CD_3CN was added dropwise and the reaction was left at 25 °C for the desired time. An aliquot was taken and 1H NMR was used to determine the yield.



Scheme S1. Bi-catalyzed cleavage of 1,2 diols ($R = Me$ or Ph).

Procedure for Sb-catalyzed oxidations of α -hydroxyketones.

For the kinetic experiments, the corresponding α -hydroxyketone (0.02 mmol) and the Sb catalytic species (10 mol%) were dissolved in 1 ml of CDCl_3 in a J. Young NMR tube under air. ^1H NMR monitoring was subsequently used to determine the yield at different times and Figure S86 shows the formation of the α -diketone with time as determined by ^1H NMR. No product formation was observed under the same conditions in the absence of catalyst (with or without the presence of Zn-TPP metalloporphyrin).

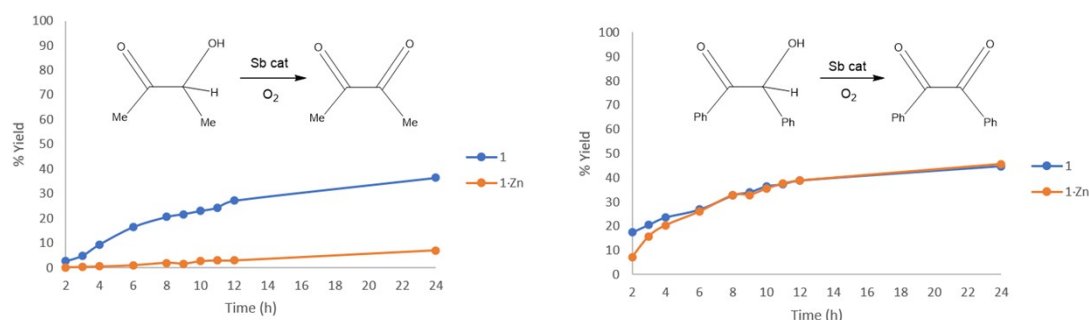
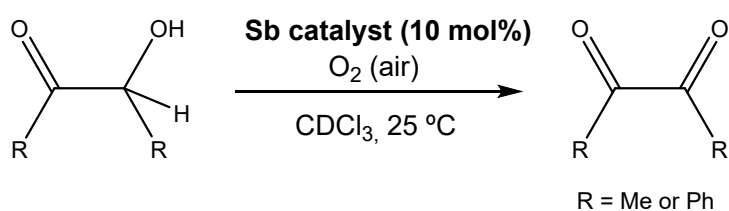


Figure S86. Kinetic experiment of **1** and **1·Zn** for Sb-catalyzed oxidation of α -hydroxyketones. Reaction conditions: α -hydroxyketone (0.02 mmol), Sb catalyst (**1** and **1·Zn**, 10% mol), 1 ml of CDCl_3 at 25 °C in a young NMR tube.

This reaction was also performed in a 5 ml vial that was loaded under air in order to compare the results when more oxygen was available. The corresponding α -hydroxyketone (0.04 mmol) and the Sb catalyst (10 mol%) were dissolved in 2 ml of CDCl_3 . The sample was stirred for 24 h and an aliquot was taken, and ^1H NMR was used to determine the yield. While the results showed a similar tendency to those of the reactions carried out in the J. Young tube, i.e., the use of the capsule **1·Zn** instead of **1** dramatically inhibits the reaction of acetoin but not the reaction of benzoin, and the yields were better (Table S8 entries 3-6), presumably due to the availability of more oxygen, reaching up to 80% in the case of the oxidation of benzoin ($\text{PhCOCH}(\text{OH})\text{Ph}$) using **1·Zn** after 24 h (entry 6). Interestingly, in this case, the better yield observed for the oxidation of benzoin ($\text{PhCOCH}(\text{OH})\text{Ph}$) using **1·Zn** instead of **1** is related to less degradation of the antimony catalyst within the capsule.

Entry	Sb catalyst	Yield (%) R = Me	Yield (%) R = Ph
1	- ^a	0	-
2	- ^b	0	-
3	- ^a	-	0
4	- ^b	-	0
5	1	61	-
6	1 ·Zn	11	-
7	1	-	54
8	1 ·Zn	-	80

Table S8. Sb-catalyzed oxidation of α -hydroxyketones. Reaction conditions: α -hydroxyketone (0.04 mmol), Sb catalyst (**1** and **1**·Zn, 10% mol), 2 ml of CDCl_3 at 25 °C in a vial after 24 h.^a In the absence of the catalyst and with no Zn-TPP. ^b In the absence of the catalyst and in the presence of Zn-TPP (30% mol).

References

- [1] Á. García-Romero, J. M. Martín-Álvarez, D. Miguel, D. S. Wright, C. M. Álvarez, R. García-Rodríguez, *Inorg. Chem.* **2021**, *60*, 19206–19218.
- [2] A. M. Kluwer, I. Ahmad, J. N. H. Reek, *Tetrahedron Lett.* **2007**, *48*, 2999–3001.
- [3] Agilent and U. K. Technologies U.K. Ltd.: Oxford, **2011**.
- [4] G. M. Sheldrick, *Acta Crystallogr. Sect. C.* **2015**, *71*, 3–8.
- [5] O. V Dolomanov, L. J. Bourhis, R. J. Gildea, J. A. K. Howard, H. Puschmann, *J. Appl. Crystallogr.* **2009**, *42*, 339–341.
- [6] C. F. MacRae, I. Sovago, S. J. Cottrell, P. T. A. Galek, P. McCabe, E. Pidcock, M. Platings, G. P. Shields, J. S. Stevens, M. Towler, P. A. Wood, *J. Appl. Crystallogr.* **2020**, *53*, 226–235.
- [7] A. Macchioni, G. Ciancaleoni, C. Zuccaccia, D. Zuccaccia, *Chem. Soc. Rev.* **2008**, *37*, 479–489.
- [8] M. Marchini, A. Luisa, G. Bergamini, N. Armaroli, B. Ventura, M. Baroncini, N. Demitri, E. Iengo, P. Ceroni, *Chem. – A Eur. J.* **2021**, *27*, 16250–16259.
- [9] S. Bachmann, R. Neufeld, M. Dzemski, D. Stalke, *Chem. - A Eur. J.* **2016**, *22*, 8462–8465.
- [10] S. Bachmann, B. Gernert, D. Stalke, *Chem. Commun.* **2016**, *52*, 12861–12864.
- [11] R. Neufeld, D. Stalke, *Chem. Sci.* **2015**, *6*, 3354–3364.
- [12] P. Kuzmič, *Anal. Biochem.* **1996**, *237*, 260–273.
- [13] N. R. Voss, M. Gerstein, *Nucleic Acids Res.* **2010**, *38*, W555–W562. Online access to program: <http://3vee.molmovdb.org/>
- [14] E. F. Pettersen, T. D. Goddard, C. C. Huang, G. S. Couch, D. M. Greenblatt, E. C. Meng, T. E. Ferrin, *J. Comput. Chem.* **2004**, *25*, 1605–1612.
- [15] Gaussian 16, Revision C.01, M. J. Frisch, G. W. Trucks, H. B. Schlegel, G. E. Scuseria, M. A. Robb, J. R. Cheeseman, G. Scalmani, V. Barone, G. A. Petersson, H. Nakatsuji, X. Li, M. Caricato, A. V. Marenich, J. Bloino, B. G. Janesko, R. Gomperts, B. Mennucci, H. P. Hratchian, J. V. Ortiz, A. F. Izmaylov, J. L. Sonnenberg, D. Williams-Young, F. Ding, F. Lipparini, F. Egidi, J. Goings, B. Peng, A. Petrone, T. Henderson, D. Ranasinghe, V. G. Zakrzewski, J. Gao, N. Rega, G. Zheng, W. Liang, M. Hada, M. Ehara, K. Toyota, R. Fukuda, J. Hasegawa, M. Ishida, T. Nakajima, Y. Honda, O. Kitao, H. Nakai, T. Vreven, K. Throssell, J. A. Montgomery, Jr., J. E. Peralta, F. Ogliaro, M. J. Bearpark, J. J. Heyd, E. N. Brothers, K. N. Kudin, V. N. Staroverov, T. A. Keith, R. Kobayashi, J. Normand, K. Raghavachari, A. P. Rendell, J. C. Burant, S. S. Iyengar, J. Tomasi, M. Cossi, J. M. Millam, M. Klene, C. Adamo, R. Cammi, J. W. Ochterski, R. L. Martin, K. Morokuma, O. Farkas, J. B. Foresman and D. J. Fox, Gaussian, Inc., Wallingford CT, 2019.
- [16] A. Austin, G. A. Petersson, M. J. Frisch, F. J. Dobek, G. Scalmani and K. Throssell, in *J. Chem. Theory Comput.*, 2012, **8**, 4989–5007.
- [17] D. Figgen, G. Rauhut, M. Dolg and H. Stoll, *J. Chem. Phys.*, 2005, **311**, 227–244.
- [18] B. Metz, H. Stoll and M. Dolg, *J. Chem. Phys.*, 2000, **113**, 2563–2569.

- [19] K. A. Peterson, *J. Chem. Phys.*, 2003, **119**, 11099–11112.
- [20] K. A. Peterson, C. Puzzarini, *Theor. Chem. Acc.*, 2005, **114**, 283–296.
- [21] B. P. Pritchard, D. Altarawy, B. Didier, T. D. Gibson and T. L. Windus, *J. Chem. Inf. Model.*, 2019, **59**, 4814–4820.
- [22] D. Feller, *J. Comput. Chem.*, 1996, **17**, 1571–1586.
- [23] K. L. Schuchardt, B. T. Didier, T. Elsethagen, L. Sun, V. Gurumoorthi, J. Chase, J. Li and T. L. Windus, *J. Chem. Inf. Model.*, 2007, **47**, 1045–1052.
- [24] GaussView, Version 6.1, Roy Dennington, Todd A. Keith, John M. Millam, Semichem Inc., Shawnee Mission, KS, 2016.
- [25] V. Bocokić, A. Kalkan, M. Lutz, A. L. Spek, D. T. Gryko and J. N. H. Reek, *Nat. Commun.*, 2013, **4**, 1–9.